



TECHNISCHE  
UNIVERSITÄT  
WIEN  
Vienna | Austria

DISSERTATION

# ***Applications of Atomic Layer Deposition in modern Materials Science***

*Ausgeführt zum Zwecke der Erlangung des akademischen Grades eines Doktors der  
technischen Wissenschaften unter der Leitung von*

Univ. Prof. Dr. Dominik Eder

und

Assistant Prof. Dr. Bernhard Bayer-Skoff

*Institut für Materialchemie*

*E165*

*Eingereicht an der Technischen Universität Wien*

*Fakultät für Technische Chemie*

von

***DI. Jakob Rath, BSc.***

*01308809*

Wien, am:

---

Unterschrift



# ABSTRACT

While many techniques are suitable for designing ultra-thin films, few are as sophisticated as Atomic Layer Deposition (ALD). This method allows any substrate to be coated with ultra-thin layers of material with unparalleled uniformity and thickness control in the sub-nm range. ALD was widely used in the second half of the 20th century to synthesize layers of oxides, nitrides, sulfides or pure metals. However, in the last 20 years, researchers have started to develop routes to highly complex materials such as metal organic frameworks (MOFs) by all-gas phase approaches, generally trying to enable their application on an industrial scale.

In this work, we demonstrate a route for the ALD synthesis of the MOF Ti-MIL-125 and present a set of characterization methods suitable for understanding such new materials. We also demonstrate the possibility of using ALD to synthesize a MOF laminate of Ti-MIL-125 and Zr-UiO-66, highlighting the uniformity and interface quality of the stack. Through a series of experiments aimed at improving the crystallinity of our networks, we have been able to gain insights into the kinetics and thermodynamics of these systems. In the last chapter, we demonstrate the uniformity of ALD-TiO<sub>2</sub> coatings on complex shaped and highly intricate 3D-printed TiVAI substrates.

# Kurzfassung

Obwohl sich viele Techniken zur Entwicklung ultradünner Schichten eignen, sind wenige so hoch entwickelt wie die Atomlagenabscheidung (ALD). Mit dieser Methode kann jedes beliebige Substrat mit ultradünnen Filmen unterschiedlichster Materialien beschichtet werden, die eine beispiellose Gleichmäßigkeit sowie Schichtdickenkontrolle im Sub-nm-Bereich aufweisen. ALD wurde in der zweiten Hälfte des 20. Jahrhunderts in großem Umfang zur Synthese von Schichten aus Oxiden, Nitriden, Sulfiden oder reinen Metallen eingesetzt. In den letzten 20 Jahren haben Forscher damit begonnen, Wege zu hochkomplexen Materialien wie metallorganischen Gerüstverbindungen (MOFs) zu entwickeln, die ausschließlich in der Gasphase hergestellt werden, um deren Anwendung im industriellen Maßstab zu ermöglichen.

In dieser Arbeit demonstrieren wir einen Weg für die ALD-Synthese des MOF Ti-MIL-125 und stellen eine Reihe von Charakterisierungsmethoden vor, die zum Verständnis solcher neuen Materialien geeignet sind. Wir demonstrieren auch die Möglichkeit der ALD-Synthese eines MOF-Laminats aus Ti-MIL-125 und Zr-UiO-66, wobei wir die Gleichmäßigkeit und die Qualität der Grenzflächen des Stapels hervorheben. Durch eine Reihe von Experimenten, die darauf abzielen, die Kristallinität unserer Netzwerke zu verbessern, konnten wir Einblicke in die Kinetik und Thermodynamik dieser Systeme gewinnen. Im letzten Kapitel demonstrieren wir die Gleichmäßigkeit von ALD-TiO<sub>2</sub>-Beschichtungen auf hochkomplexen 3D-gedruckten TiVAI-Substraten.

# Acknowledgments

This thesis represents a significant amount of time and work that has consumed the last few years of my life and would not exist without the help and support of numerous colleagues and friends. I am deeply grateful to be surrounded by such amazing, loving and caring people and this part of my thesis is dedicated to them. As the number of people who have had a positive influence on my work is vast, I will try to focus on those who have had the greatest impact on my outcome and motivation over these years.

First of all, I would like to thank my supervisors, Assistant Prof. Dr. Bernhard Christian Bayer-Skoff and Prof. Dr. Dominik Eder, for their brilliant guidance, support and trust over the past years. When I decided to start my PhD in their group, my decision was based on a sudden emotion regarding the human focus within the MMC department. This feeling has been confirmed almost every day during this time. In addition, they supported me in every way possible, enabling me to broaden my focus, learn much more than I ever thought possible, and develop a scientific understanding of the world that completely changed my perspective in many ways. It has been a great pleasure to work with such dedicated and encouraging scientists and I hope to keep this connection alive in the future.

In writing this thesis, it is clear that many people have contributed ideas, specific knowledge and help in many other ways. Therefore, I would like to thank all my students who did amazing work and always showed an exceptionally high level of dedication and interest, and I am happy to call some of them my friends. To name just a few, Tomas Gregan, Nick Parak, Laura Aichinger, Johannes Jeryczynski, Simon Demmer, Tanja Steger and Jury Möller did a great job in supporting my research and lifting my spirits every day. My special thanks go to Daniel Matulka, who is one of the most outstanding young scientists I have ever met. Without him, many individual projects within this thesis would not have been possible and I am excited to see where his deep interest and astonishing knowledge will lead him.

Throughout these years, there was always a very high level of social interaction within the whole institute and I had the chance to not only come to TU every day to work, but also to meet my friends there. I consider this a great privilege and would not want to miss any of them. However, there are a few people I would like to mention individually, as they have become real friends over the past few years: Nevzat Yigit is a lovely person and one of the main reasons why I decided to apply for the job, Sebastian Buhr was always there when I needed technical support or someone to talk to, Njomza Isufaj became a close friend and will hopefully stay one, next to her Martin Nastran, Markus Hofer and Bodo Baumgartner are my favorite companions for any "work holidays", Hannah Rabl was always an expert at making every room she entered a little nicer, I always enjoyed being around Jasmin Schubert, who also taught me a lot about XPS, Julia Roll and Angelika Gabriel were always helpful and lovely, Werner Artner would be my father-in-law of choice - he is, as far as I know, the most lovable character at TU Wien. However, there are many others who have had a huge impact on my success and personal development and I am sorry that I cannot name them all, but I hope they know how important they are to me. Thank you for making my time as a PhD student so enjoyable.

I would like to thank everyone who has contributed scientifically to this thesis: The funding agencies, the team at the X-Ray Centre of the TU Vienna, who were always friendly and helpful, even though some requests were tricky and almost impossible, the team and colleagues at USTEM, especially Johannes Bernardi for his support whenever I had a problem with an instrument, Michael Stöger-Pollach for teaching me so much about electron optics, Sabine Schwarz, Thomas Schachinger and Martin Gruber for their endless patience when explaining new methods. The AIC team has always supported me throughout my PhD, and Annette Foelske, the head of the center and nowadays my boss, was one of the first supporters I had at the TU and I am very grateful to be able to rely on her guidance now. My other colleagues Markus Sauer, Francesco Laudani and Jakob Hemetsberger impress me almost every day with their great skills and abilities. I am very happy to have the opportunity to learn so much in such a great environment. I would also like to acknowledge the work of our other cooperation partners at the TU - first and foremost Herbert "Hörby" Hutter and his team - but also many former colleagues and people from other departments: Oliver Hudak, Rebecca Janknecht, Balint Hajas, Erik Lübke, Ariane Giesriegel, Willi Zeni, Francesco Valentini and many others. Thank you for making my life a little easier. I also had the privilege of working with some amazing scientists on some experiments we ran on the CLAES beamline in March 2024. Thank you very much for your help and guidance, Vlad and Jose.

My special thanks go to Dr. Bernhard Fickl, who has become one of my closest friends over the last four years. You made coming to work less frustrating on bad days and more enjoyable on good days. Thank you for your support and friendship.

Finally, I would like to thank the people who have been there for me all my life and have probably contributed the most to my success: my friends and family. Even though I am not an easy person to deal with, you have always been brilliant at strengthening my faith and belief in myself and the world around me, and encouraging me to become a better person. Thank you for your support over the years and thank you for making existence so pleasant.

# List of Publications

## Primary

1. **Jakob Rath**, Bernhard Fickl, Daniel Matulka, Njomza Isufaj, Hanspeter Kählig, Clemens Mangler, Jani Kotakoski, Alexey Cherevan, Shaghayegh Naghdi, Ariane Giesriegl, Sabine Schwarz, Michael Stöger-Pollach, Markus Sauer, Annette Foelske, Bernhard C. Bayer, Dominik Eder. *Atomic layer deposition of conformal Ti-MIL-125-like metal organic framework ultrathin films on nanoscaled substrates towards photocatalysis.* (2024) – submitted
2. **Jakob Rath**, Bernhard Fickl, Tomas Gregan, Nick Parak, Laura Aichinger, Markus Sauer, Gerlinde Habler, Florian Fahrnberger, Shaghayegh Naghdi, Annette Foelske, Herbert Hutter, Bernhard C. Bayer, Dominik Eder. *Synthesis of Metal-Organic-Framework Nano-Laminates by use of ALD and their Characterization.* (2024) – in preparation
3. **Jakob Rath**, Johannes Jeryczynski, Bernhard Fickl, Fabian Bohrn, Herbert Hutter, Benjamin Meier, Reinhard Kaindl, Bernhard C. Bayer, Dominik Eder. *V- and Al-free conformal atomic layer deposited TiO<sub>2</sub> diffusion-barrier-layers on porous 3D-printed TiVAI structures* (2024) – in preparation
4. **Jakob Rath et al.** *In-situ studies on the thermal degradation of NH<sub>2</sub>-MIL-125 during the SeLiRe (selective ligand removal) process using XRD, Raman and EXAFS.* (2024) – in preparation
5. **Jakob Rath, Jakob Blaschke**, et al. *In-situ studies on the thermal degradation of UiO-66 and NH<sub>2</sub>-UiO-66 using XRD, Raman and EXAFS.* (2024) – in preparation

## Secondary

1. Zheao Huang, **Jakob Rath**, Qiancheng Zhou, Alexey Cherevan, Shaghayegh Naghdi, Dominik Eder. *Hierarchically Micro- and Mesoporous Zeolitic Imidazolate Frameworks Through Selective Ligand Removal*. *Small* 20, 21 (2023), <https://doi.org/10.1002/smll.202307981>
2. Jasmin S. Schubert, Eva Doloszeski, Pablo Ayala, Stephen Nagaraju Myakala, **Jakob Rath**, Bernhard Fickl, Ariane Giesriegl, Dogukan H. Apaydin, Bernhard C. Bayer, Shun Kashiwaya, Alexey Cherevan, Dominik Eder. *Nature of the Active Ni State for Photocatalytic Hydrogen Generation*. *Advanced Materials Interfaces* 11, 3 (2023), <https://doi.org/10.1002/admi.202300695>
3. Pablo Ayala, Shaghayegh Naghdi, Sreejith P. Nandan, Stephen Nagaraju Myakala, **Jakob Rath**, Hikaru Saito, Patrick Guggenberger, Lakhanlal Lakhanlal, Freddy Kleitz, Maytal Caspary Toroker, Alexey Cherevan, Dominik Eder. *The Emergence of 2D Building Units in Metal-Organic Frameworks for Photocatalytic Hydrogen Evolution: A Case Study with COK-47*. *Adv. Energy Mater.* 13, 31 (2023), <https://doi.org/10.1002/aenm.202370133>
4. Hannah Rabl, Stephen N. Myakala, **Jakob Rath**, Bernhard Fickl, Jasmin S. Schubert, Dogukan H. Apaydin, Dominik Eder. *Microwave-assisted synthesis of metal-organic chalcogenolate assemblies as electrocatalysts for syngas production*. *Nature Com. Chemistry* 6, 43 (2023), <https://doi.org/10.1038/s42004-023-00843-3>
5. Tushar Gupta, Nicole Rosza, Markus Sauer, Alexander Goetz, Maximilian Winzely, **Jakob Rath**, Shaghayegh Naghdi, Andreas Lechner, Dogukan H. Apaydin, Alexey Cherevan, Gernot Friedbacher, Annette Foelske, Sarah M. Skoff, Bernhard C. Bayer, Dominik Eder. *Sonochemical Synthesis of Large Two-Dimensional Bi<sub>2</sub>O<sub>2</sub>CO<sub>3</sub> Nanosheets for Hydrogen Evolution in Photocatalytic Water Splitting*. *Adv. Sustainable Syst.* 6, 11 (2022), <https://doi.org/10.1002/adsu.202270026>

# Table of Content

1	Introduction and Motivation .....	3
1.1	Atomic Layer Deposition (ALD) .....	5
1.2	Metal-organic frameworks .....	10
1.3	Nano-Laminates .....	17
1.4	Passivation of micro-structured 3-D printed medical implants by use of ALD .....	19
2	Experimental Details .....	22
3	Atomic layer deposition of conformal Ti-MIL-125-like metal organic framework ultrathin films on nanoscaled substrates towards photocatalysis .....	24
3.1	Abstract .....	24
3.2	Introduction .....	24
3.3	Results and Discussion .....	28
3.3.1	Flat Si substrates. ....	29
3.3.2	Nanosopic ~500 nm diameter SiO <sub>2</sub> nanoparticle substrates. ....	37
3.3.3	Photocatalytic HER measurements.....	42
3.4	Conclusions .....	44
3.5	Methods.....	45
3.5.1	ALD. ....	45
3.5.2	Substrates. ....	46
3.5.3	Characterization.....	46
3.5.4	Photocatalytic HER tests. ....	48
3.6	Acknowledgements.....	49
3.7	Author Contributions .....	49
4	Synthesis of Metal-Organic-Framework Nano-Laminates by ALD.....	50
4.1	Abstract.....	50
4.2	Introduction .....	50
4.3	Experimental .....	54
4.4	Results and Discussion: .....	56
4.5	Conclustions .....	70
4.6	Methods.....	70
4.6.1	Laminate Synthesis. ....	70
4.6.2	Post deposition treatment .....	71
4.6.3	Substrates. ....	72

4.6.4	Characterization.....	72
4.7	Acknowledgements:.....	74
4.8	Author Contributions: .....	74
5	V- and Al-free conformal atomic layer deposited TiO <sub>2</sub> diffusion-barrier-layers on porous 3D-printed TiVAI structures .....	76
5.1	Abstract:.....	76
5.2	Introduction: .....	76
5.3	Experimental:.....	79
5.3.1	Synthesis: .....	79
5.3.2	Characterization:.....	80
5.4	Results and Discussion: .....	81
5.5	Conclusion:.....	90
5.6	Acknowledgments:.....	91
5.7	Author Contributions: .....	91
6	Summary and Outlook .....	92
7	Bibliography .....	94

# 1 Introduction and Motivation

The field of developing novel techniques for synthesizing, characterizing, and integrating new materials is currently among the most prominent areas of study in science.<sup>1,2</sup> It enables humankind to consistently enhance the ability to design and engineer compounds, ultimately leading to the production of nanoscale machines and tools, and materials with an expanding array of previously unattainable properties. For instance, even before the 2010 Nobel Prize in Physics was awarded to Andre Geim and Konstantin Novoselov for their discovery of single layer graphene, two-dimensional materials were attracting increasing interest due to their enormous range of outstanding properties.<sup>3</sup> The synthesis, characterization and implementation of these materials has become a huge field of materials science, constantly advancing our understanding of these building blocks. Today we have a vast zoo of different 2D materials that can be tailored, combined and modified to form components for future devices and revolutionize various sectors from catalysis towards semiconductor industries and medical applications.<sup>4</sup> The discovery of so-called MXenes by Yury Gogotsi and recent advances in their synthesis have highlighted the potential still hidden in this world of nanomaterials.<sup>4</sup> Although conventional approaches to material synthesis generally rely on solid or liquid state formation, gas phase methods such as chemical vapor deposition (CVD) and physical vapor deposition (PVD) have increasingly garnered attention over the past centuries.<sup>5,6</sup> Despite operating at relatively lower temperatures when compared to synthesis from a molten state, these techniques offer the potential to generate high-purity materials as thin film coatings on a diverse range of substrates, ultimately improving the electronic, mechanical, or catalytic properties of the bulk material.<sup>7-9</sup>

Development of high-end solutions for integration of such materials rapidly gained industrial interest in the latter half of the 20th century, particularly with advancements in high-vacuum pump manufacturing.<sup>5</sup> These developments enabled the construction of operational plants for large-scale synthesis of thin films through gas-phase reactions. Presently, techniques such as CVD and PVD are extensively utilized in semiconductor manufacturing, the aerospace industry, coating of cutting tools, and decorative applications.<sup>10-12</sup>

In gas-phase processes, one or more chemicals, known as precursors, are evaporated and transported onto the substrate surface using an inert gas stream, typically nitrogen or argon. In PVD, the evaporated target material is chemically identical to the desired material and can be achieved through heating, laser ablation, plasma discharge, or other methods.<sup>13</sup> Chemical vapor deposition employs a broader range of more volatile precursors, such as metal organics or amino compounds, which often react with another reactant to form a solid film on the substrate surface. In this case, the precursors and the final material are not chemically identical.<sup>14–16</sup>

As the range of materials accessible through gas-phase synthesis continues to expand, certain aspects related to mechanisms and reactor design have proven to be disadvantageous in practical applications. CVD is limited to highly volatile precursors, necessitating the development of new chemicals for synthesizing specific materials.<sup>17</sup> Contamination of these precursors can significantly impact film quality, and the high temperatures required in CVD processes restrict the range of suitable substrates for coating, even though researchers are constantly working on the improvement of low-temperature vapor deposition techniques.<sup>18–</sup>

22

In the case of PVD, the use of target evaporation to coat substrates highlights the need for highly uniform targets to ensure uniformity in the resulting film. Additionally, the target must be compatible with any of the aforementioned evaporation methods.<sup>23</sup>

Both CVD and PVD involve a trade-off between deposition rate and film quality. Higher deposition rates often lead to decreased film quality, characterized by increased roughness or reduced density. Striking a balance between deposition rate and film properties is critical and requires meticulous optimization. Furthermore, the coating of complex geometries is often challenging due to the line-of-sight transfer mechanism employed in most cases, particularly for PVD. A graphical presentation of this limitation is provided in Figure 1.1.<sup>24–26</sup>

Due to the limitations in uniformity when coating complex structures, first of all Russian and Finnish scientists independently started to work on a modification of CVD in order to produce highly uniform films with a thickness control down to the Angstrom region. These efforts lead

to manufacturing of the first commercial reactors for atomic layer deposition (ALD) in the 1990s.<sup>27</sup>

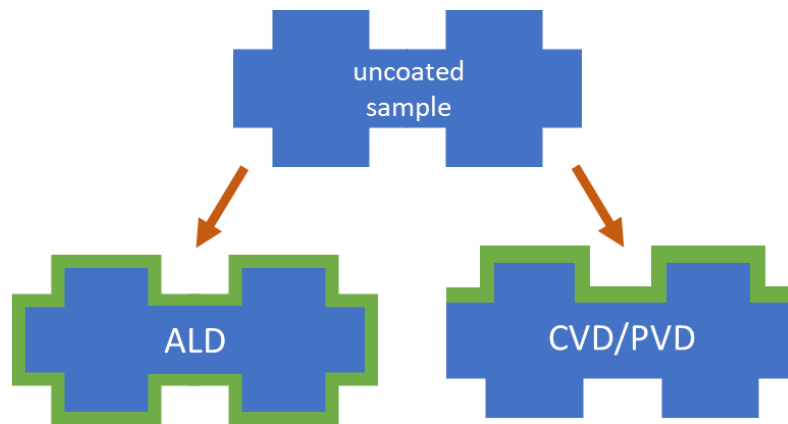


**Figure 1. 1:** Illustration of vapor-deposition based coatings. While ALD (left) offers the possibility to deposit highly uniform films on complex and intricate geometries, classical CVD as well as PVD (right) are limited in terms of uniformity by their line-of-sight transfer mechanisms – coatings are mainly formed on surfaces that face towards the target materials or flow direction of the chemical precursors.

### 1.1 Atomic Layer Deposition (ALD)

Atomic layer deposition (ALD) is a thin-film deposition technique that has been derived from classical chemical vapor deposition (CVD) which is designed for coating various substrates with conformal, dense and highly uniform thin films with incomparable quality. The method allows for the precise control of film thickness, composition, and uniformity, making it a valuable tool in a wide range of applications such as microelectronics, energy, and catalysis. The realm of materials attainable through atomic layer deposition synthesis encompasses a broad spectrum, spanning from elemental metals to oxides, nitrides, polymers, and progressively advancing towards increasingly intricate and multifaceted compositions, exhibiting an incessant expansion.<sup>28,29</sup>

ALD works by sequentially exposing a substrate to two or more precursor gases, each of which reacts with the surface in a self-limiting manner. This means that (in theory) only a monolayer

of material is deposited per cycle, ensuring ultimate thickness control. The reaction between the precursors and the surface is typically facilitated by a thermal or plasma process, which can be adjusted to achieve different film properties.<sup>30,31</sup> The following figures show schematic presentations of the experimental setup of an ALD reactor (Figure 1.2) and a simplified version of an ALD process (Figure 1.3) including pulses of  $\text{TiCl}_4$  and BDC (benzene dicarboxylic acid = terephthalic acid/TPA), two precursor chemicals used for synthesis of metal-organic-framework-type films, as explained later.

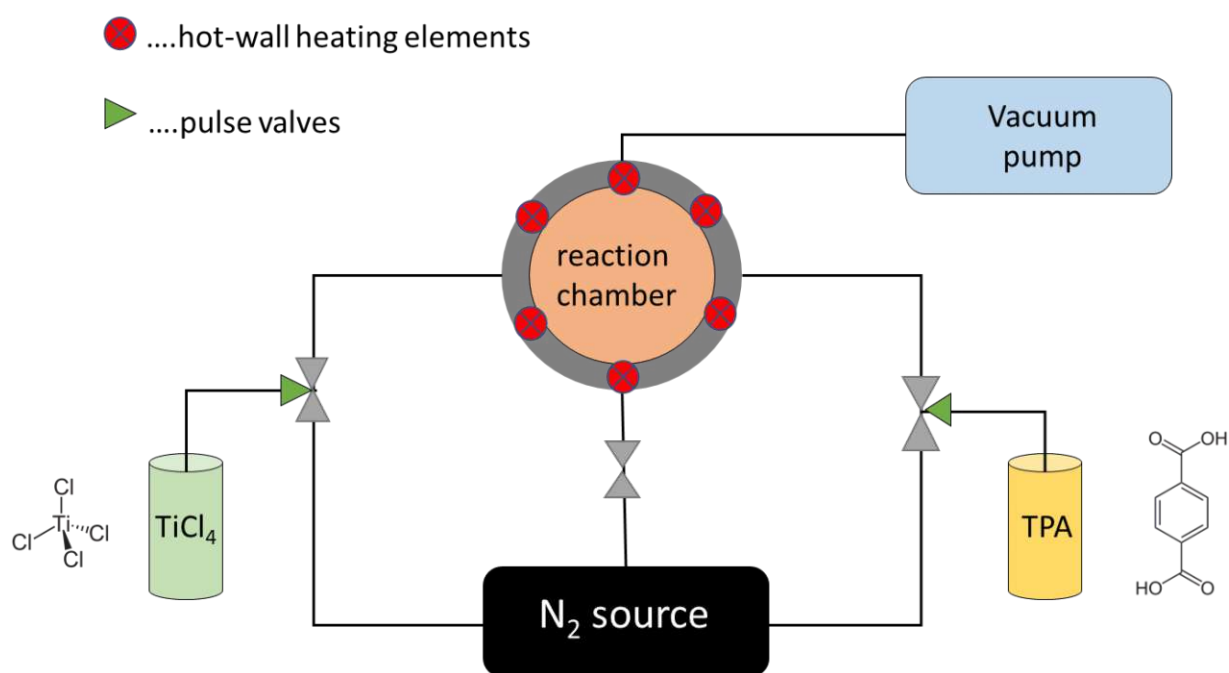


**Figure 1. 2:** Schematic of the ALD process for Ti-MIL-125 MOF deposition: The two precursors ( $\text{TiCl}_4$  and BDC/TPA) are alternately pulsed onto the substrate via pulsing valves. Nitrogen acts as a transport gas, as well as a purging gas in between the different precursor pulses. A dry pump keeps the pressure at about 1 mbar. The reaction chamber is heated by use of hot wall heating elements.

**Reaction schematic for one deposition cycle of Ti-MIL125**

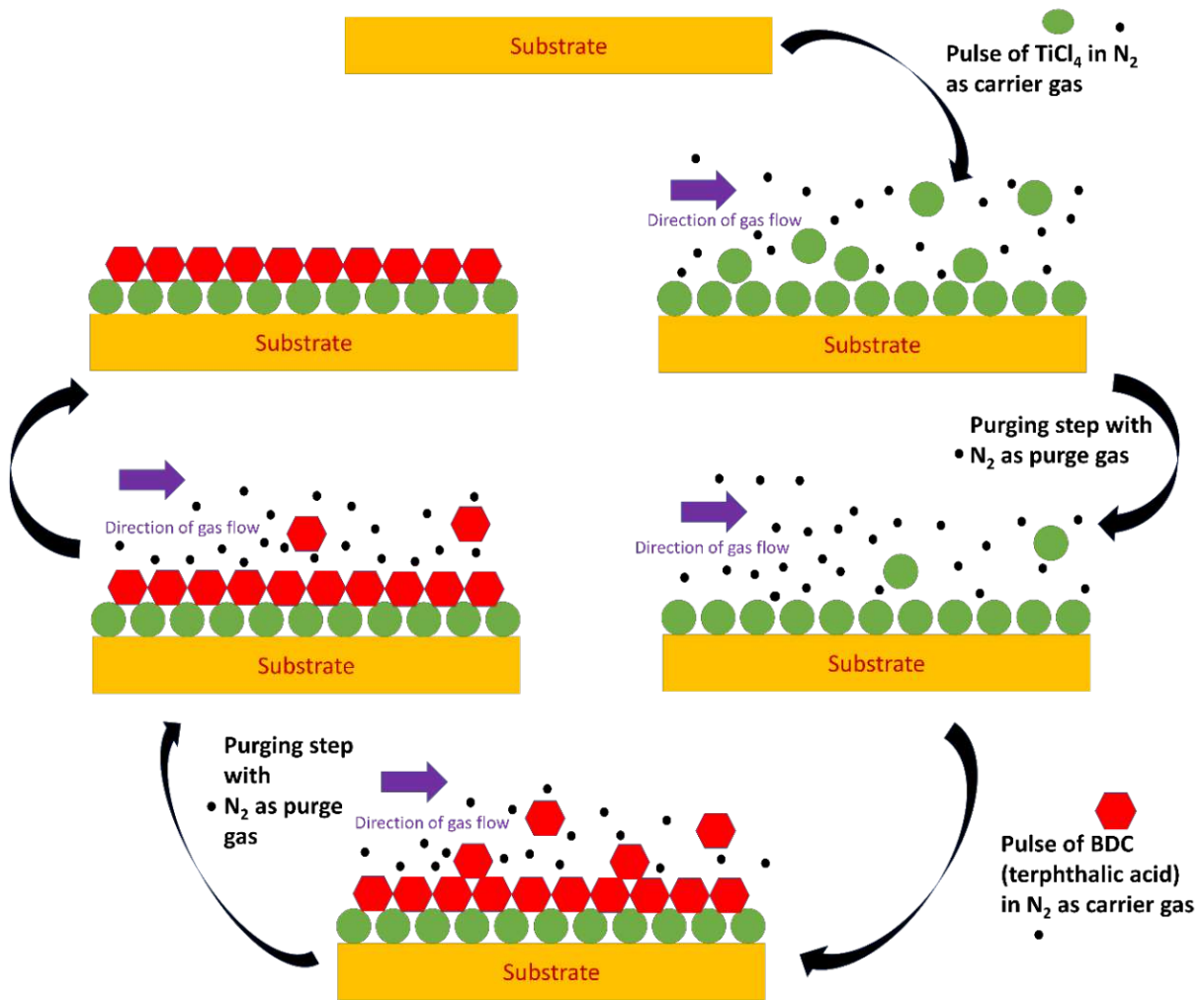


**Figure 1. 3:** Reaction schematic for an ALD process: After saturating the hot surface of the substrate with a monolayer of Precursor A (here  $\text{TiCl}_4$ ), a purging step with nitrogen removes excessive molecules. In the next step precursor B (BDC = benzene dicarboxylic acid) is pulsed into the chamber and saturates the surface and again, residual molecules of precursor are removed in a nitrogen stream forming one full layer of material

Atomic Layer Deposition (ALD) has its roots in the field of surface science and thin film deposition techniques. The concept of ALD originated in the late 1960s and early 1970s when researchers began to explore ways to deposit thin films with precise control over their

thickness and composition. The initial focus was primarily on the deposition of inorganic materials, such as oxides and nitrides.<sup>32</sup>

Early work on ALD focused primarily on developing methods for depositing thin films for microelectronic applications. In the 1970s, Finnish scientists Tuomo Suntola and Riikka Puurunen made significant contributions to the development of ALD. In particular, Suntola invented the first practical ALD reactor, known as the "Suntola reactor", in 1974. This reactor used a sequential and self-limiting gas-phase reaction mechanism to achieve atomic-scale control of film growth.<sup>33,34</sup>

In the 1980s and 1990s, ALD gained attention as a promising technique for depositing high-quality thin films in various industries, including microelectronics, optoelectronics and catalysis. The potential of ALD for the fabrication of complex multilayer structures and nanoscale devices became increasingly apparent. Silicon dioxide ( $\text{SiO}_2$ ) became a critical material for insulating layers in integrated circuits, and ALD offered superior thickness control and uniformity compared to conventional deposition techniques such as chemical vapor deposition (CVD). ALD-based deposition of  $\text{SiO}_2$  became an integral part of the microelectronics industry, paving the way for advances in chip manufacturing. In the late 1990s, ALD was successfully applied to the deposition of metals and metal nitrides, expanding the range of applications beyond insulating materials. Thin metal films synthesized by ALD exhibited excellent conformality, purity and electrical properties, making them suitable for interconnects, gate electrodes and catalysts.<sup>33</sup>

During the early 2000s, ALD made significant strides in the development of organic and hybrid materials. Organic-inorganic hybrid materials, such as metal oxides embedded in polymer matrices, were synthesized using ALD.<sup>35</sup> These materials combined the desirable properties of both organic and inorganic components, opening the door to applications in flexible electronics, photovoltaics, and sensing devices. Advances in ALD continued throughout the 2000s and 2010s, driven by the increasing demand for precise and conformal thin films in emerging fields such as nanotechnology and energy storage. Researchers explored new

materials, reaction chemistries, and deposition processes to expand the range of materials accessible with ALD.<sup>35–37</sup>

One of the key advantages of ALD is its ability to deposit conformal films, meaning that the coating can conform to the shape of the substrate, even on complex three-dimensional structures. This makes it particularly useful in the microelectronics industry for coating high aspect ratio structures, such as deep trenches and vias. In principle ALD even offers the possibility of coating nanoparticles and nanowires.<sup>38</sup>

In addition to its applications in microelectronics and nanomaterials, ALD is also being explored in energy applications. For example, ALD is being used to deposit thin films on battery electrodes to improve their performance and stability. ALD is also being investigated as a method of manufacturing solar cells, where it can be used to deposit high quality, uniform layers of material.<sup>39</sup>

Atomic layer deposition (ALD) is a rapidly advancing field, with new research topics emerging regularly. One area of current interest is the development of new ALD precursors that can offer improved performance and new capabilities.<sup>21</sup>

Another area of research is the development of new ALD processes that are more environmentally friendly. One approach being explored is the use of plasma-enhanced ALD (PEALD), which can reduce the use of harmful chemicals in the deposition process. PEALD is also being investigated for its ability to deposit films at lower temperatures, which can reduce energy consumption and improve the compatibility of ALD with temperature-sensitive substrates.<sup>40</sup>

Researchers are also focusing on using ALD to make flexible and stretchable electronics. By depositing thin films on flexible substrates, such as polymers or textiles, it is possible to create devices that can conform to the shape of the human body or other irregular surfaces. This has applications in areas such as wearable electronics, medical sensors, and robotics.<sup>41,42</sup>

Another area of interest is the use of ALD for the synthesis of new 2D materials, such as transition metal dichalcogenides (TMDs). TMDs have unique electronic and optical properties,

making them promising candidates for applications in electronics, photonics, and catalysis. ALD can offer provide control over the thickness and composition of TMDs, enabling the creation of new materials with tailored properties.<sup>43,44</sup>

In this work, we demonstrate new routes towards synthesis and integration of metal-organic framework (MOF) – like materials by using ALD, an area of growing interest with respect for renewable energy materials or applications in sensing or semiconductor fabrication.<sup>29,45,46</sup> A more comprehensive review of these materials is given in the following section of this work.

Overall, the field of ALD is constantly evolving, with new research topics and applications emerging on a regular basis. By continuing to explore the potential of ALD, researchers are opening up new possibilities for the fabrication of advanced materials and devices, with implications for a wide range of fields, from electronics to energy and medicine.

## 1.2 Metal-organic frameworks

Metal-organic frameworks (MOFs) are a class of materials that have gained significant attention in recent years due to their exceptional properties and wide range of potential applications. MOFs are composed of metal ions or clusters connected by organic ligands to form a porous and highly tunable framework. The unique properties of MOFs, including high surface area, high selectivity, and exceptional stability, make them ideal candidates for a variety of applications, such as gas storage,<sup>47,48</sup> catalysis,<sup>49,50</sup> sensing,<sup>51-53</sup> and drug delivery.<sup>54,55</sup> An overview of possible applications is given in Figure 1.4.

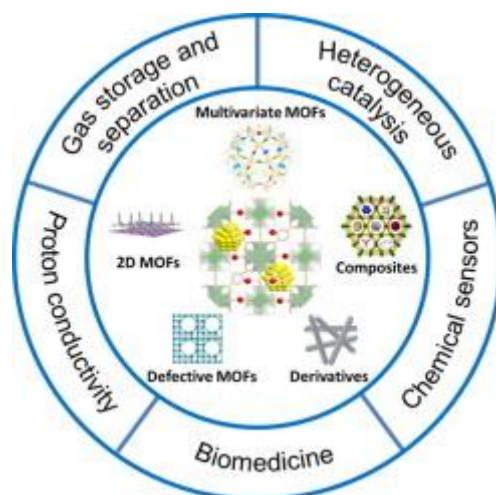


**Figure 1.4:** Graphical representation of possible applications of metal-organic-framework materials according to Jiao et al.<sup>56</sup>

The history of MOFs dates back to the early 20th century when zeolites, which can be considered as a precursor to MOFs, were first discovered. Zeolites are crystalline aluminosilicates with well-defined nanoporous structures.<sup>57</sup> In the 1990s, researchers began exploring the use of organic linkers to replace the inorganic components of zeolites, leading to the birth of MOFs as a distinct class of materials.

The first true MOF, called MOF-5, was reported in 1999 by Omar Yaghi and his team at the University of Michigan. This discovery marked a major breakthrough in the field, as it demonstrated the ability to construct highly ordered frameworks with large surface areas using coordination chemistry principles. The field rapidly expanded following this seminal work, with numerous research groups worldwide actively exploring the synthesis, characterization, and applications of MOFs.<sup>58</sup>

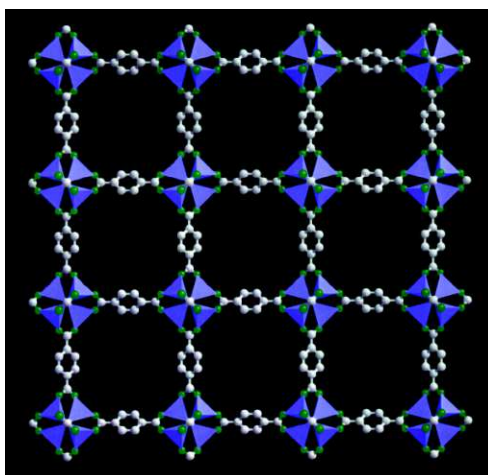


**Figure 1.5:** Representation of a {100} layer of the MOF-5 framework shown along the  $a$ -axis (C, grey; O, green) according to Li et al.<sup>59</sup>

In the early 2000s, researchers focused on developing new synthetic strategies to enhance the stability and functionality of MOFs. One significant development was the introduction of the concept of "reticular chemistry" by Yaghi and his collaborators. Reticular chemistry refers to the assembly of molecular building blocks into extended networks, enabling the design and synthesis of MOFs with targeted properties. This approach opened up new avenues for the creation of MOFs with tailored structures and functionalities.<sup>60,61</sup>

As the field progressed, researchers began exploring the potential applications of MOFs beyond gas storage. In 2005, one of the first examples of MOF-based catalysis was reported by researchers at the University of North Carolina. They demonstrated that MOFs could serve as effective heterogeneous catalysts for a range of chemical reactions, even highly complex stereoselective processes.<sup>62</sup> This discovery opened up new possibilities for MOFs in the field of catalysis, offering advantages such as high surface area, tunable pore size, and adjustable functionality.

In subsequent years, MOFs found applications in various areas. They were utilized as drug delivery vehicles, exploiting their large pore volumes and tunable properties to encapsulate and release therapeutic agents.<sup>54,63</sup> MOFs also proved valuable in gas separation processes, exhibiting high selectivity for specific gases due to their tailored pore sizes and surface

chemistry.<sup>64</sup> Additionally, MOFs showed promise in sensing applications, where their unique structures enabled the detection of target analytes with high sensitivity and selectivity.<sup>65</sup>

The development of MOFs continued to evolve, and in recent years, researchers have made significant advancements in the synthesis of novel MOFs with enhanced properties. This includes the design of MOFs with ultra-high surface areas,<sup>66</sup> exceptional stability in harsh conditions,<sup>67</sup> and improved gas storage capacities. Various strategies, such as post-synthetic modifications,<sup>68,69</sup> guest molecule exchange,<sup>70</sup> and mixed-metal/linker frameworks,<sup>71,72</sup> have been employed to tailor the properties of MOFs for specific applications.

Another noteworthy advancement in the field is the exploration of MOFs for energy storage and conversion.<sup>73,74</sup> Researchers have developed MOFs for applications in electrochemical energy storage devices such as batteries and supercapacitors. By incorporating redox-active metal centers and organic linkers with desirable properties, MOFs have demonstrated the ability to store and deliver electrical energy efficiently. These materials hold great potential for next-generation energy storage systems, offering high energy densities, long cycle lifetimes, and improved safety compared to traditional battery technologies.<sup>75</sup>

Moreover, MOFs have been investigated for their potential in photocatalysis and solar energy conversion. The combination of light-harvesting properties of the organic linkers and the redox capabilities of the metal centers allows MOFs to absorb light and facilitate charge transfer processes. This opens up opportunities for applications such as water splitting, carbon dioxide reduction, and photovoltaics, where MOFs can harness solar energy to drive chemical reactions or generate electricity.<sup>49,76,77</sup>

In recent years, efforts have been focused on scaling up the synthesis of MOFs,<sup>78</sup> improving their stability in various environments,<sup>67,79</sup> and exploring their integration into practical devices.<sup>80,81</sup> Researchers have developed techniques to produce MOFs on a larger scale while maintaining control over their structure and properties. Strategies such as thin-film deposition techniques,<sup>82</sup> surface modification<sup>83</sup> and MOF composites<sup>84</sup> have been employed to enhance their stability, making them suitable for real-world applications.

Additionally, advancements in computational modeling and artificial intelligence have facilitated the design and discovery of new frameworks with tailored properties. High-throughput screening methods and data-driven approaches have accelerated the identification of promising MOF candidates, significantly reducing the time and cost involved in materials development.<sup>85</sup>

Looking ahead, the field of MOFs continues to evolve rapidly. Researchers are actively exploring new synthesis methodologies, functionalization strategies, and applications for these materials in areas such as environmental remediation, sustainable chemistry, and beyond. With ongoing advancements, it is anticipated that MOFs will play a crucial role in addressing global challenges and revolutionizing diverse fields, ranging from energy and healthcare to environmental sustainability. This fact is displayed by the increasing amount of publications on metal-organic frameworks per year. While only about 100 papers were published in 2005 this number increased to well above 4.000 in 2019.<sup>86</sup>

One of the main areas of scientific interest in MOFs is their synthesis which is a complex process that requires a deep understanding of the interactions between the metal ions or clusters and the organic ligands. The synthesis of MOFs involves the assembly of these building blocks into a precise and controlled framework, which can be achieved through various methods such as solvothermal synthesis, hydrothermal synthesis, and microwave synthesis. Nowadays synthesis from gas-phase is another possible method to determine MOF-type materials with a unique set of properties.

Another major scientific interest that correlates with synthesis of these materials is the fact that MOFs can be tailored for specific applications by tuning their properties through various attempts like the choice of (mixed) metal ions or clusters and organic ligands but also through changing the synthetic routes towards enhanced properties.<sup>87,88</sup>

Also, the scalability of MOF synthesis is a critical factor in their commercialization. The development of large-scale synthesis methods that can produce MOFs in an efficient and cost-effective manner is a significant challenge. Therefore, research efforts are focused on

developing new synthetic strategies that can produce MOFs in large quantities without compromising their properties.<sup>89</sup>

Finally, the understanding of the fundamental principles underlying MOF synthesis is essential for the advancement of the field. Researchers are exploring the thermodynamics and kinetics of MOF formation to gain insights into the mechanisms underlying their synthesis. This understanding can lead to the development of new synthetic strategies and the optimization of existing methods.<sup>90–92</sup>

While solvothermal and microwave assisted techniques were the main synthetic routes towards creation of MOFs, vapor-based approaches have garnered increasing interest in the past decades.

The development of gas phase-based techniques for Metal-Organic Framework synthesis has emerged as an important area of research due to their advantages in achieving precise control over MOF properties and enabling scalability. Here is an overview of the most common techniques:<sup>93</sup>

- **Chemical Vapor Deposition (CVD):**  
MOF-Chemical Vapor Deposition involves the growth of a thin layer of metal oxide by PVD, CVD or ALD and subsequent MOF-formation by introduction of a gaseous linker onto the material film that leads to formation of a MOF-thin-film. CVD allows for the formation of MOF coatings with good adhesion and uniformity. It offers advantages such as the potential for large-scale production.<sup>20,94</sup>
- **Atomic Layer Deposition (ALD):**  
Atomic Layer Deposition, originally developed for ultra-thin film deposition, has been adapted for MOF synthesis. ALD involves sequential, self-limiting surface reactions, enabling precise control over film thickness and composition. By carefully selecting precursors, ALD enables the growth of MOF thin films with excellent uniformity and conformality on various, even highly complex substrates.<sup>46</sup>

Over time, these gas phase-based techniques have undergone advancements and refinements. Researchers have explored novel precursor chemistries, reaction conditions, and deposition methods to expand the scope and applicability of gas phase-based MOF synthesis. Additionally, there have been efforts to integrate these techniques with other fabrication processes to create hybrid structures and functionalize MOFs.<sup>29,93</sup>

When synthesizing MOFs from gas-phase approaches researchers often end up with so called amorphous Metal-Organic Frameworks (aMOFs) which are a unique class of materials that combine the characteristics of both amorphous solids and crystalline MOFs. While solvothermal frameworks are typically composed of metal ions or clusters connected by organic ligands, forming a highly ordered, porous and crystalline structure, amorphous MOFs however lack long-range order in their atomic arrangement, resulting in a disordered or glass-like structure. This disorder can occur at various length scales, ranging from short-range disorder to completely lacking any long-range order. Amorphous MOFs retain this porosity, albeit in a less ordered manner compared to crystalline ones. The lack of a well-defined crystal structure in amorphous MOFs can impart enhanced stability compared to their crystalline counterparts. The absence of specific crystal planes and the presence of disorder can make them less susceptible to structural changes caused by external factors such as temperature, pressure, or humidity.<sup>95,96</sup>

Amorphous MOFs offer unique opportunities in various applications. Their enhanced stability and porosity make them suitable for gas storage, separation, and catalysis. They can also be used as precursors for the synthesis of other materials or as matrices for encapsulating guest molecules. The disordered structure of amorphous MOFs can provide tunable properties, making them appealing for applications such as sensing, drug delivery, and energy storage.<sup>97-99</sup>

While amorphous MOFs are an exciting and emerging area of research, their study is still in its early stages. Researchers are exploring different synthetic strategies, characterizing their properties, and investigating their potential applications.<sup>95</sup>

The development of gas phase-based techniques for MOF synthesis has opened up new possibilities for tailoring MOF properties, such as pore size, surface area, and functionality, with precise control. Ongoing research aims to address challenges related to precursor reactivity, growth mechanisms, scalability, and reproducibility to further advance the field of gas phase-based MOF synthesis.

In this work in chapter 3, we develop an ALD process for conformal deposition Ti-MIL-125-like metal organic framework ultrathin films on nanoscaled substrates towards photocatalysis, which is the first demonstration of ALD of this MOF-type and also of photocatalytic use of ALD MOFs.

### 1.3 Nano-Laminates

Nano-laminates, layered structures composed of alternating nanoscale thin films, have emerged as a highly promising and versatile class of materials with unique properties and a wide range of applications. The following overview provides a detailed examination of the historical development, current applications, synthesis methods, future perspectives, and other relevant information regarding nano-laminates.

Nano-laminates consist of stacked layers of different materials with individual layer thicknesses typically in the range of a few nanometers to a few hundred nanometers. The precise control of layer thicknesses and composition in nano-laminates allows for the engineering of desirable properties, such as enhanced mechanical strength, improved electrical conductivity, tailored optical responses, and optimized chemical reactivity.<sup>100</sup>

The concept of nano-laminates originated in the early 1990s, driven by the need to improve the performance of thin film coatings and functional materials. Initial studies focused on fabricating alternating layers of metals and ceramics to achieve enhanced hardness and wear resistance. Over time, researchers explored various material combinations, such as metals, oxides, nitrides, and polymers, leading to the discovery of unique properties and expanded applications of nano-laminates.<sup>101</sup>

In this thesis, we present the first successful synthesis of nano-laminates based on MOF-like materials, accompanied by a comprehensive set of characterization techniques that contribute to a profound understanding of these films.

Nano-laminates find applications in diverse fields, including electronics, energy storage, catalysis, optics, and biomaterials.<sup>102,103</sup> In electronics, nano-laminates are utilized to fabricate high-performance transistors, memory devices, and sensors with improved electrical properties, reduced power consumption, and enhanced stability.<sup>104</sup> In energy storage, nano-laminates offer higher energy density and faster charging rates as electrode materials for batteries and supercapacitors.<sup>105</sup> Nano laminates also have significant applications in optical coatings, plasmonics, and photovoltaics, enabling precise control over light-matter interactions and improved device performance.<sup>106</sup>

Various synthesis methods are employed to fabricate nano-laminates, each offering specific advantages and control over layer thickness, composition, and interface quality. Common techniques include physical vapor deposition (PVD),<sup>107</sup> chemical vapor deposition (CVD),<sup>108</sup> sputtering,<sup>109</sup> electrochemical deposition,<sup>110</sup> and self-assembly approaches.<sup>111</sup> Atomic layer deposition (ALD) and molecular layer deposition (MLD) provide exceptional control over layer thickness and composition, enabling precise engineering of nano-laminates at the atomic level. Techniques such as co-sputtering,<sup>112</sup> electrochemical deposition, and Langmuir-Blodgett assembly offer additional versatility in designing nano-laminate structures.

The future of nano-laminates is very promising, with ongoing research focusing on several key areas. First, there is a growing emphasis on expanding the range of materials and layer combinations to explore new functionalities and applications. Tailoring interfaces and compositional gradients within such materials allows the creation of materials with unique electronic, thermal and mechanical properties. Second, advances in characterization techniques, computational modelling and fabrication methods will further improve our understanding of nano-laminates, enabling the design and optimization of tailored structures for specific applications. Third, nano-laminates are expected to play a crucial role in emerging

fields such as flexible electronics, bioelectronics and nanomedicine, where their tunable properties can be exploited to develop novel devices and systems.<sup>113,114</sup>

In summary, nano-laminates offer immense potential for engineered materials with exceptional properties due to their layered structure and the precise control of layer thickness and composition. With their diverse applications in electronics, energy, optics, catalysis and biomaterials, nano-laminates are poised to revolutionize many fields. Continued advances in synthesis techniques, material combinations and characterization methods will help to unlock the full potential of this subclass of materials, enabling the development of advanced technologies and addressing various societal challenges.

In this work in chapter 4, we focus on the development of MOF laminates consisting of two different ALD-synthesized MOF-type materials with similar building blocks. To the best of our knowledge, this is the first described route for such a material. In addition, we present a series of characterization techniques that allow a broad and thorough understanding of these systems.

#### **1.4 Passivation of micro-structured 3-D printed medical implants by use of ALD**

In recent decades, there has been a significant increase in research into the production of lightweight materials with excellent mechanical properties and high resistance to oxidation, even at elevated temperatures. Initially, this research was driven by the aerospace and automotive industries in the 20th century. More recently, however, there has been a growing interest in using these materials for biomedical applications, particularly as high-performance and durable implants.<sup>115</sup>

The most commonly used titanium alloy today is Ti-6Al-4V (Ti64), a high strength alloy containing 6% aluminium and 4% vanadium. It is used in a variety of industries, including the chemical, marine and aerospace sectors, as well as in the manufacture of implants and prostheses using techniques such as wrought, cast or additive manufacturing (e.g. LPBF – laser powder bed fusion).<sup>115,116</sup>

While Ti64 implants are widely used in the short term, concerns arise regarding the long-term utilization of these materials due to the toxicity of vanadium and aluminum, both in elemental form and as oxides, to the human body.<sup>117,118</sup> This has prompted the need to explore alternative alloys – essentially prohibitive Ti-Nb-alloys – or implement surface treatments to mitigate implant toxicity.<sup>119,120</sup> However, the complexity of achieving a uniform coating on complex three-dimensional structures presents a challenge for the second option.

Various methods, including solvothermal<sup>120</sup> and vapor deposition techniques (PVD/CVD), have been used to obtain coatings, but they exhibit limitations in terms of coating quality and uniformity due to their previously mentioned line-of-sight transfer mechanisms. The growth of materials not only occurs on the substrate surface but also in the gas phase, leading to edge-effects affecting the geometry of nanostructured objects.<sup>121</sup>

One promising technique to address these challenges is atomic layer deposition. ALD offers precise control over film thickness and uniformity, making it suitable for coating complex three-dimensional substrates with high-purity and atomically smooth material films. As the main component of the Ti64 alloy is biocompatible titanium, TiO<sub>2</sub> is as an ideal material for coating implants. Its strong ionic bonds also make it an excellent candidate for thin film diffusion barriers.<sup>122</sup>

Characterizing the effectiveness of ALD deposition is not straightforward due to the relatively high levels of titanium in both the substrate and the thin film. As a result, advanced surface analysis techniques such as X-ray photoelectron spectroscopy (XPS) and time-of-flight secondary ion mass spectroscopy (ToF-SIMS) are essential for predicting the quality of the barrier layer.

Despite the significant scientific and economic interest in this topic, there has been limited research on ALD-TiO<sub>2</sub> coating of 3D-printed Ti64-implant materials.<sup>123</sup> In this work in chapter 5, we aimed to demonstrate the general feasibility of ALD-thin-film coatings of TiO<sub>2</sub> on porous 3D-printed TiVAl structures. In addition, we demonstrated the homogeneity of the coatings and the absence of vanadium and aluminum within the top surface layers. Furthermore, a comparison between these results and the intrinsic formation of Ti/V/Al-oxides on 3D-printed

TiVAI structures by annealing at different temperatures is presented. Figure 1.6 illustrates the experimental strategies and the expected results of the different approaches to oxide film formation on the implant materials.

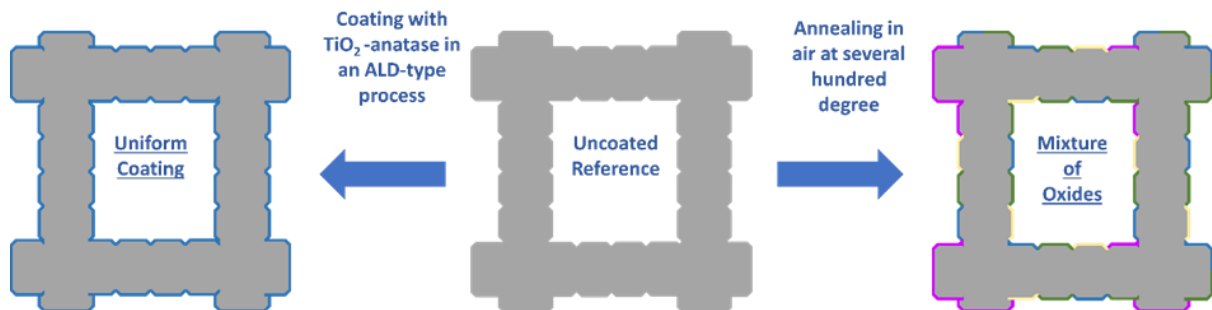


**Figure 1.6:** Graphic Representation of the two approaches used to form an oxide layer onto the 3D-printed TiVAI-implant-materials: coating of the material with TiO<sub>2</sub>-anatase, synthesized by use of ALD leads to formation of a dense, uniform film (left) whereas annealing of the uncoated samples at 300 and 700 °C leads to the formation of various oxides (Al, V, Ti) on the surface (right).

## 2 Experimental Details

The ALD configuration used in all the depositions discussed in this thesis is a Picosun R200 Advanced ALD system, connected to a 4.5 kW iXH 100 dry pump from Edwards, which is then connected to an ECO GEN2 nitrogen generator. This generator dilutes all exhaust gases with a stream of nitrogen gas (99.9% purity). The reactor enables the deposition of ultra-thin layers of material on a variety of substrates. Given its ability to accommodate up to nine independent precursors simultaneously (two solids, three liquids, four gases), the potential range of accessible materials and material combinations is enormous.



**Figure 2.1:** ALD-setup at TU Wien (E165, IMC) – from left to right: Picosun R200 Advanced ALD reactor with human interface; Edwards iXH 100 dry pump; ECO GEN 2 nitrogen generator

Although the provided setup for coating powders and other nanomaterials had some limitations in terms of flow dynamics and coating uniformity, we addressed these issues by using special particle coating moulds that were manually placed in the reaction chamber. A stream of nitrogen gas (99.99 % purity) was used to facilitate the purging and transport of precursors into the reaction chamber. A powder trap and afterburner, located between the

reaction chamber exhaust valve and the Edwards dry pump, ensured that no hazardous materials entered the laboratory exhaust lines.

To enhance safety, a system of interlocks was implemented to automatically shut down the process before any potential risk to the operator or others present in the laboratory could occur. In addition, a combination of manual and automated valves was used to prevent leakage of the precursors used.

A typical working routine for the synthesis of 2D materials using a Picosun R200 ALD reactor involves cutting silicon wafers and transferring the wafers and possibly other samples (such as powders or 3D printed monoliths) into the reaction chamber. After closing the hydraulic lid to the chamber, the reactor is evacuated and purged twice with N<sub>2</sub> before the heating elements mounted around the reactor heat the sample holder to the set temperature set in the human interface. After a short stabilization period, the manual valves between the ALD and precursor source bottles are opened and the programmed process begins. After cooling, the manual source bottles are closed, the system is purged with nitrogen gas and the coated material is removed. After the reactor has been pumped down again, all connected source lines are purged with a stream of N<sub>2</sub> and the system is fully operational again.

# 3 Atomic layer deposition of conformal Ti-MIL-125-like metal organic framework ultrathin films on nanoscaled substrates towards photocatalysis

## 3.1 Abstract

We report the deposition of ultrathin (30 nm to 150 nm thickness) and conformal Ti-MIL-125 metal-organic-framework (MOF) films by atomic layer deposition (ALD) on flat wafer substrates as well as on nanoscaled, complex shaped nanoparticle substrates. Notably, we find that our ALD MOF films show the signature of Ti-MIL-125 structure in Raman spectroscopy, while they appear amorphous in X-ray diffractometry (XRD) (i.e. are “XRD-amorphous”). Consequently, we assign to our ALD MOF films limited short range order and therefore label them as ALD “Ti-MIL-125-like” MOF films (in analogy to “diamond-like-carbon”). We demonstrate the deposition of the Ti-MIL-125-like ALD MOF films not only on planar Si wafer substrates but also on nanoscaled ~500 nm diameter SiO<sub>2</sub> nanoparticles, thus forming core-shell nanostructures with ALD Ti-MIL-125-like MOF coating shells. Finally, we also demonstrate the hitherto not explored potential of such ALD MOF coatings as photocatalysts for the hydrogen evolution reaction (HER) in photocatalytic water splitting.

## 3.2 Introduction

Metal-organic-frameworks (MOFs) are a subclass of coordination polymers consisting of nodes of metal ion(s) (clusters) that are coordinated by organic linker molecules in a crystalline lattice. MOFs exhibit a set of highly unique properties, incl. typically enormous

specific surface areas and high porosities that are tuneable by MOF composition.<sup>129</sup> Equally, via variation of metal node and linker species a variety of (opto-)electronic and catalytic properties can be readily engineered in MOFs. These characteristics directly lead to a very wide set of possible MOF applications from heterogeneous (photo-)catalysis,<sup>49,130,131</sup> gas separation/storage<sup>132</sup> and water purification<sup>133</sup> to (opto-)electronic device elements.<sup>53,134,135</sup> This has made MOFs one of the most researched topics in materials science in recent years. Notably, recently, besides variation of MOF chemical composition also variation of the crystallinity of a given MOF has been identified as another key parameter to modify MOF properties and further expand their application profile in so-called “amorphous MOFs” or “MOF glasses”.<sup>96,136–140</sup>

Historically, the synthesis of MOFs is based on wet-chemical hydrothermal and solvothermal techniques.<sup>129</sup> While readily applicable to synthesis of microscopic and macroscopic MOF powders, such wet-chemistry based techniques are often limited when wanting to deposit MOFs as thin films of ultra-low thickness conformally on complex three-dimensionally (3D) shaped substrates. Such conformally covering, ultra-thin MOF films would however be of key interest as (heterostructure) catalysts or in opto-electronic device applications.<sup>141,142</sup>

While wet-chemical layer-by-layer epitaxy towards so-called surface-coordinated MOFs (SURMOFs) is one possible way to deposit ultra-thin MOF thin films,<sup>143</sup> recently various solvent-free gas-phase synthesis approaches for MOF thin films emerged<sup>29,144</sup> incl. chemical vapor deposition (CVD)<sup>135,145,146</sup> or atomic layer deposition (ALD). The appeal of such solvent-free gas-phase growth of MOFs thin films is multifaceted: In particular, gas phase synthesis of MOFs intrinsically promises highly conformal MOF thin film growth even for complex, nanoscaled 3D substrates at high interface quality. Uniquely, gas phase techniques are expected to also be potentially able to coat nm-scaled high aspect ratio features that liquid deposition routes may not achieve. Gas phase techniques also open MOF deposition to substrates that are not compatible with wet-chemical processing due to e.g. substrate stability problems with capillary forces from solvent drying or other material incompatibilities.

Among the gas phase techniques, in particular ALD appears appealing (in the context of MOFs ALD is also often called molecular layer deposition (MLD)).<sup>29,144</sup> In ALD of MOFs the precursors

for the metal nodes and the linkers are typically separately pulsed over the substrates (Figure 3.1a), leading to conceptionally ideally self-limiting growth of only one molecular adsorbate layer in each pulse half-cycle to react with each other at molecular precision upon the subsequent pulse to form ideally only one monolayer unit of MOF per cycle. Thereby, ALD promises precise thickness control down to Å-resolution, very high interface-quality and intrinsic conformal coating of complex-shaped 3D substrates. ALD can also offer benign deposition conditions that are compatible with a large variety of substrates and uses an industrially scalable technology platform. Consequently, a number of reports have to date investigated the deposition of various MOF films by ALD incl. Zn-MOF-5, Zn-IRMOF-8, Zr-Uio-66 and other hybrid mixed organic/inorganic structures.<sup>46,147–155</sup>

Notably, in these prior studies one drawback of ALD MOF deposition is that the initial product film is typically found to be of amorphous MOF or MOF glass structure, which only sometimes can be crystallized in subsequent vapor annealing or autoclaving steps.<sup>46,147,148,150–152,155</sup>

One highly interesting MOF that to date has not been deposited by ALD is Ti-MIL-125 (Figure 3.1b) with composition  $\text{Ti}_8\text{O}_8(\text{OH})_4[\text{O}_2\text{C}-\text{C}_6\text{H}_4-\text{CO}_2]_6$ , consisting of  $(\text{Ti}_8\text{O}_8(\text{OH})_4)$  clusters held together by benzene-dicarboxylic linkers. Ti-MIL-125 is one of the most promising MOFs in the field of photocatalysis, in particular for photocatalytic water splitting towards sustainable green hydrogen production.<sup>49,131</sup> All prior work in photocatalytic water splitting with Ti-MIL-125 MOF (incl. several prior works by TU Wien) has however only utilized wet-chemistry grown Ti-MIL-125 MOF powders.<sup>49,131</sup> Conformally deposited thin films of Ti-MIL-125 MOF would however allow realization of novel photocatalyst concepts and form factors such as nanoscaled heterostructure photocatalysts to allow efficient charge separation across component junctions.<sup>141,142</sup> Such conformal ultra-thin films have to date however not been realized for Ti-MIL-125. In fact, conformal coating of nanoscale objects with films of any MOF structure by gas-phase techniques remains underdeveloped.

Filling this gap, we here report the deposition of ultra-thin, conformally coating Ti-MIL-125 MOF films by ALD on both macroscopically flat native oxide-covered Si wafer substrates as well as on nanoscaled ~500 nm diameter  $\text{SiO}_2$  nanoparticles (Figure 3.1c). We employ simple  $\text{TiCl}_4$  and terephthalic acid (TPA, also called 1,4-benzene-dicarboxylic acid, BDC) precursors

and deposit films from 30 nm to 150 nm thickness at substrate temperatures around 260 °C. Notably, we find that our films show signs of Ti-MIL-125 structure in Raman spectroscopy, while the films appear amorphous in X-ray diffractometry (XRD) (i.e. are “XRD-amorphous”). Consequently, we assign to our ALD MOF films limited short range order and therefore label them as ALD “Ti-MIL-125-like” MOF films (in analogy to “diamond-like-carbon”<sup>156,157</sup>). We further demonstrate that we can deposit the Ti-MIL-125-like ALD MOF films not only on planar Si wafer substrates (Figure 3.1c, left) but also on nanoscaled ~500 nm diameter SiO<sub>2</sub> nanoparticles, thus forming unprecedented sub- $\mu\text{m}$  core-shell nanostructures with ALD Ti-MIL-125-like MOF shells (Figure 3.1c, right). Finally, we also explore the potential of these ALD Ti-MIL-125-like MOF films (with Pt co-catalysts<sup>49,131</sup>) as photocatalysts for the hydrogen evolution reaction (HER) in photocatalytic water splitting, which to date has not been reported in the literature for any ALD MOFs.

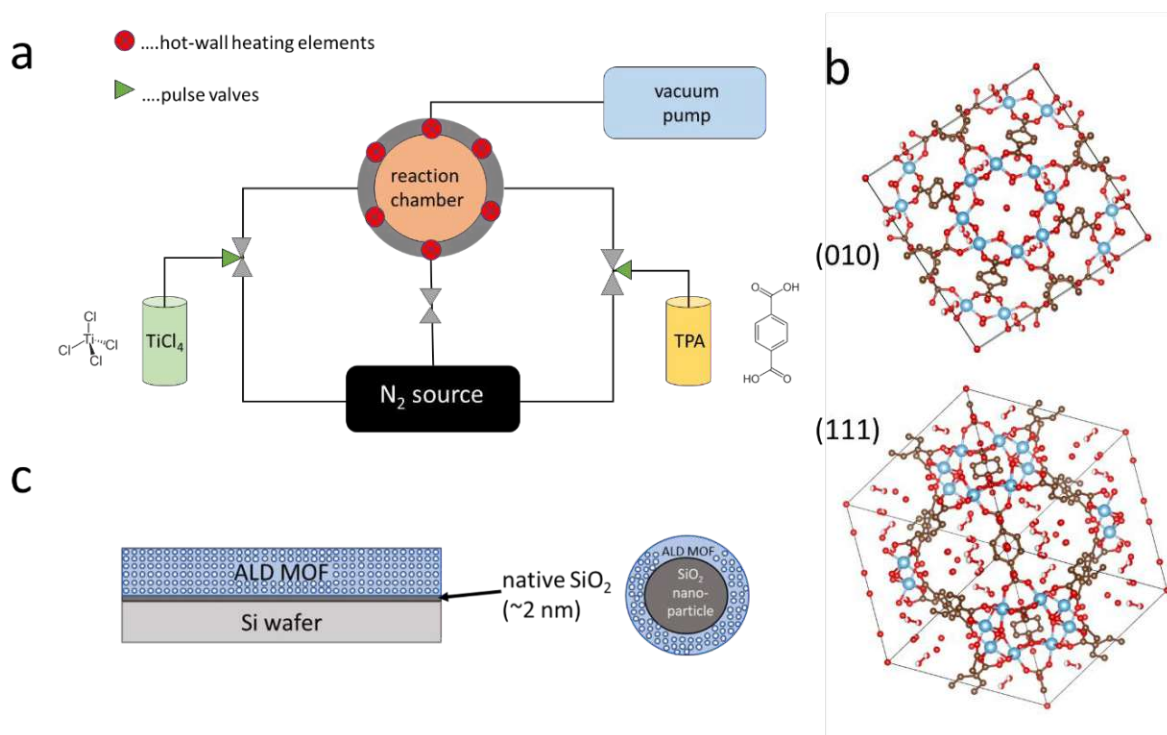


**Figure 3. 1:** (a) Schematic of the ALD process for Ti-MIL-125 MOF deposition: The two precursors ( $\text{TiCl}_4$  and TPA) are alternately pulsed onto the substrate via pulsing valves. Nitrogen acts as a transport gas, as well as a purging gas in between the different precursor pulses. A dry pump keeps the pressure at about 0.1 mbar. The reaction chamber is heated by hot wall heating elements. (b) Atomic sketch of Ti-MIL-125 structure, showing typical (010) and (111) planes. Blue atoms represent Ti, red O and brown C, respectively. The sketch was made using an ICSD structure file<sup>158</sup> and the software VESTA.<sup>159</sup> (c) Schematic view of the two different types of substrates utilized in our experiments: Si wafer piece with ~2 nm of native  $\text{SiO}_2$  (left) and sol-gel synthesized ~500 nm diameter  $\text{SiO}_2$  nanoparticle (right).

### 3.3 Results and Discussion

All ALD depositions were performed in a Picosun R200 Advanced ALD-reactor, equipable with up to 9 precursor sources (solid, liquid, gaseous). The system is pumped to a base pressure (without pulsing) of 0.1 mbar. The synthesis procedure for Ti-MIL-125 involved alternating pulse-purge-cycles of two precursors, namely vapors from liquid  $\text{TiCl}_4$  (99.7% purity) and solid

TPA (99% purity). For  $\text{TiCl}_4$  feeding, only the room temperature vapor pressure of liquid  $\text{TiCl}_4$  ( $\sim 13$  mbar) was used.<sup>160</sup> For TPA feeding, the solid precursor material was heated in its source to  $165$  °C, resulting in a vapor pressure of  $\sim 1$  mbar.<sup>46,161</sup> It is important to note that pulsing valves and lines in our ALD system are heatable to avoid re-condensation of precursor vapor in lines and pulsing valves. For TPA we set line and pulsing valve heating to  $175$  °C to avoid condensation. A flow of  $\text{N}_2$  gas (5.0 purity) was applied as both transport gas for the precursors to the substrate and as purging gas between pulses (250 sccm). We employed a pulse-purge sequence of 20 s TPA – 40 s purge – 4 s  $\text{TiCl}_4$  – 8 s purge, which we ensured to be well above the saturation range when comparing with experimental results using XRR as well as literature data.<sup>46</sup> We base this selected pulsing pattern on inspection of established protocols for  $\text{TiO}_2$  deposition in our ALD reactor<sup>162</sup>, adjusted by prior literature on MOF ALD.<sup>46</sup> Film thicknesses are controlled via the number of pulse cycles (see below). The substrates are heated in the ALD chamber via a hot-wall heater arrangement. We initially screened a substrate temperature range of  $210$  °C to  $310$  °C. The lower limit ( $210$  °C) resulted from selecting a sufficiently high temperature to safely avoid physical re-condensation of the TPA. The upper limit ( $310$  °C) resulted from the maximum heating temperature our system can achieve. From initial ALD deposit characterization we obtained Raman signatures for best MOF crystallization (Figure 3.5a) for a substrate temperature of  $260$  °C, which we therefore investigate as substrate temperature for the remainder of this study. We attribute the limited stability of the MOF films at substrate temperatures  $< 260$  °C in Figure 3.5a to insufficient energy provided for proper MOF formation, while the low Raman signal at temperatures  $> 260$  °C in Figure 3.5a is assigned to onset of thermal MOF degradation via linker labilization. The observation of a narrow intermediate temperature range for successful MOF ALD is in line with prior literature on other MOFs.<sup>46</sup>

### 3.3.1 Flat Si substrates.

We first focus on development of an ALD process for Ti-MIL-125 deposition on the macroscopic, planar Si wafer substrates (Figure 3.1c, left). This is because ALD on planar substrates is much more established, largely due to easier control of precursor flow patterns.<sup>163</sup> In contrast, ALD on nanoscopic powder substrates such as the  $\sim 500$  nm  $\text{SiO}_2$

nanoparticles (Figure 3.1c, right) can be challenging even for well-established ALD materials like oxides due to more complex flow dynamics.<sup>163</sup>

Figure 3.2a shows optical photographs of Si wafer pieces before (left) and after our ALD process (right). The change in color of the sample after deposition of 1000 pulse cycles (right) is clearly visible optically and indicative of a homogeneous film deposition laterally on a cm scale. Figure 3.2b shows a corresponding scanning electron microscopy (SEM) image of the as-deposited film, indicating an overall homogeneous and on a nm-scale flat morphology with only few ~500 nm wide slightly protruding growth features superimposed. Such morphology has been reported previously for other ALD MOF films on flat substrates.<sup>46</sup>

To check for successful deposition of the Ti-MIL-125 MOF, we check via X-ray photoelectron spectroscopy (XPS) the corresponding Ti2p, O1s and C1s core levels of the as-deposited films in Figure 2.2c. We find that the peak shapes and positions are in excellent accordance with literature on XPS characterization of Ti-MIL-125.<sup>49,164,165</sup> Notably, the observed Ti2p and O1s spectra exclude the formation of TiO<sub>2</sub> as an undesired (side-)product in our ALD MOF films.<sup>49,166</sup> Elemental quantification of the as-deposited ALD films from XPS (Table 3.1) shows good accordance with the Ti:O:C stoichiometry compared to nominal Ti-MIL-125 composition, albeit a small level of excess TPA linker presence is detected in addition to the Ti-MIL-125 stoichiometry. We note that some of the oxygen in the (Ti<sub>8</sub>O<sub>8</sub>(OH)<sub>4</sub>) clusters is likely to stem from partial TPA dissociation and rearrangement.

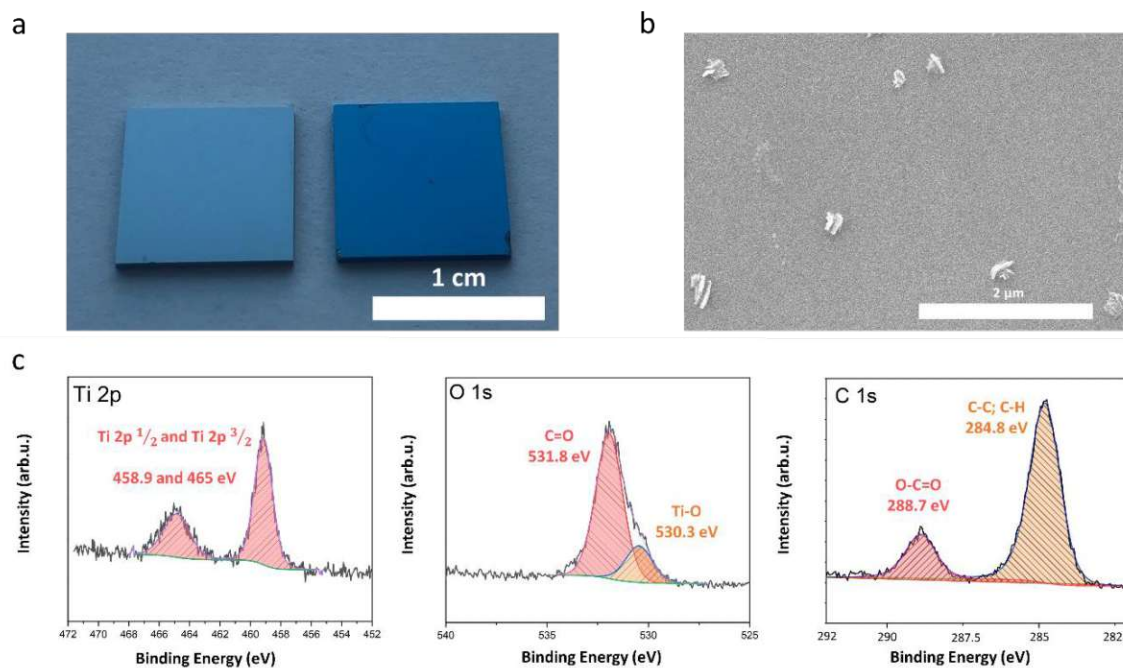


**Figure 3. 2:** (a) Photograph of a bare Si wafer (left) and a Si wafer covered with as-deposited 1000 pulse cycles of ALD MOF (right). (b) Corresponding scanning electron microscopy (SEM) image of the as-deposited film, indicating an overall homogeneous and on a nm-scale flat morphology with only few ~500 nm wide slightly protruding features superimposed. (c) XPS of the corresponding Ti2p, O1s and C1s core levels. The peak shapes and positions are in excellent accordance with literature on XPS characterization of Ti-MIL-125 powder.<sup>49,164,165</sup>

	<i>C/O</i>	<i>C/Ti</i>	<i>Ti/O</i>
<b>measured elemental ratios</b>	2.00	7.08	0.28
<b>nominal elemental ratios</b>	1.33	6.00	0.22

**Table 3. 1:** Quantification results determined by XPS. After peak-fitting and removal of the signals caused by adventitious C, the elemental ratios calculated were compared to the nominal composition of Ti-MIL-125, showing generally very good agreement, indicative of successful Ti-MIL-125 deposition by ALD. The values for C/O and C/Ti measured with XPS are however somewhat higher than the nominal concentration, indicating an access of TPA linker present within the ALD MOF film.

Figure 3.2 has so far revealed that we have deposited homogeneous, flat films with an overall composition and chemical states corresponding to Ti-MIL-125 via our ALD process. To understand the structure of the deposited film we present in Figure 3.3a Raman spectroscopy measurements of the ALD MOF films (blue and red traces), referenced also against solvothermally produced high-quality Ti-MIL-125 microcrystal powders (black trace)<sup>49</sup> and neat TPA powder (gray trace).<sup>164,167–169</sup> Expected Raman peak positions for crystalline Ti-MIL-125 (black trace) are at  $\sim 1147$ ,  $\sim 1435$ ,  $\sim 1451$  and  $\sim 1617$   $\text{cm}^{-1}$ .<sup>170</sup> These are linked to the vibrational modes of the TPA-linker in the Ti-MIL-125 structure, in detail the symmetrical and asymmetrical vibrational modes of the COO-group, as well as the vibrational modes of the C-H and C=C bonds.<sup>165</sup> For the as-deposited ALD MOF films from 260 °C substrate temperature (blue trace) we measure broad Raman bands around these positions in Figure 3.3a. The position and broadness of the bands for the as-deposited ALD MOF films would be consistent with a Ti-MIL-125 structure of a low degree of crystallization.<sup>166</sup> We also note that additional Raman data in Figure 3.5b further excludes (in line with the XPS above) that  $\text{TiO}_2$  was formed as an undesired (side-)product in our MOF ALD process.

What is however complicating a structural assignment is that neat TPA (i.e. that is not placed as linker within a crystalline Ti-MIL-125 structure) has Raman bands (grey trace in Figure 3.3a) at positions that are also close to those of Ti-MIL-125.<sup>49,169</sup> We therefore employ post-deposition washing of the as-deposited films in Dimethylformamide (DMF) which is a known solvent that dissolves neat TPA but not Ti-MIL-125 MOFs.<sup>171</sup> We find that this washing via DMF soaking for >24h improves the structural Raman fingerprints of our ALD MOF films, as observed by sharpening of the peaks in Figure 3.3a (red trace). Notably this DMF washing leaves the optical appearance of the ALD MOF films without signs of dissolution of the deposited material (photograph in Figure 3.4). We suggest that via this DMF washing the majority of excess TPA that is not linked into Ti-MIL-125 structure is removed from the deposits (with a small amount of excess TPA remaining as seen by the minority peak  $\sim 1300$   $\text{cm}^{-1}$  in the red trace in Figure 3.3a). We find that this treatment also allows the ALD MOF deposits to further crystallize via the soaking (which is in line with prior work on other ALD MOFs<sup>46</sup>). The Raman signal of ALD MOF deposits after DMF washing in Figure 3.3a (red trace) is thus indicative of Ti-MIL-125 structure for our ALD MOFs, albeit of lower degree of

crystallization compared to solvothermal Ti-MIL-125 (black trace in Figure 3.3a), as evidenced by the still much wider peaks in the red trace. Consistent with this low degree of crystallization from Raman measurements, corresponding X-ray diffractometry (XRD) measurements (Figure 3.3b) did not exhibit reflections<sup>96,136,138</sup>, neither for as-deposited nor DMF-soaked films. This indicates that our ALD films are “XRD-amorphous”. Raman is generally more sensitive towards even shorter range ordering than XRD, and thus evidence of structure in Raman spectroscopy but its absence in XRD typically indicates presence of a certain structure at only short range order (i.e. low crystallinity).<sup>172</sup>

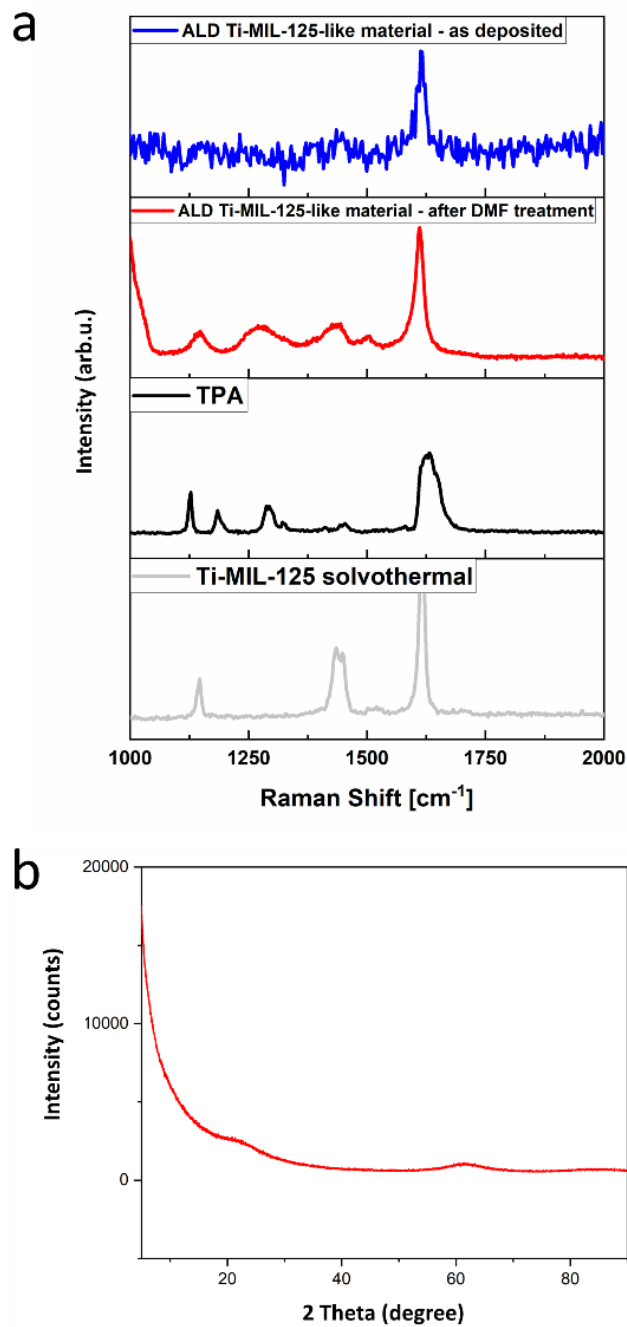


**Figure 3. 3:** (a) Raman spectra of ALD MOF film as-deposited (blue) and after treatment with DMF (red) as well as a reference spectrum of solvothermal synthesized Ti-MIL-125 (black) and neat TPA (grey). Spectra plotted to lower wavenumbers and additional Raman data are shown in Figure 4. (b) XRD diffractogram of an as-deposited ALD MOF film. The absence of any sharp reflexes indicates that there is no long-range order within the ALD MOF film, i.e. it is “XRD-amorphous”.

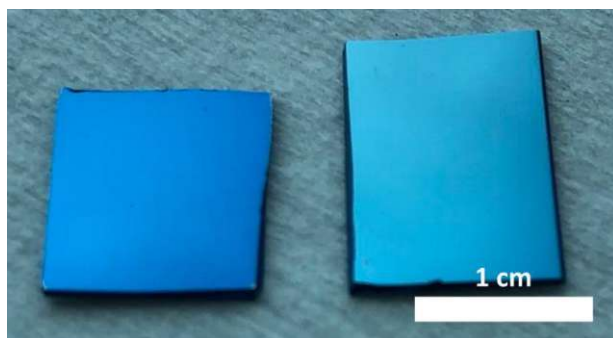


**Figure 3. 4:** Photograph of a Si wafer coated with 1000 pulse cycles of ALD MOF films as deposited (left) and after long-term DMF-washing (right); note that both samples appear visually blue and dull while a bare Si wafer shows a shiny silvery surface.

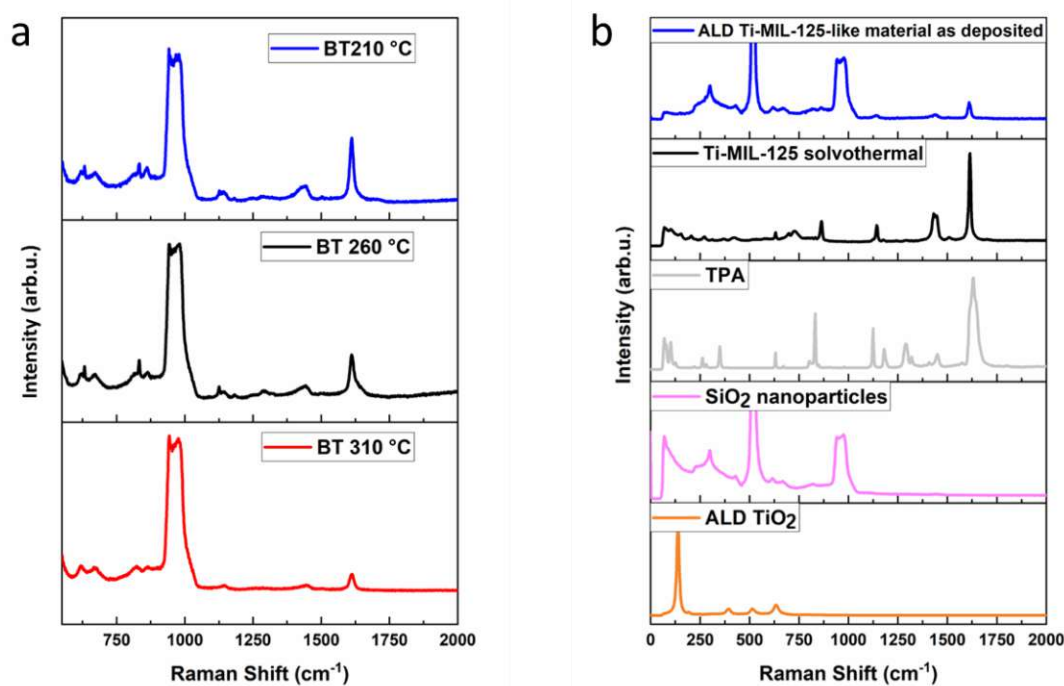


**Figure 3. 5:** a - Raman spectra obtained on ( $\sim 500$  nm) silica particles coated with 1000 pulse cycles of  $\text{TiCl}_4$  and TPA at various temperatures. While the material synthesized at  $210^\circ\text{C}$  shows signals in the range of expected transitions of Ti-MIL-125, the film deposited at that temperature dissolves in DMF and any signals present vanish upon DMF washing. Conversely, the film deposited at  $310^\circ\text{C}$  shows reduced signs of crystallinity in terms of Raman signatures. The film deposited at  $260^\circ\text{C}$  combines a good signal and remains fully stable upon DMF washing, thus identifying  $260^\circ\text{C}$  as ideal deposition temperature under our conditions. All

further detailed experiments were therefore carried out at 260 °C deposition temperature. b - Raman spectra of from top to bottom: ALD MOF film, as deposited on (~500 nm) silica nanoparticles (blue), solvothermal synthesized Ti-MIL-125, neat TPA powder, bare silica nanoparticles as reference, ALD TiO<sub>2</sub>. The ALD TiO<sub>2</sub> was similarly deposited at ~260 °C using TiCl<sub>4</sub> and water in the same ALD system. The ALD TiO<sub>2</sub> shows a Raman fingerprint consistent with anatase (REF).<sup>1</sup> Notably, absence of the strongest anatase peak (E<sub>g</sub>) at 145 cm<sup>-1</sup> in the Raman spectra of the ALD MOF excludes the presence of TiO<sub>2</sub> as an undesired (side-)product in the ALD MOF films. The data shown in this figure is similar to Figure 3a but shows the Raman spectra over the full range.

Combining the morphological, compositional and structural characterization data so far, suggests that we have in our ALD process deposited homogeneous, flat MOF films with a composition consistent with Ti-MIL-125 and a structure that corresponds to Ti-MIL-125, albeit at low structural order. Due to this limited short range order of Ti-MIL-125-type in our films, we terms these as “Ti-MIL-125-like” MOF films (in analogy to “diamond-like-carbon”<sup>156,157</sup>).

We provide further assessment of our Ti-MIL-125-like ALD MOF films by studying their growth-per-cycle characteristics which are key parameters in ALD film growth development. To this end we employ X-ray reflectivity (XRR) which gives us access to thickness and density of the ALD films on the Si-wafer substrates. Figure 3.6a shows two exemplary XRR measurements for 500 and 1000 pulse cycle depositions, respectively. Plotting XRR-derived thicknesses for depositions ranging from 500 to 2500 pulse cycles indicates linear growth behavior and allows calculation of the growth-per-cycle via a linear fit (Figure 3.6b), which yields a growth-per-cycle of ~0.58 Å per cycle for our conditions at 260 °C. Notably our XRR data in Figure 6b shows that we can controllably deposit the Ti-MIL-125-like ALD MOF films in a range of ultra-low thickness from ~30 to 150 nm. Concurrent XRR-based estimation of the density of the films yields values ranging 1.73 to 1.89 g/mL which compares well with the nominal density of Ti-MIL-125 of 1.66 g/mL (calculated via structure file<sup>158</sup>) as well as the density of 1.84 g/mL measured on the isostructural MOF Ti-NH<sub>2</sub>-MIL-125 using He-

pycnometry.<sup>173</sup> This excellent agreement in film density values further corroborates our structural assignment of our ALD MOF films to Ti-MIL-125-like structure.

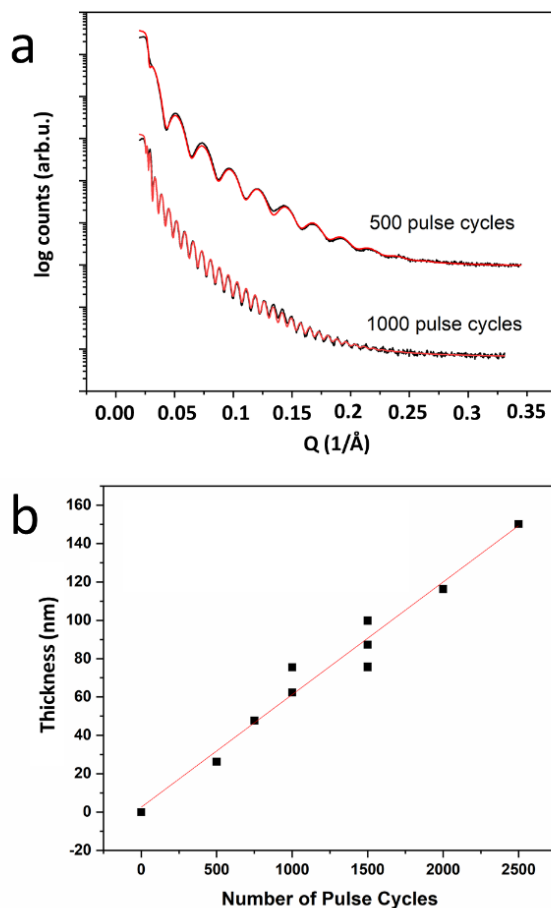


**Figure 3. 6:** (a) XRR data obtained for two ALD films deposited with 500 and 1000 pulse cycles, respectively. The black dots are the experimental data points, the red curve shows the fitted graph. (b) Linear fit for thickness-values obtained by use of XRR for samples covered with 500 to 2500 deposition cycles, the slope of this fit (0.59 Angstrom per cycle) is referred to as growth per cycle value.

### 3.3.2 Nanoscopic ~500 nm diameter SiO<sub>2</sub> nanoparticle substrates.

All so far presented ALD MOF films in this study were deposited onto macroscopic, planar Si wafer substrates. Such mirror-polished flat substrates however do not make use of ALD's key

advantage of potentially conformal coating of nanoscaled objects.<sup>141,163</sup> Therefore, we in the following present data on ALD MOF deposition on nanoscopic  $\sim 500$  nm diameter  $\text{SiO}_2$  nanoparticles. For a transmission electron microscopy (TEM) image of such  $\text{SiO}_2$  nanoparticles before ALD see Figure 3.7. A similar ALD coating with a layer of Titania of nanoparticles is displayed in Figure 3.8. Note in this context that ALD onto nanoscopic powders is still an active emerging area in research in itself and remains underdeveloped even for standard ALD materials such as oxides,<sup>163</sup> let alone for MOFs by ALD.

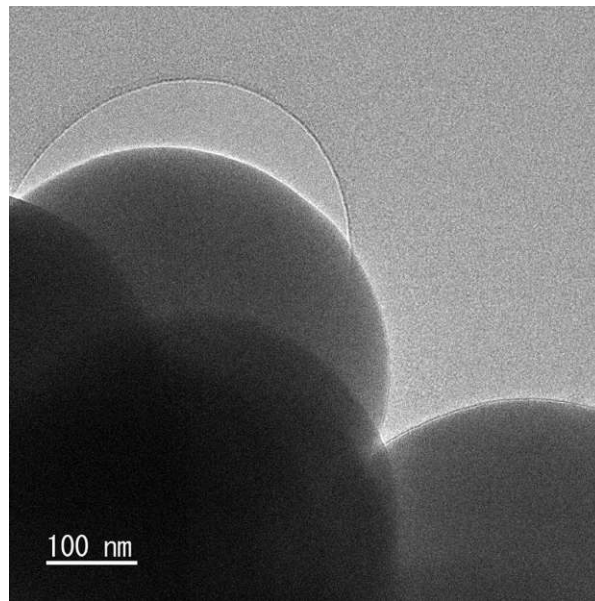


**Figure 3. 7:** Bright-field TEM image of as synthesized, uncoated  $\text{SiO}_2$  nanoparticles used for later powder coating with MIL-125-like material (and reference  $\text{TiO}_2$  as shown in Figure 2.8) by ALD.

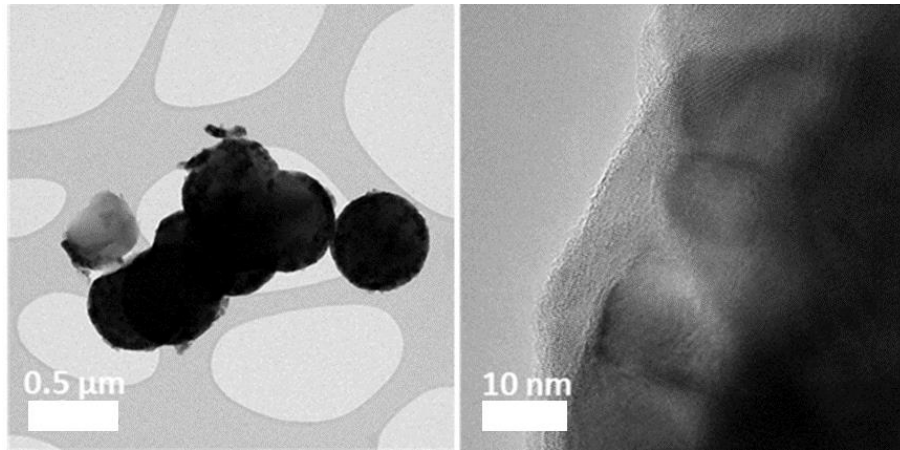


**Figure 3. 8:** TEM images of ALD TiO<sub>2</sub> coating on SiO<sub>2</sub> nanoparticles whereby the ALD coating was similarly deposited at ~260 °C using TiCl<sub>4</sub> and water in the same ALD system. This results in more or less homogeneous nanocrystalline TiO<sub>2</sub> coatings on the SiO<sub>2</sub> nanoparticles with similar thickness to the ALD Ti-MIL-125-like material. Due to epitaxial growth mechanism of ALD the uniformity of the coating is reduced when comparing to an amorphous material.

Figure 3.9a shows a scanning transmission electron microscopy (STEM) image of a SiO<sub>2</sub> nanoparticle after our MOF ALD process, acquired via high angle annular dark field (HAADF) mode, which provides mass-thickness contrast.<sup>174</sup> Thus the HAADF image in Figure 3.9a already indicates a clear core-shell structure, which is absent in the uncoated particles (Figure 3.7). Notably the lower HAADF intensity in the shell indicates that the shell is of lower density than the core, which is consistent with a Ti-MIL-125 shell on a SiO<sub>2</sub> core. The assignment of the shell to Ti-MIL-125 is further corroborated by the energy dispersive X-ray (EDX) mapping in Figures 3.9b-e: Figure 3.9b clearly shows the Si signal to be located only in the core region. In stark contrast, Ti (Figure 3.9c) and C (Figure 3.9d) signals are located in the homogeneous shell structure with thickness of ~110 nm. This is fully consistent with a Ti-MIL-125 shell. O signal (Figure 3.9e) is correspondingly present in both the SiO<sub>2</sub> core and Ti-MIL-125-like shell. Raman measurements of such SiO<sub>2</sub> nano-powders after ALD coating exhibit a Raman signal consistent with Ti-MIL-125-like coatings, akin to the discussion above. Consequently, Figure 3.9 confirms conformal coating of SiO<sub>2</sub> nanoparticles by Ti-MIL-125-like shells via our ALD process.

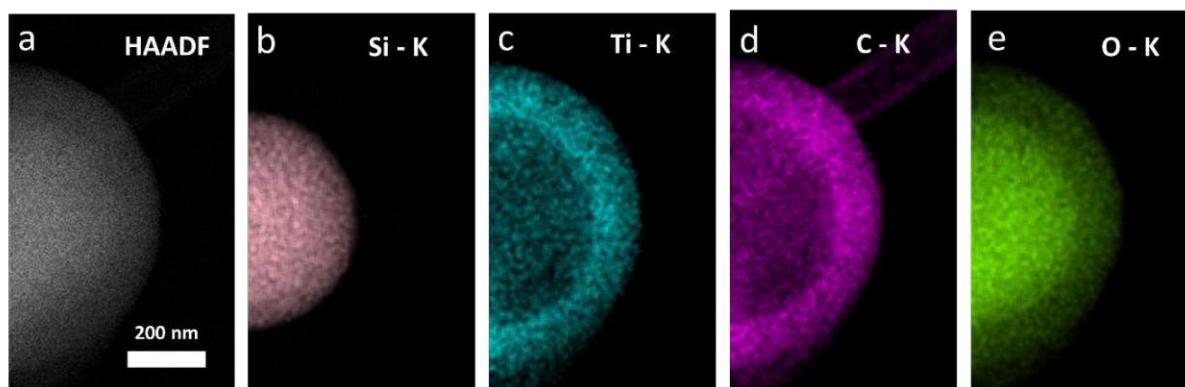


**Figure 3. 9:** (a) HAADF STEM image showing a  $\text{SiO}_2$  nanoparticle coated with  $\sim 110$  nm of Ti-MIL125-like material by ALD in a core-shell structure. (b) to (e) corresponding EDX maps: (b) Si-K-edge; (c) Ti-K-edge; (d) C-K-edge; (e) O-K-edge. In (d) one can also see a strand from the lacey carbon support on which the core-shell structure is immobilized for STEM imaging.

Successful coating of the  $\text{SiO}_2$  nanoparticle powder with the Ti-MIL-125-like MOF films also opens these ALD MOF materials to study with powder-based techniques that are usually not possible with flat wafers. In particular physisorption/Brunauer-Emmett-Teller (BET) specific surface measurements become possible via the core-shell Ti-MIL-125-like MOF/ $\text{SiO}_2$  nanoparticle powders. We note however that for our  $\sim 100$  nm ALD MOF films BET specific surface area measurements are still very challenging, as also recently explicitly highlighted in the literature on ALD MOFs.<sup>175</sup> Correspondingly, our  $\text{N}_2$  physisorption measurements at 77 K and their BET analysis measurements turned out to be a quite challenging instrumentally, mostly since the total amount of material (ALD MOF-like coated  $\text{SiO}_2$  nanoparticles) obtainable at this proof-of-point was only some tens of milligrams, of which the coating also only comprised an estimated  $\sim 70\%$  volume fraction. For this reason, we also do not initially safely assign absolute specific surface area values (due to possible systematic error from low amount of material) but instead first discuss the relative increase in specific surface area upon ALD MOF coating. The obtained adsorption-desorption isotherms from physisorption measurements at 77 K are shown in Figure 3.10 and analyzed in Table 3.2. Notably we measure for bare  $\text{SiO}_2$  nanoparticles signs of mesoporosity and a specific surface area of  $107.8 \text{ m}^2/\text{g}$ , compared to an estimated specific surface area of approximately  $5.1 \text{ m}^2/\text{g}$  for a simple model for a non-porous  $\sim 500$  nm diameter  $\text{SiO}_2$  nanoparticle, indicating that the sol-gel  $\text{SiO}_2$  nanoparticle substrates also have some intrinsic porosity (Table 3.2). Upon Ti-MIL-125-like

MOF shell ALD we however measure development of both micro- and mesoporosity and also a marked increase in specific surface area by a factor of 2.7 to 288.9 m<sup>2</sup>/g. Notably, this is a clear relative increase, while one would expect a decrease from the diameter increase of a non-porous Ti-MIL-125-like coated SiO<sub>2</sub> nanoparticle (Table 3.2). Therefore, our BET measurements strongly indicate introduction of additional micro- and mesoporosity and corresponding increase in specific surface area via ALD of our Ti-MIL-125-like MOF on SiO<sub>2</sub> nanoparticles to an absolute value of 288.9 m<sup>2</sup>/g. Prior reported specific surface areas of reference solvothermally synthesized Ti-MIL-125 micropowders were ~1400 m<sup>2</sup>/g.<sup>49</sup> Thus our specific surface area of the Ti-MIL-125-like MOF coated nanoparticles falls surprisingly well within a factor of ~5 of the optimized, highly crystalline solvothermal Ti-MIL-125 micropowder reference. In line with the above observed lower degree of crystallinity of the ALD Ti-MIL-125-like MOF we also ascribe this significant but still lower absolute specific surface area to the lower degree of crystallization in the ALD process compared to optimized hydrothermal synthesis.

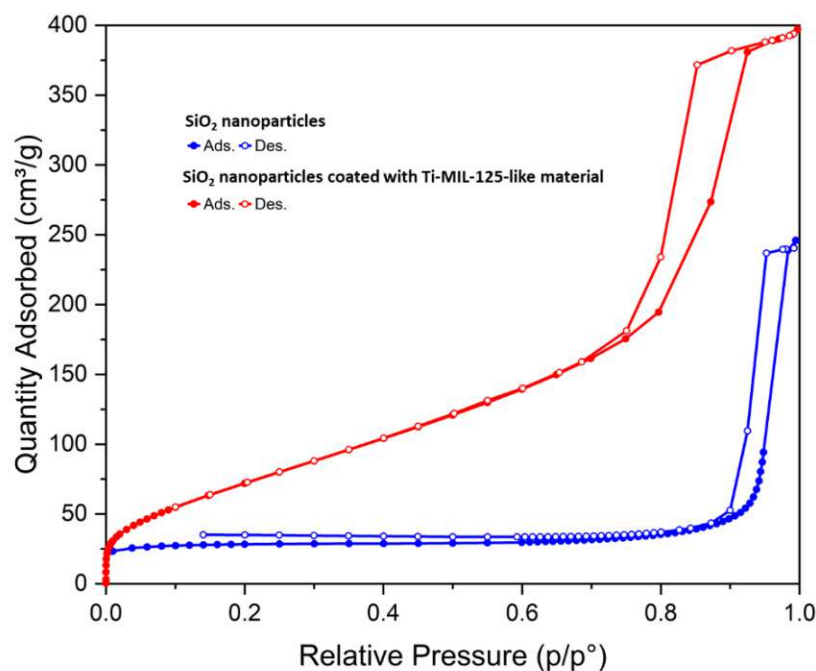


**Figure 3. 10:** Adsorption (ads.) and desorption (des.) isotherms measured by N<sub>2</sub> physisorption at 77 K, the blue graph shows the uncoated SiO<sub>2</sub> nanoparticles while the red curve shows

particles coated with 1000 pulse cycles of ALD Ti-MIL-125-like MOF. The data indicates that bare SiO<sub>2</sub> nanoparticles have mesoporosity. In contrast, upon coating with the ALD MOF clear signs of microporosity and increased mesoporosity are observed. Extracted BET specific surface areas are presented in Table 3.2.

	Estimated radius (nm)	Estimated Volume (m <sup>3</sup> )	Estimated mass (g)	Estimated Surface (m <sup>2</sup> )	Estimated specific surface (m <sup>2</sup> /g)	BET surface area (m <sup>2</sup> /g)
<b>bare SiO<sub>2</sub> nanoparticles</b>	270	8.2E-20	1.8E-13	9.2E-13	5.1E+00	1.1E+02
<b>coated SiO<sub>2</sub> nanoparticles</b>	402	2.7E-19	5.0E-13	2.0E-12	4.1E+00	2.9E+02

**Table 3. 2:** Calculations used for estimation of the expected specific surface of the bare non-porous SiO<sub>2</sub> nanoparticle incl. Ti-MIL-125-like coating assuming non-porosity, as well as measured corresponding BET-results.

### 3.3.3 Photocatalytic HER measurements.

To finally also test the functionality of the produced ALD Ti-MIL-125-like material, we employ our ALD Ti-MIL-125-like coated SiO<sub>2</sub> nanoparticles as photocatalysts in suspension-type photocatalytic HER for water splitting. In particular, we compare our ALD Ti-MIL-125-like material on SiO<sub>2</sub> nanoparticles with reference solvothermally produced Ti-MIL-125 micrometer-scale crystalline particles,<sup>49,131</sup> as well as with ALD TiO<sub>2</sub> coatings on SiO<sub>2</sub> nanoparticles<sup>176</sup> and standard commercial anatase TiO<sub>2</sub> nanoparticles (99.7 %, 25 nm, Sigma Aldrich).<sup>177</sup> The comparison with TiO<sub>2</sub> allows a contrast to the to date benchmark photocatalytic HER catalyst used in a majority of the literature.<sup>177</sup> In line with all prior literature,<sup>49,131</sup> we use for all measurements 1% Pt as HER co-catalyst, a 1:1 mixture of water:methanol (whereby the latter acts as sacrificial hole scavenger) as suspension medium and UV-light (280 - 400 nm) as excitation source in a custom-built modular photocatalysis reactor. Quantification of the formed amount of H<sub>2</sub> gas was performed by use of gas chromatography.

Table 3.3 shows the obtained HER evolution performance from the various samples. We first note that bare SiO<sub>2</sub> nanoparticles as a baseline reference do not show any photocatalytic HER activity i.e. bare SiO<sub>2</sub> are inactive towards HER and thus only act as an inert support. When SiO<sub>2</sub> nanoparticles are coated with our ALD Ti-MIL-125-like material we obtain a photocatalytic HER evolution of ~28 μmol/(h·g) H<sub>2</sub>. As a direct comparison from the same ALD system, we then measure ALD TiO<sub>2</sub> coatings that were similarly deposited at ~260 °C using TiCl<sub>4</sub> and water in the same ALD system on SiO<sub>2</sub> nanoparticles. As seen in the TEM characterization in Figure 8, this results in homogeneous nanocrystalline TiO<sub>2</sub> coatings on the SiO<sub>2</sub> nanoparticles with similar thickness to the ALD Ti-MIL-125-like material. These ALD TiO<sub>2</sub> coatings on SiO<sub>2</sub> nanoparticles yield a H<sub>2</sub> evolution performance of ~1900 μmol/(h·g) H<sub>2</sub> under otherwise same HER conditions. At first glance a performance ratio of only ~0.015 for our ALD Ti-MIL-125-like material vs. ALD TiO<sub>2</sub> may appear disappointing. To contextualize these values, in a next step we however measure the HER performance ratio of benchmark solvothermal Ti-MIL-125 micrometer-scale crystalline particles (~2000 μmol/(h·g) H<sub>2</sub>) vs. benchmark commercial anatase TiO<sub>2</sub> nanoparticles (~8000 μmol/(h·g) H<sub>2</sub>). This results in a HER performance ratio of benchmark solvothermal Ti-MIL-125 vs. benchmark anatase TiO<sub>2</sub> nanoparticles of ~0.25. The comparison to these highly optimized and highly crystalline benchmark systems shows that ALD coatings deposited at ~260 °C generally result in lower catalytic activity for both Ti-MIL-125 and TiO<sub>2</sub> systems. In turn, these results also imply that compared to the solvothermal benchmark standards, our ALD Ti-MIL-125-like coatings perform within one order of magnitude of relative performance versus the corresponding TiO<sub>2</sub> comparison material. This shows that ALD MOF coatings could not only allow highly conformal ultra-thin coating of nanoscale objects (as demonstrated above) but also offer a perspective for actual photocatalytic activity and application, which to date has not been demonstrated in the literature for ALD MOF materials. The overall lower performance ratio of ALD Ti-MIL-125-like materials/ALD TiO<sub>2</sub> (0.25) vs. benchmark solvothermal Ti-MIL-125/benchmark anatase TiO<sub>2</sub> nanoparticles (0.015) can be ascribed to the lower degree of crystallinity and porosity observed above in the ALD Ti-MIL-125-like material.

	[H <sub>2</sub> ] - μmol/(h·g)	ratio [H <sub>2</sub> ] from MOF/TiO <sub>2</sub>
Bare SiO <sub>2</sub> nanoparticles	0	
ALD Ti-MIL-125-like coating	28	0.015
ALD TiO <sub>2</sub> coating	1876	
solvothermal Ti-MIL-125 micropowder	1990	0.25
TiO <sub>2</sub> nanopowder (anatase)	8021	

**Table 3. 3:** Hydrogen evolution rates [H<sub>2</sub>] and their respective ratios of bare SiO<sub>2</sub> nanoparticles, ALD Ti-MIL-125-like coating on SiO<sub>2</sub> nanoparticles, ALD TiO<sub>2</sub> coating on SiO<sub>2</sub> nanoparticles, solvothermal Ti-MIL-125 micropowder and TiO<sub>2</sub> nanopowder (anatase) benchmark.

### 3.4 Conclusions

In this work we demonstrated the deposition of ultra-thin (~30 nm to 150 nm), highly conformal films of Ti-MIL-125-like material by ALD not only onto flat wafer substrates but also onto nanoscale objects, in particular forming unprecedented ultra-thin, homogeneous Ti-MIL-125-like shell coatings on SiO<sub>2</sub> nanoparticle cores. Complementary structural characterization indicates a comparatively low degree of crystallization in the ALD MOF films, which is why we term these as “Ti-MIL-125-like”, given their structural characteristics of Ti-MIL-125 observed in Raman spectroscopy but remaining XRD-amorphicity. We demonstrate that these ALD Ti-MIL-125-like materials show sizeable activity in photocatalytic hydrogen evolution from water splitting. Our work thereby extends ALD MOFs not only to production of ultra-thin and homogeneous ALD MOF coatings on nanoscaled, complex shaped substrates (as

demonstrated here for SiO<sub>2</sub> nanoparticle substrates) but also opens an application perspective of such ALD MOF films in photocatalysis.

### 3.5 Methods

#### 3.5.1 ALD.

All ALD depositions were conducted using a Picosun R200 Advanced ALD-reactor, which can accommodate up to 9 precursor sources (solid, liquid, gaseous). The system's base pressure, without pulsing, was maintained at 0.1 mbar. The synthesis procedure for Ti-MIL-125 involved a series of alternating pulse-purge cycles using two precursors: vapor from liquid TiCl<sub>4</sub> (with a purity of 99.7%) and solid TPA (with a purity of 99%). Liquid TiCl<sub>4</sub> was used at its room temperature vapor pressure (~13 mbar) for feeding. The solid TPA precursor was heated to 165 °C in its source, resulting in a vapor pressure of approximately 1 mbar. Pulsing valves and lines in our ALD system are heated to prevent the re-condensation of precursor vapor. In the case of TPA, the line and pulsing valve heating were set to 175 °C to avoid condensation. A flow of N<sub>2</sub> gas (purity of 5.0) was used both as a transport gas for the precursors to the substrate and as a purging gas between pulses (250 sccm). We employed a standard pulse-purge sequence of 20 s TPA - 40 s purge - 4 s TiCl<sub>4</sub> - 8 s purge. Film thicknesses were controlled by the number of pulse cycles. The substrates were heated inside the ALD chamber using a hot-wall heater. For depositions on Si wafers, a wafer holder (fitting 100-, 200- and 300-mm samples) provided by the manufacturer was used. A 100-mm wafer was used as platform for smaller, manually cut pieces of wafers. Powder coatings were performed using an Al<sub>2</sub>O<sub>3</sub> crucible that was filled with approximately 100 mg of SiO<sub>2</sub> nanoparticles, placed underneath the precursor distribution place and right next to the pumping line. Additionally, some powder coatings were directly performed on SiO<sub>2</sub> nanoparticles that were immobilized on lacey carbon TEM grids for comparison to the standard powder recipe. We note that generally the observed homogeneity of ALD MOF coatings is better for flat Si wafer substrates, while for SiO<sub>2</sub> nanoparticles variations in coating homogeneity are often observed, especially for higher powder loadings in the crucible, presumably due to flow differences through a deep powder bed. This is a challenge in line with prior reports on ALD coating of fine powders.<sup>163</sup>

Since the standard pulse-purge scheme was well above the saturation range no changes were applied on the ALD recipe for coating of wafer samples or powder samples.

### 3.5.2 Substrates.

Si-wafers were commercially sourced from Silicon Materials (polished, (100)-oriented, P-doped wafers with 2 nm native oxide, a thickness of 525  $\mu\text{m}$  and 100 mm diameter) and cleaved by hand to  $\sim 1 \times 1$  cm pieces for our experiments.  $\text{SiO}_2$  nanoparticles were synthesized using the sol-gel method following a published recipe.<sup>178,179</sup> The following substances were employed: tetraethylorthosilicate (TEOS) with a purity of 99.9%, absolute ethanol (EtOH) with a purity of 99.5%, concentrated ammonia and water. The procedure commenced by adding 4 mL of a saturated ammonium hydroxide solution to 50 mL of absolute EtOH in a flask. Subsequently, TEOS (0.28 mol/L) was introduced into the mixture. Within minutes, the mixture transformed into a white suspension, which was stirred for 120 min. Following a 24 h aging process, the sol underwent gelation. To obtain nanoparticles, the gel was subjected to drying at 100 °C for 2 h to eliminate water and organic compounds. Subsequently, the dried gel underwent calcination at 450 °C for 3 h, resulting in a powder that was subsequently ground.

### 3.5.3 Characterization.

SEM was performed on a FEI Quanta 250 Field-Emission-Gun-SEM, equipped with an Everhardt-Thornley secondary electron detector. The device was operated at an electron acceleration voltage of 10 kV at a working distance of about 5 mm. XPS was measured in a custom-designed XPS system (SPECS) using monochromatic Al- $K_\alpha$  (1486.6 eV) radiation and a hemispheric Phoibos WAL 150 photoelectron energy analyzer. Raman spectra were measured using a 488 nm laser source equipped on a WITech alpha 300 RSA+ confocal Raman spectrometer. XRD measurements were performed using a X'Pert MPDII diffractometer in Bragg-Brentano geometry (with application of an  $\Omega$ -offset to suppress overwhelmingly intense single-crystal Si-wafer substrate reflections), equipped with a Cu- $K_\alpha$  X-Ray source and

an X'Celerator semiconductor detector. The samples were mounted on the spinning holder with a rotation speed of four seconds per rotation. X-ray reflectivity (XRR) experiments were carried out within a scattering angle range of  $-0.5^\circ < 2\theta < 2.5^\circ$  at a Malvern PANalytical (B.V.) Empyrean diffractometer. The line focus of an Empyrean Cu LFF HR X-ray tube was used for the measurements. This metal-ceramic tube has a maximum power rating of 1.8 W and a focal spot of  $12 \text{ mm} \times 0.4 \text{ mm}$ . The exit window consists of beryllium with a thickness of  $300 \mu\text{m}$ . The tube was operated at 45 kV and 40 mA. A hybrid monochromator consisting of a parabolical shaped graded multilayer and a channel-cut Ge(220) crystal in one module was used to provide almost pure  $K\alpha_1$  radiation. The  $K\alpha_2$  radiation is reduced to below 0.1% of the original value. The parallel beam X-ray mirror module contains a parabolical shaped graded multilayer. It converts the divergent beam into a monochromatic  $K\alpha$  quasi-parallel beam. The  $K\beta$  radiation is reduced to below 0.5% of the original value. The beam divergency was reduced to  $1/32^\circ$  by placing a fixed vertical entrance slit and a 10 mm horizontal mask in front of the monochromator. On the second beam path a  $0.18^\circ$  vertical Soller was introduced together with a  $0.18^\circ$  receiving slit in front of a scintillation detector. The detector to sample distance for this instrument is fixed to 240 mm. The data was analysed using Refnx.<sup>180</sup> The density was calculated from the evaluated scattering length density using the chemical formula of Ti-MIL-125. The same device was also used for additional grazing incidence (GI) XRD-measurements with a parallel beam mirror instead of the alpha-hybrid monochromator, which yielded similar "XRD-amorphy" as the Bragg-Brentano XRD measurements above. TEM measurements and STEM-EDX-mapping were performed on a Tecnai F20 FEG-TEM, equipped with a X-FEG, a Gatan Rio16 CCD-camera, Gatan DigiSTEM II with HAADF detector for STEM imaging and an EDAX-AMETEK Apollo XLTW SDD EDX-detector. The operating voltage was kept at 200 kV for all measurements.  $\text{N}_2$  physisorption measurements were performed at 77 K with a Micromeritics 3Flex device. The specific surface area was calculated using the Brunauer-Emmet-Teller (BET) equation. Prior to the physisorption experiments, the samples were degassed in vacuum at a temperature of  $150^\circ\text{C}$  for a duration of 10 hours.

### 3.5.4 Photocatalytic HER tests.

HER experiments were done using a side-irradiation batch-type home-made reactor equipped with a water cooling circuit kept at 15 °C during the reaction.<sup>181,182</sup> For the experiments 10 mg of the photocatalyst materials was weighed into 2 ml of a 1:1 MeOH:H<sub>2</sub>O solution with methanol taking the role of the sacrificial agent.<sup>181</sup> 1% Pt (with respect to the catalyst mass) was photodeposited in situ as HER co-catalyst by adding a corresponding amount of hexachloroplatinic acid (H<sub>2</sub>PtCl<sub>6</sub>); in line with prior HER photocatalysis literature on Ti-MIL-125.<sup>49,131</sup> The reactor was closed and purged with argon through the septum to remove any dissolved oxygen. For illumination purposes, a 200 W super-pressure Hg lamp (with a wavelength range of 240-400 nm and an intensity of ~30 mWcm<sup>-2</sup>; Superlite SUV DC-P deep UV model from Lumatec) was utilized. The light was delivered via optical fiber light guide.<sup>49,131,181</sup> Before illumination, 200 µL of the reactor's gaseous phase was sampled using gas-tight Hamilton syringe and injected into the gas chromatography (GC) instrument (GC-2030, Shimadzu; Micropacked-ST Column, ShinCarbon; and barrier discharge ionization detector, BID) to confirm successful degassing and the absence of any undesired components in the head space. The light source was then turned on and the amount of photocatalytically evolved H<sub>2</sub> accumulated in the head space was analyzed by taking 200 µL injection volumes at different time intervals. The GC-derived amounts of H<sub>2</sub> evolved in ppm were converted to µmol considering the head space volume (via ideal gas equation). The activities were finally normalized per mass of the photoactive component, which in the case of the SiO<sub>2</sub>/MIL-125-like and SiO<sub>2</sub>/TiO<sub>2</sub> core-shell structures considered only the mass of the MIL-125-like or TiO<sub>2</sub>, respectively. Reference solvothermal Ti-MIL-125 powder was synthesized following published recipes.<sup>49,131</sup> Reference TiO<sub>2</sub> nanoparticles (anatase) were purchased from Sigma Aldrich (99.7 %, PCode 1002920065). Reference ALD TiO<sub>2</sub> coating on SiO<sub>2</sub> nanoparticles was done at ~260 °C using TiCl<sub>4</sub> and water in the same ALD system.

### 3.6 Acknowledgements

The authors acknowledge the use of facilities at the University Service Centre for Transmission Electron Microscopy (USTEM), Analytical Instrumentation Centre (AIC) and X-Ray Centre (XRC), TU Wien, Austria for parts of this work.

### 3.7 Author Contributions

Jakob Rath (IMC, TUW) , Dominik Eder (IMC, TUW) and Bernhard C. Bayer (IMC, TUW)planned the experiments. Bernhard C. Bayer conceived the idea. Jakob Rath developed the synthesis procedures and performed the majority of the materials characterizations in this work. Bernhard Fickl (IMC, TUW), Daniel Matulka (IMC, TUW), Hanspeter Kählig (Universität Wien), Clemens Mangler (Universität Wien) , Jani Kotakoski (Universität Wien), Alexey Cherevan (IMC, TUW), Shaghayegh Naghdi (IMC, TUW) , Sabine Schwarz (USTEM, TUW), Michael Stöger-Pollach (USTEM, TUW), Markus Sauer (AIC, TUW) and Annette Foelske (AIC, TUW) assisted with materials characterization. Njomza Isufaj (IMC, TUW) and Ariane Giesriegel (IMC, TUW) assisted with synthesis. Bernhard C. Bayer and Dominik Eder supervised the work. Jakob Rath and Bernhard C. Bayer wrote the manuscript with inputs from all authors.

# 4 Synthesis of Metal-Organic-Framework Nano-Laminates by ALD

## 4.1 Abstract

We demonstrate the deposition of ultrathin (40 nm to 200 nm thickness) nano-laminates consisting of alternating layers of Ti-MIL-125- and UiO-66-like metal-organic-framework (MOF) films by atomic layer deposition (ALD). We find that structurally our ALD MOF laminates show characteristic MOF-features in Raman spectroscopy, while they appear amorphous in X-ray diffractometry (XRD) (i.e. are “XRD-amorphous”) in the as-deposited state. Subsequent annealing steps enabled post-deposition crystallization of the films to a certain extent but at the expense of the controlled nano-laminate morphology. In general, we introduce a scalable and reproducible route towards synthesis and integration of MOF-like nanolaminates.

## 4.2 Introduction

A metal-organic-framework (MOF) is a type of material composed of metal ions or clusters (nodes) and organic molecules (linkers) which are linked together to form a three-dimensional network.<sup>61,183,184</sup> MOFs have attracted considerable attention in recent years due to their unique combination of high surface area, tunable porosity, and chemical stability, which makes them attractive for a wide range of applications, such as biomedical applications<sup>185,186</sup>, gas storage and separation<sup>47,48</sup>, catalysis<sup>49,76,187,188</sup> or as ultra-low-k dielectrics in semiconductor industries.<sup>189–192</sup>

While classical, usually solvothermal approaches to the synthesis of MOFs result in highly ordered nanoparticles, in recent years, new synthetic techniques and approaches have allowed the formation of amorphous Metal-Organic Frameworks that lack long-range crystalline order, but still retain their outstanding properties.<sup>95,96,193,194</sup> Unlike crystalline

MOFs, which have a well-defined and periodic structure, amorphous MOFs have a disordered and random arrangement of their constituent molecules.

Today amorphous MOFs can be synthesized by a variety of methods, including sol-gel processes<sup>195,196</sup>, rapid precipitation<sup>197</sup>, melt quenching<sup>198,199</sup> or vapor-based deposition techniques.<sup>95,200</sup> Similar to their crystalline analogues they have potential applications in sensing, gas storage, catalysis, and drug delivery due to their high surface area, tunable pore size, and active metal centers, while their amorphous nature allows for greater flexibility in their design and synthesis.<sup>95</sup>

A well-known challenge in working with amorphous MOFs is the aforementioned lack of long-range order, which makes it difficult to determine their exact structure and properties. However, recent advances in characterization techniques and understanding of these materials, have helped to elucidate their structures and properties and to identify an adequate range of methods for a sufficient description.<sup>95,96,193,201</sup>

A specific area of research that has not yet attracted too much attention is the use of MOFs as the basis for nanolaminates, which are thin films composed of alternating layers of different materials (Figure 4.1a).<sup>202-205</sup> By carefully designing the composition and structure of these layers, researchers should be able to create MOF-based nanolaminates with enhanced properties, such as improved stability, optimized band gaps or dielectric properties<sup>206</sup> and improved gas adsorption or separation properties.<sup>100</sup> Gradient materials can also be produced using this technique.<sup>207,208</sup>

Atomic Layer Deposition (ALD) is a highly precise thin-film growth technique that operates on the nanometer scale, hence enabling the creation of nano-laminates with individual layer thicknesses as thin as single molecular layers. Typically, films produced by ALD exhibit exceptional uniformity and quality. In this work we argue that ALD can be suitable for the synthesis of Metal-Organic Framework (MOF) laminates, a category of materials that would be difficult to produce using most alternative synthesis methods. These challenges often stem from issues of uniformity, scalability, and interface quality, which ALD effectively overcomes.

However, as noted above, a limitation of this vapor based method is the relatively low degree of crystallinity observed in the resulting materials.<sup>200</sup>

Recently, there has been a significant increase in the number of researchers focusing on all-gas-phase methodologies for synthesizing Metal-Organic Framework (MOF) thin films. This growth has resulted in the development of successful routes towards production of specific MOFs using Chemical Vapor Deposition (CVD) and Atomic Layer Deposition (ALD) processes. One of the notable MOFs is the UiO-66 framework (Figure 4.1c), which consists of  $Zr_6O_4(OH)_4$  nodes coordinated with terephthalate linkers to create a highly porous, thermally stable, and chemically robust network.<sup>46</sup>

Our prior research (Chapter 3) has involved developing a methodology for synthesizing and integrating Ti-MIL-125 (Fig. 4.1b), another MOF constructed from  $Ti_8O_8(OH)_4$  clusters connected by terephthalate linkers. Ti-MIL-125 has impressive surface area and potential for use in heterogeneous catalysis, such as photocatalytic water splitting.<sup>49,50,209</sup>

Since these two networks have both similar building blocks and a set of outstanding material properties, we decided to combine them in a laminate to develop a new nanostructured material with unique properties. This combination should also enable the manufacturing of materials with adjustable properties, such as, e.g., perfectly engineered and optimized dielectric constants for use as low-k dielectrics in the semiconductor industry.

Low-k dielectrics are a class of materials used in semiconductor manufacturing to insulate and separate different layers of integrated circuits (ICs) while minimizing the capacitance between them. They play a critical role in advancing the performance and efficiency of semiconductor devices. The dielectric constant, represented as "k" measures a material's ability to store electrical energy. Low-k materials have lower dielectric constants, which reduces the capacitance between neighboring conductive elements in semiconductor devices. This reduction in capacitance enhances the device's speed and lowers power consumption.<sup>190,195,210,211</sup>

As semiconductor devices become smaller and more complex, it is increasingly important to reduce interconnect delays and power consumption. To address the issues of signal delays and increased power consumption caused by the relatively high dielectric constant ( $\kappa \approx 4$ ) of traditional silicon dioxide ( $\text{SiO}_2$ ) dielectrics, low-k dielectrics ( $\kappa < 4$ ) were developed.<sup>212,213</sup> The semiconductor industry's pursuit of miniaturization, as described by Moore's Law, requires the constant development of advanced materials. Low-k dielectrics have become a crucial factor in scaling down feature sizes while maintaining or enhancing performance.

There are several types of low-k dielectrics, the most important are organic low-k materials<sup>214</sup>, inorganic low-k materials<sup>215</sup>, and hybrid low-k materials.<sup>216,217</sup> Organic low-k dielectrics, which are often based on carbon-based compounds, offer low dielectric constants. However, they can be less thermally stable than their inorganic counterparts. Inorganic low-k dielectrics typically consist of materials such as silicon-based compounds. Hybrid low-k dielectrics combine both organic and inorganic components to balance performance and stability. Some low-k materials are intentionally engineered to have pores or voids,<sup>210,218</sup> which reduce the dielectric constant by lowering the effective permittivity. Although challenging to manufacture, porous low-k materials provide significant performance benefits. Recently the material subclass of MOFs has gained attention as a potential source for porous low-k hybrid materials.<sup>189,214,218</sup>

Implementing low-k dielectrics in semiconductor processes presents integration challenges. Low-k materials may be more sensitive to plasma etching, chemical mechanical planarization (CMP), and thermal processing.<sup>218</sup> Specialized deposition techniques, such as plasma-enhanced chemical vapor deposition (PECVD) and atomic layer deposition (ALD), are often used for precise control and generally offer great scalability.

Since both Zr- UiO-66 and Ti-MIL-125 are also interesting materials in their own right for (photo-)catalysis, such nanolaminates may also enable new catalytic concept such as charge separation across interfaces (charge funneling).

Our work here lays the basis for such future electronic or catalytic application exploration for such MOF nanolaminates via their fabrication for the first time in the literature.

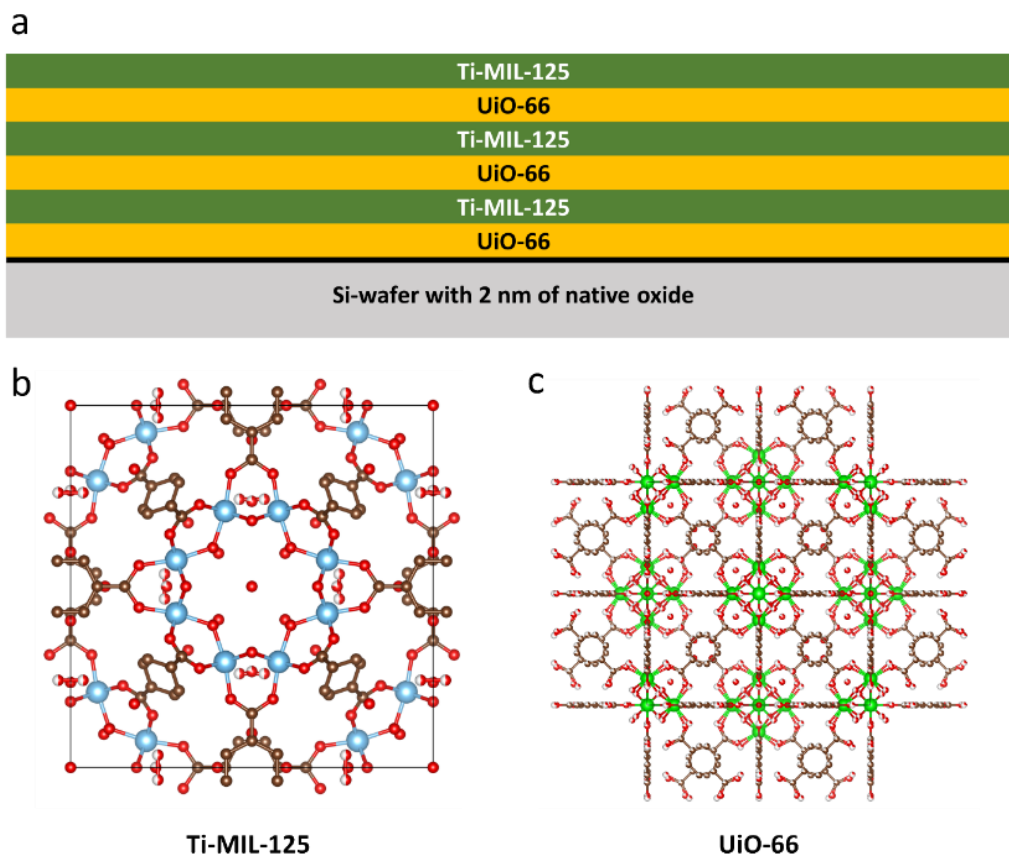


**Figure 4. 1:** a - Graphical representation of a nano-laminate consisting of three bilayers of the two MOF-type materials UiO-66 (orange) and Ti-MIL-125 (green) as synthesized by use of atomic layer deposition on a (100)-oriented Si-wafer (grey) with approximately two nm of native SiO<sub>2</sub> (black); b – Atomic sketch of Ti-MIL-125 structure in (100) orientation – blue: Ti, red: O, brown: C; c - Atomic sketch of UiO-66 structure in (100) orientation – green: Zr, red: O, brown: C; The sketches are based on ICDS structure files provided by Dan-Hardi et al.<sup>158</sup> and Sigurd Øien<sup>219</sup> and were created by use of the open-source software VESTA 3 for three-dimensional visualization of crystal, volumetric and morphology data.

### 4.3 Experimental

All Atomic Layer Deposition (ALD) processes were carried out in a Picosun R200 Advanced ALD-reactor, which can accommodate up to nine precursor sources, including solid, liquid, and gaseous precursors. The system was initially evacuated to a base pressure of 0.1 mbar

without precursor pulsing. In the synthesis of Ti-MIL-125, a series of alternating pulse-purge-cycles were employed using two specific precursors: the vapor from liquid  $\text{TiCl}_4$  (99.7 % purity) and solid TPA (99 % purity). The vapor pressure of liquid  $\text{TiCl}_4$  at room temperature is approximately 13 mbar and was used for  $\text{TiCl}_4$  feeding.<sup>220</sup> In contrast, TPA feeding required heating the solid precursor material in its source to 165 °C, resulting in a vapor pressure of approximately 1 mbar.<sup>46</sup> It is important to note that we implemented heating for the pulsing valves and lines in our ALD system to prevent the re-condensation of precursor vapor within the lines and valves. For TPA, the line and pulsing valve heating were set to 175 °C to prevent condensation. To enhance the structural order of the resulting films, a process with additional pulses of AcOH as a modulation agent was adopted. This enabled re-arrangement of the formed bonds, resulting in higher crystallinity and thermodynamic stability. This route was used for the majority of experiments illustrated in this work. Any data on unmodulated processes is specifically marked as such.

To synthesize UiO-66, a similar route was followed, but with the use of  $\text{ZrCl}_4$  instead of  $\text{TiCl}_4$ , as the source for the metal nodes. To achieve a vapor pressure of  $\sim 1$  mbar, the  $\text{ZrCl}_4$  source bottle was heated to 220 °C,<sup>46</sup> while the corresponding precursor lines were heated to 230 °C in order to prevent condensation. The pulse-purge procedure was the same as described for Ti-MIL-125-type material. In order to obtain films with a higher degree of crystallinity, pulses of AcOH were applied as a modulation agent.

A flow of high-purity  $\text{N}_2$  gas (5.0) was used as a transport gas to deliver the precursors to the substrate and as a purging gas between pulses at a rate of 250 standard cubic centimeters per minute (sccm). The standard pulse-purge sequence consisted of 4 seconds of  $\text{TiCl}_4$  (or  $\text{ZrCl}_4$  respectively), followed by an 8-second purging step, then 20 seconds of TPA exposure, and finally another 40-second purging step. To enhance the degree of crystallinity, we applied additional 1-second pulses of acetic acid (followed by 1 second of purging) as a modulation agent since the first results indicated a relatively low degree of structural organization. This deposition sequence was based on insights from existing literature data and previous studies

to ensure that we remained well above the saturation range.<sup>46</sup> The film thicknesses were set by varying the number of pulse cycles.

The substrates were heated in the ALD chamber using a hot-wall heater arrangement. Previous studies by Lausund et al. on UiO-66 and our own experiments with the Ti-MIL-125 system informed our approach, and all reactions were conducted at 265°C.<sup>46</sup>

The study began by developing an Atomic Layer Deposition (ALD) process for depositing UiO-66 and Ti-MIL-125 MOF-type materials on flat Si wafer substrates, as shown in Figures 4.2 and 4.4. ALD is well-established on flat substrates due to the easier control of precursor flow patterns. In contrast, applying ALD on nanoscopic powder substrates, such as ~ 500 nm SiO<sub>2</sub> nanoparticles (Figure 4.3), can be more challenging due to the complex flow dynamics involved. Coatings on Si wafers are limited by their accessibility to certain characterization methods that require powders, such as some sorption experiments or experiments on catalytic activity.

Several experiments were conducted to enhance the crystallinity through post-deposition treatment. The solvents used in the autoclavation steps included MeOH, AcOH, DMF, formaldehyde, acetone, formic acid, propanol, propanal, and benzoic acid. The last one enabled us to fabricate a crystalline material. However, none of the experiments resulted in the synthesis of a fully crystalline and uniform film.

The laminates were characterized using various methods to gain a comprehensive understanding of the new materials. XRD and Raman were used to observe the structural integrity of the network, while STEM-EDX, XPS, and ToF-SIMS were utilized to visualize the uniformity of the entire laminate, including the individual layers on a nanometer scale.

#### 4.4 Results and Discussion:

Figure 3.2a presents photographic evidence of Si wafer pieces before (left) and after ALD processing (right). The optical change in the substrate's color after deposition of two bilayers of MOF-type materials (right) clearly indicates homogeneous film deposition on a centimeter scale. Figure 4.2b, an accompanying scanning electron microscopy (SEM) image, suggests an overall homogeneous, flat morphology on a nanometer scale, with only a few slightly

protruding features of up to 100 nm width. During the aging process of the samples, a nanostructure develops on the surface. This phenomenon has been previously reported in the literature and is further described in Figure 4.4.<sup>46</sup>

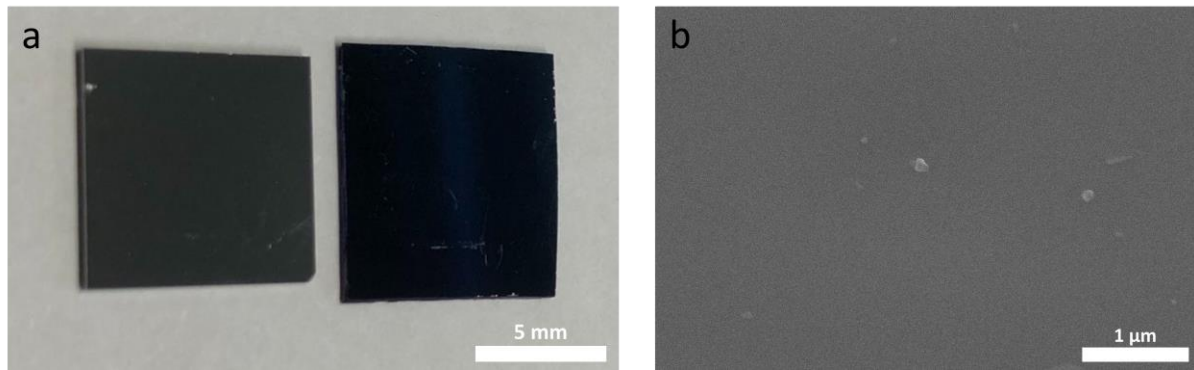


**Figure 4. 2:** *a – The left side of the photo shows a bare (100) Si-wafer, while the right side shows another piece of wafer coated with two bilayers of Ti-MIL-125 and UiO-66 type material using ALD. The uniform change in color demonstrates the homogeneity of the process on a centimeter scale. b – The corresponding SEM-image of the coated wafer indicates high quality and uniformity on a nanometer scale, with a few slightly protruding features measuring less than 100 nm.*

All elements present in the theoretical MOF-materials were confirmed using wavelength dispersive XRF and SEM-EDX (Figure 4.3). The nanospheres are visibly coated in the SEM image, and additional EDX-point spectra allow for visualization of all relevant transitions (Ti-K, Zr-L, Si-K, O-K, and C-K). The C-K peak has a super-elevated intensity due to the carbon tape (black areas) used as a support.

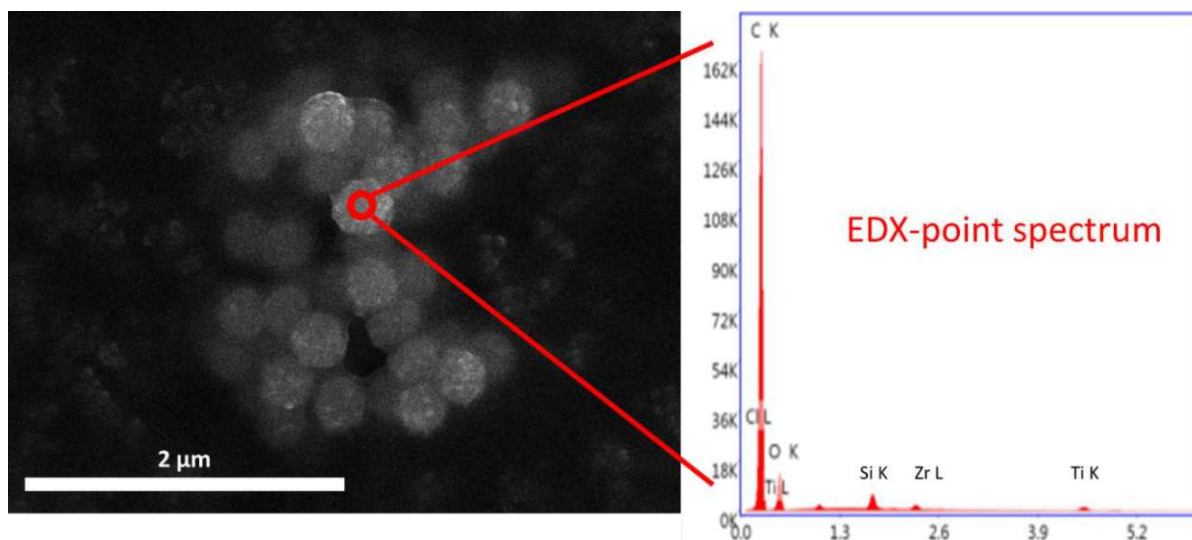


**Figure 4. 3:** A scanning electron microscope (SEM) image was taken of silica nanoparticles that were coated with two bilayers of the MOF-type materials UiO-66 and Ti-MIL-125. The powder coating system used  $\text{Al}_2\text{O}_3$ -crucibles and a Picosun R200 Advanced ALD reactor. The total thickness of the laminate is approximately 150 nm. The EDX-spectrum on the right indicates the presence of Ti, Zr, C, and O, which are all elements present in the desired MOFs. The image also clearly shows the time-dependent formation of protruding features on the nm scale, which is described in more detail in the following figure.

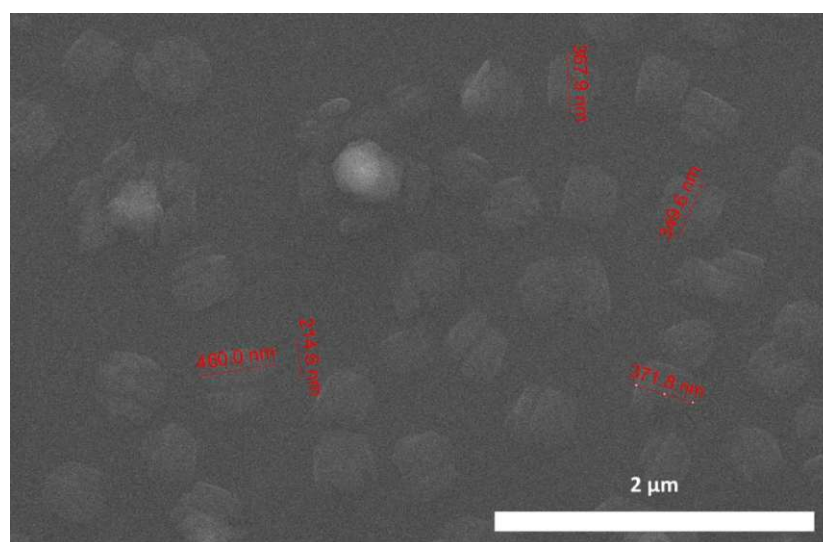


**Figure 4. 4:** A scanning electron microscope (SEM) image is presented, showing the surface of a wafer coated with two bilayers of UiO-66 and Ti-MIL-125, two MOF-type materials. The coating was applied using a Picosun R200 Advanced ALD reactor, resulting in a laminate with

*a total thickness of approximately 150 nm. The image was taken four months after synthesis. The monitored features exhibit time-dependent growth, as previously reported in publications on the synthesis of ALD-MOFs.<sup>46</sup> These structures have similar dimensions and geometries to solvothermal MOFs. Immediately after synthesis, the surfaces appear smooth and uniform, as shown in Figure 4.2b.*

To analyze the structural aspects, we employed Raman spectroscopy. Figure 4.5 illustrates the obtained data, while a more detailed view is provided in Figure 4.6. The Raman signals from the ALD MOF-like films deposited at 265°C substrate temperature suggest the presence of UiO-66 and Ti-MIL-125-like structures with low crystallization and a relatively higher amount of unreacted linker. To improve structural clarity, we utilized a deposition process with additional pulses of acetic acid as a modulation agent.<sup>46</sup> This resulted in clear improvements in the Raman fingerprints while maintaining the XRD-diffractograms unchanged. It is worth noting that additional post-deposition treatment, such as autoclavation in benzoic acid, can lead to the leaching of excessive linker molecules. These can be removed either in a subsequent DMF-washing step or by adding a small fraction of DMF during the annealing step.<sup>221</sup> This resulted in clear improvements in the Raman fingerprints while maintaining the XRD-diffractograms unchanged. It is worth noting that additional post-deposition treatment, such as autoclavation in benzoic acid, can lead to the

leaching of excessive linker molecules. These can be removed either in a subsequent DMF-washing step or by adding a small fraction of DMF during the annealing step.

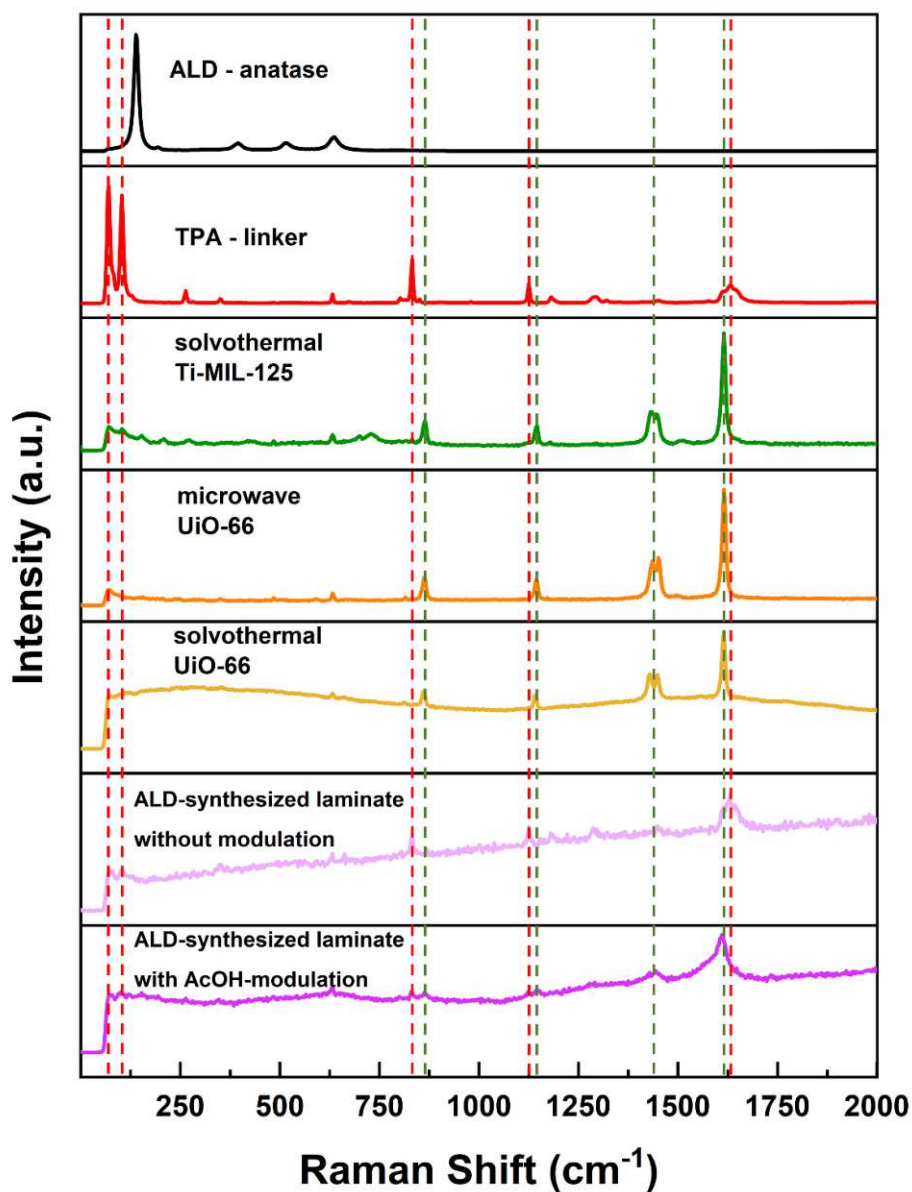


**Figure 4. 5:** The Raman spectra of various sample and reference substances are presented in the following order from top to bottom: – ALD-synthesized  $\text{TiO}_2$ -anatase deposited at 265 °C (black); – terephthalic acid (TPA = benzene dicarboxylic acid BDC, red); – Ti-MIL-125 synthesized by a standard solvothermal procedure (green); – UiO-66 synthesized by a microwave assisted approach (orange); – UiO-66 synthesized by a standard solvothermal procedure (yellow); – a laminate consisting of two bilayers of Ti-MIL-125- and UiO-66- type materials synthesized at 265 °C by use of ALD with no additional modulation (pink); – a

*laminate consisting of two bilayers of Ti-MIL-125- and UiO-66- type materials synthesized at 265 °C by use of ALD with additional pulses of acetic acid as a modulation agent (purple)*

*The spectra show that both laminates have features similar to UiO-66 and Ti-MIL-125 (green drop lines). The spectrum of the unmodulated sample displays peaks that correspond to the uncoordinated linker. However, upon addition of a modulation agent (AcOH), the spectrum exhibits all features of the solvothermal synthesized MOFs. It is worth noting that the relatively broader peaks suggest a lower level of crystallinity of the ALD-materials. For a more detailed view, refer to Figure 4.6. The Raman spectra of UiO-66 suggest that different synthetic approaches may lead to varying results and affect background or peak shapes due to residual solvent or linker molecules. The higher background in the ALD samples may be due to excessive linker molecules dissolved in the matrix. The first spectrum indicates that Titania was not formed during the process.*

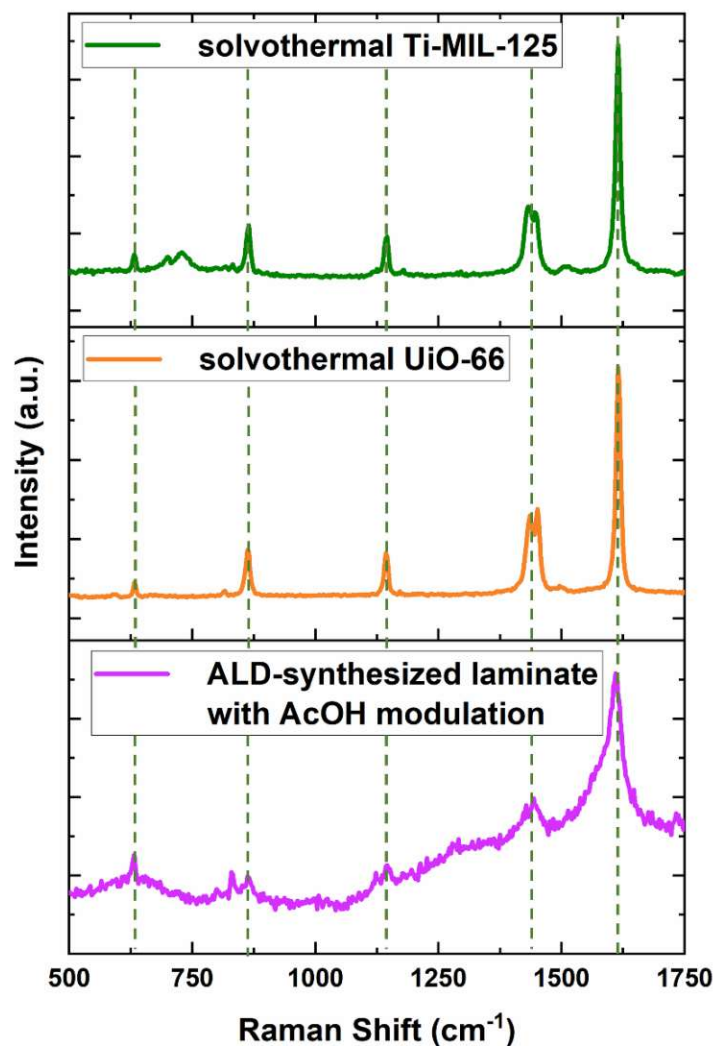


**Figure 4. 6:** The Raman detail-spectra of solvothermal Ti-MIL-125 (green) and UiO-66 (orange) as well as ALD-synthesized Ti-MIL-125- and UiO-66-like nano-laminate show similar features. The relatively broader peak in the vapor-based material indicates a lower level of crystallinity, as also implied by XRD. The higher background may be a consequence of excessive linker molecules present in the matrix.

While the laminates deposited without any modulation agents show Raman spectra that strongly correlate with terephthalic acid (peaks at  $70\text{ cm}^{-1}$ ,  $103\text{ cm}^{-1}$ ,  $832\text{ cm}^{-1}$ ,  $1125\text{ cm}^{-1}$ ,  $1632\text{ cm}^{-1}$ , red drop lines),<sup>222</sup> additional pulses of acetic acid lead to the formation of a material, that exhibits features which are in close correlation with UiO-66 and Ti-MIL-125 (peaks at  $865\text{ cm}^{-1}$ ,  $1143\text{ cm}^{-1}$ ,  $1438\text{ cm}^{-1}$ ,  $1615\text{ cm}^{-1}$ , green drop-lines)<sup>223</sup> while the linker-induced signals vanish almost completely. The presence of unreacted linker molecules is

indicated by the relatively high background observed in measurements obtained on both modulated and unmodulated ALD-synthesized samples. Similarly, an increase in background intensity can be observed in the case of solvothermal-synthesized UiO-66. It is important to note that microwave-synthesized UiO-66 does not exhibit any significant fluorescence background under the same measurement conditions, despite both materials appearing highly crystalline in powder XRD measurements. The presence of fluorescent molecules, such as solvents or excessive linkers, dissolved or distributed within the matrix, is a major reason for an excessive background in Raman.

The post-deposition treatment involved autoclavation with approximately 100 mg of benzoic acid at 170°C. This process improved the crystallization of the films, presumably by removing excess linker molecules (Figures 4.7 to 4.9). However, this treatment resulted in a significant reduction in the unity and uniformity of the laminates, which restructured from a closed film into discrete nanoparticles (Figure 4.8). The corresponding XRD data and optical microscope images that confirm these findings are displayed below. We tested several solvents and

combinations of solvents for the autoclavation of our MOF-type laminates, and we found that the crystallinity increased noticeably only when benzoic acid was used.

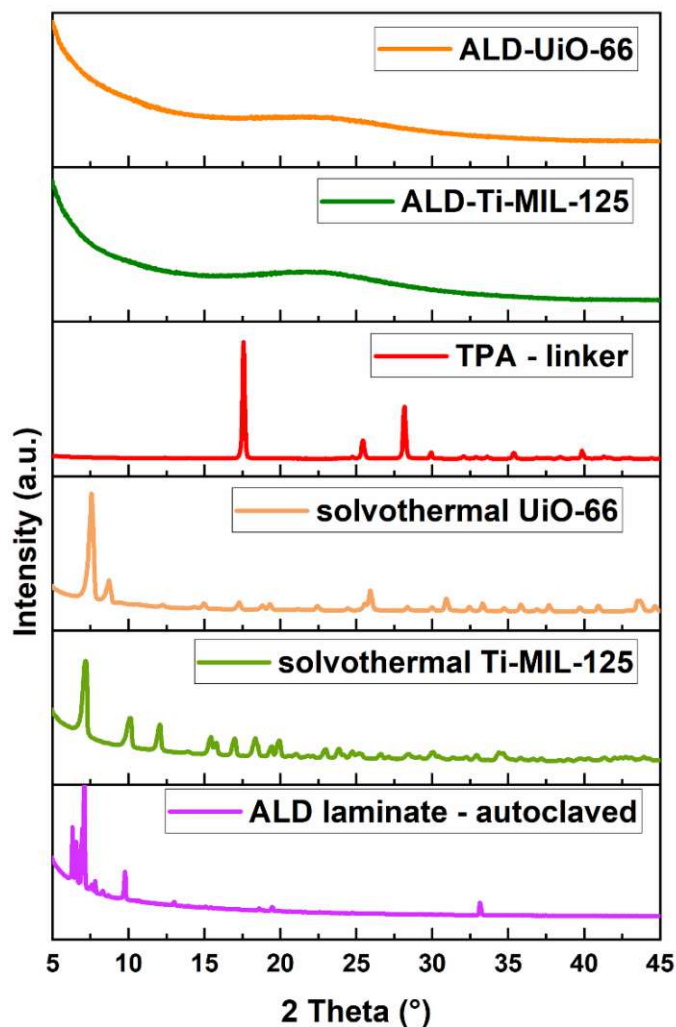


**Figure 4. 7:** The provided Powder-XRD data displays various samples and reference materials. From top to bottom, the samples include ALD-synthesized MOF-type material Ti-MIL-125, ALD-synthesized MOF-type material UiO-66, terephthalic acid (TPA) – linker, solvothermal UiO-66, solvothermal Ti-MIL-125, and an ALD synthesized laminate autoclaved using benzoic acid at 160 °C for 24 h. While the solvothermal MOFs exhibit clear reflexes that correlate to a highly crystalline 3-dimensional network, all ALD synthesized samples lack this sort of long-range order. Post-deposition treatment of the MOF-laminates results in partial crystallization,

leaving a material with a diffraction pattern that corresponds to both solvothermal MOFs to some extent (see Figures 4.8 and 4.9).

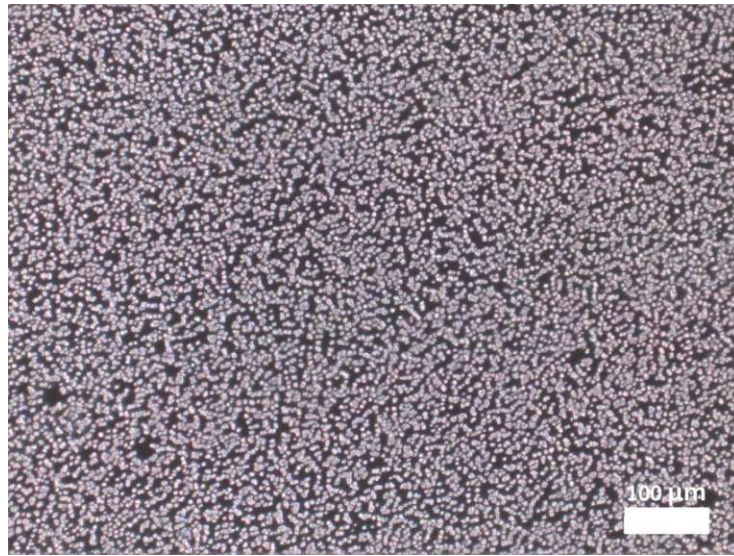


**Figure 4. 8:** This is a polarization-filtered DF-OM image of a MOF-type laminate after being annealed in benzoic acid for 24 hours in an autoclave. The uniformity of the film is significantly reduced, with islands of MOF-type material (bright areas) separated by uncoated holes (black - silicon surface).

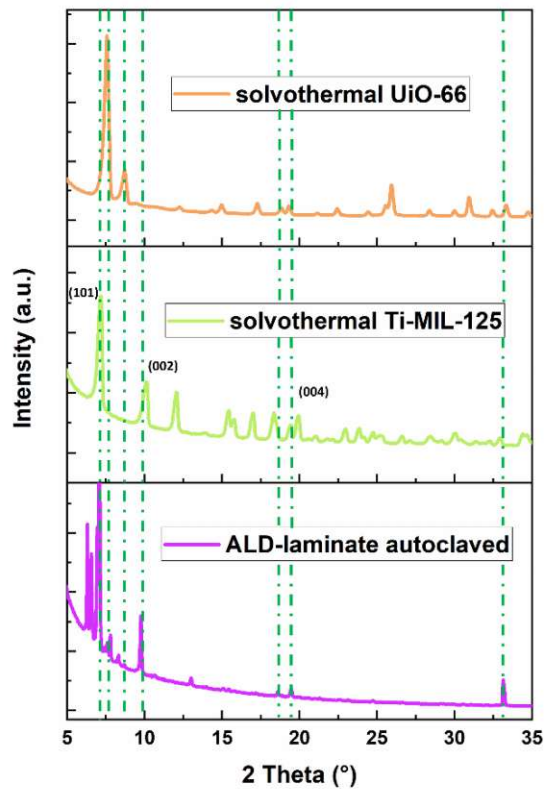


**Figure 4. 9:** Powder X-ray diffraction data were obtained for an MOF-type laminate synthesized using ALD and annealed in an autoclave with benzoic acid for 24 hours at 170°C. Comparison of the resulting pattern with solvothermal UiO-66 and Ti-MIL-125 revealed a range of equivalent features (indicated by green lines), while no signals correlated to TPA are present. However, the laminates' crystallinity is inferior to their solvent-based counterparts. This behavior may be due to the nature of the process, as epitaxial growth of material typically results in preferred orientations. One indication of preferred orientation is the presence of a certain family of reflexes, such as the (002)-family, and the absence of others, such as (211). Additionally, the OM images show that the films' closeness and uniformity are lost (see Figure 4.8).

Based on the morphological and structural findings of the as synthesized nanolaminates above (i.e. without post-deposition annealing), it is clear that our ALD process has produced homogeneous and flat films of materials that are closely related to UiO-66 and Ti-MIL-125,

although with limited structural order. These films are referred to as 'Ti-MIL-125- and UiO-66-like' films, similar to the term 'diamond-like-carbon'.<sup>224</sup>

To assess the uniformity and integrity of these synthesized nano-laminates, an ultra-thin lamella (< 200 nm) was extracted from the wafer surface using a focused ion beam (FIB). The resulting cross-section was then analyzed using a Tecnai F20 TEM, and elemental maps were recorded in HAADF using STEM-EDX. The resulting images are presented in Figure 4.10.

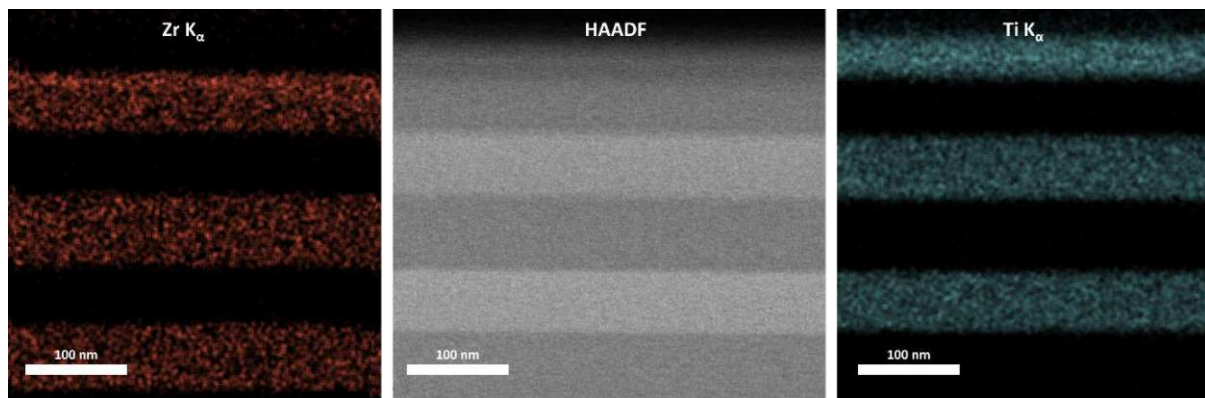


**Figure 4. 10:** STEM-EDX images were obtained on a FIB-cross-section of a Si-wafer coated with three bilayers of UiO-66 (Zr-K $\alpha$ , left, orange) and Ti-MIL-125 (Ti-K $\alpha$ , right, green) MOF-type materials. The materials were synthesized using atomic layer deposition with additional AcOH modulation. The images show the formation of several independent layers of MOF-type materials on the substrate. The Ti-MIL-125 type material on the top layer has a relatively lower thickness due to the deposition of a few nm thick Pt-layer on top of the material. This preserves the surface chemistry during etching with the focused ion beam.

The data obtained indicates the presence of highly uniform and dense layers of MOF-type materials that are well separated from each other. The images also do not show any signs of interface cavities or shrinkages that could reduce the stability of the material and limit its potential applications, particularly in semiconductor components.

To determine the chemical uniformity and integrity of the laminate, XPS depth profiling was performed on a film containing three bilayers of the ALD-synthesized frameworks. The

obtained profile is illustrated in Figure 4.11, which shows distinct regions of Ti- and Zr-rich materials with a clear separation between the single sheets. Although the signals for the two metals exhibit strong periodic variations, the signals for oxygen and carbon remain almost constant throughout the film and disappear as the silicon interface is approached at a sputter time of approximately 85 minutes.

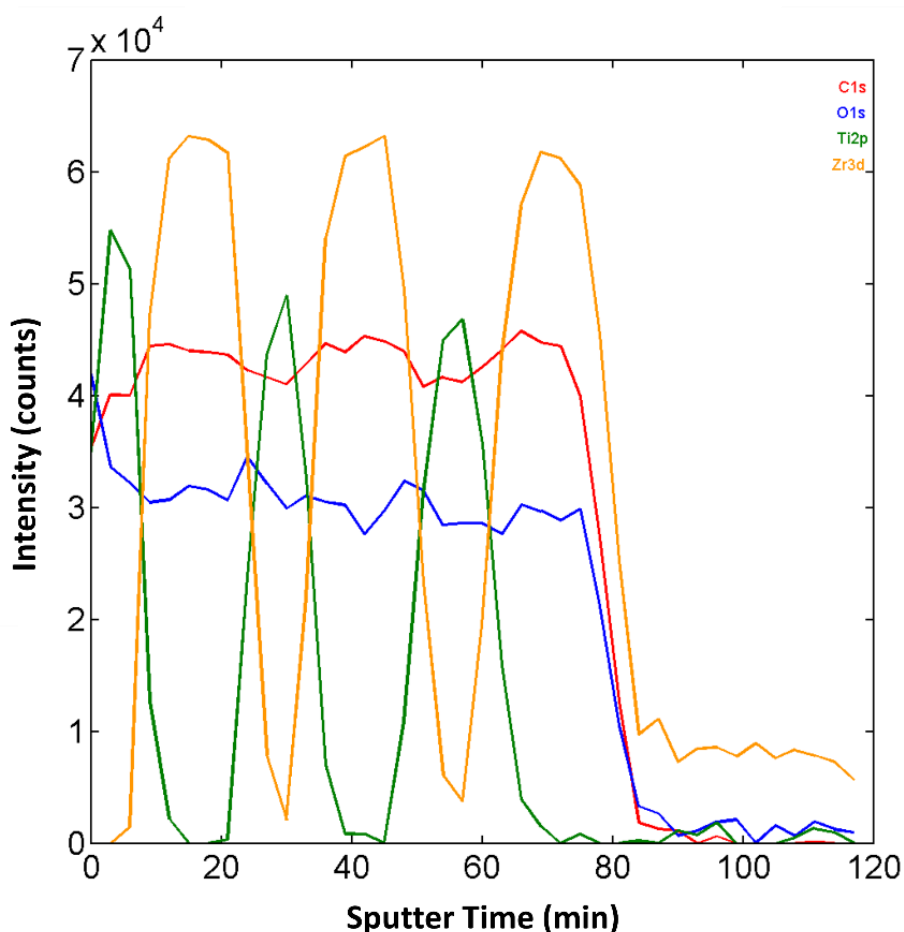


**Figure 4. 11:** XPS depth profile obtained on a laminate system consisting of three bilayers of the two MOF-type materials UiO-66 (Zr-3d transition, orange) and Ti-MIL-125 (Ti-2p transition, green) as synthesized by use of atomic layer deposition. The Ti- and Zr-rich layers are clearly separated, while the carbon (C-1s transition, red) and oxygen (O-1s transition, blue) content remains quite stable throughout the measurement. The decrease in all intensities at a sputter time of around 85 minutes is associated with nearing the silicon interface.

These findings were further confirmed by additional ToF-SIMS measurements performed on a two-bilayer laminate of the same materials. Figure 4.12 shows the corresponding graph.

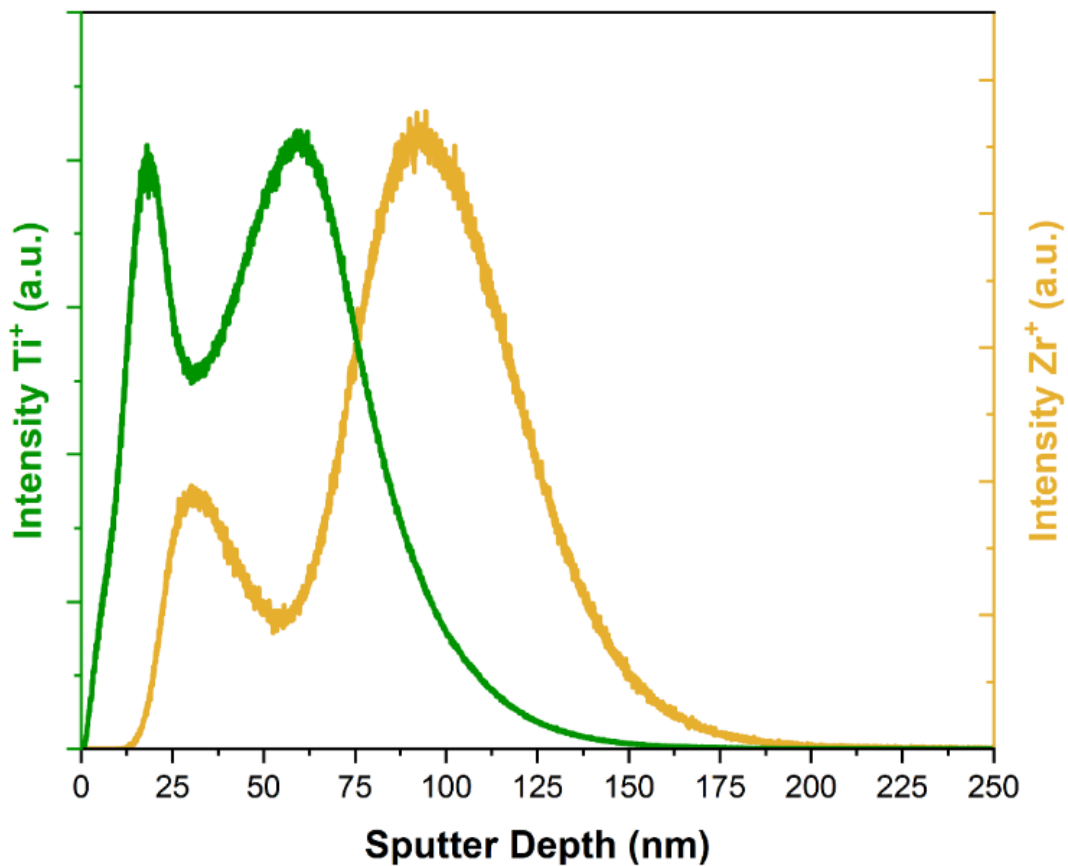


**Figure 4. 12:** ToF-SIMS-depth profile obtained on a laminate system consisting of two bilayers of the two MOF-type materials UiO-66 (orange) and Ti-MIL-125 (green) as synthesized by use of atomic layer deposition. The graph shows independent layers of Ti- and Zr-rich material. The intensities drop at approximately 150 nm sputter depth, which corresponds to approaching the silicon interface. The broadening of peaks observed in deeper material layers (peaks further to the right) is a result of ion migration induced by the bombardment of positively charged Bi-ions. This migration might be preventable by freeze-quenching the diffusion through cooling the sample to liquid nitrogen temperature during the measurement.

## 4.5 Conclusions

We were able to demonstrate the general capability of synthesizing nanolaminates consisting of ultra-thin layers of MOF-like materials by use of ALD. In principle, the developed process offers manufacturing of such materials with surpassing uniformity, purity and industrial scalability. This approach offers operators the possibility to combine materials in order to tailor or enhance certain properties with possible applications ranging from gradient materials towards low-k dielectrics or heterojunction catalysts. Moreover, we were able to apply a set of characterization techniques that allow an almost complete understanding of the structural and chemical identity of the laminate as well as the high uniformity and outstanding interface quality, that cannot be achieved with any solvent-based methods. For further investigations on the structural integrity of the partially amorphous material, we are currently evaluating EXAFS data obtained at CLAESS beamline at ALBA synchrotron in order to enhance our understanding of the underlying kinetics and thermodynamics in the arrangement of these materials. Also, we were able to increase the crystallinity of the samples through various attempts in post-synthetic modification. However, synthesis of a fully crystalline and highly uniform stack of nano-layers could not be achieved yet and still remains an open goal for future research.

## 4.6 Methods

### 4.6.1 Laminate Synthesis.

All ALD depositions were conducted using a Picosun R200 Advanced ALD-reactor, which can accommodate up to 9 precursor sources (solid, liquid, gaseous). The system's base pressure, without pulsing, was maintained at 0.1 mbar. The synthesis procedure for both MOFs, UiO-66 and Ti-MIL-125 involved a series of alternating pulse-purge cycles using two to three precursors: vapor from liquid  $\text{TiCl}_4$  and  $\text{ZrCl}_4$  (both with 99.7 % purity), liquid AcOH (99% purity) – in case of modulation involved – and solid TPA (with a purity of 99%).  $\text{TiCl}_4$  was used at its room temperature vapor pressure (~13 mbar) for feeding; also, AcOH could be used without heating due to its relatively high vapor pressure of ~21 mbar at room temperature. The solid TPA precursor was heated to 165 °C in its source, resulting in a vapor pressure of approximately 1 mbar. Accordingly, the source bottle for  $\text{ZrCl}_4$  was heated to 220 °C, resulting in a vapor pressure of nearly 1 mbar. It is worth noting that the pulsing valves for any solid precursor lines as well as the corresponding lines in our ALD system are heated to prevent the re-condensation of precursor vapor. In the case of TPA, the line and pulsing valve heating were set to 175 °C to avoid condensation, the lines for  $\text{ZrCl}_4$  were heated to 230 °C. A flow of

N<sub>2</sub> gas (purity of 5.0) was used both as a transport gas for the precursors to the substrate and as a purging gas between pulses (at a flow rate of 250 sccm). We employed a standard pulse-purge sequence of 20 s TPA - 40 s purge - 4 s TiCl<sub>4</sub>/ ZrCl<sub>4</sub> - 8 s purge – 1 s acetic acid – 1 s purge, which we believe exceeds the saturation range based on literature data. The selected pulsing pattern was determined by examining established protocols for TiO<sub>2</sub> deposition in our ALD reactor, with adjustments made based on prior literature on ALD of MOFs as well as our own studies on ALD-Ti-MIL-125. Film thicknesses were controlled by the number of pulse cycles. The substrates were heated inside the ALD chamber using a hot-wall heater arrangement. For depositions on Si-wafers, a wafer holder (fitting 100-, 200- and 300-mm samples) provided by the manufacturer was used. A 100-mm wafer was used as platform for smaller, manually cut pieces of wafers. Powder coatings were performed using an Al<sub>2</sub>O<sub>3</sub> crucible that was filled with approximately 100 mg of SiO<sub>2</sub>-NPs, placed underneath the precursor distribution place and right next to the pumping line. We note that generally the observed homogeneity of ALD MOF coatings is better for flat Si wafer substrates, while for SiO<sub>2</sub> nanoparticles variations in coating homogeneity are often observed, especially for higher powder loadings in the crucible, presumably due to flow differences through a deep powder bed. This is a challenge in line with prior reports on ALD coating of fine powders. Since the standard pulse-purge scheme was well above the saturation range no changes were applied on the ALD recipe we used for coating of wafer samples or powder samples.

#### 4.6.2 *Post deposition treatment.*

Post-deposition treatment was employed to enhance the crystalline order of the as-deposited thin films. An autoclave process was utilized, involving the use of various solvents, on Si wafers coated with ALD-MOF-like materials. In a 100 mL Teflon-lined steel autoclave equipped with a custom-designed Teflon holder for Si wafer pieces, approximately 1 mL of solvent was introduced. Despite the majority of solvents used (MeOH 99.9% purity, AcOH 99.98% purity, DMF 99.9% purity, formaldehyde 40% aq., acetone 99.9% purity, formic acid 99.9% purity, propanol 99.9% purity, propanal 99.9% purity) not producing crystalline reflexes in XRD, a successful method involved introducing 120 mg of benzoic acid (99.9 % purity, Sigma Aldrich) into an Ar-filled autoclave containing the sample material. This process was carried out at a

temperature of 160 °C for 24 hours within a sealed autoclave. Following a 6-hour cooling period, the sample was extracted, and subsequent XRD data and optical microscopy (OM) images were acquired. To eliminate unreacted linker molecules that were detected alongside crystalline material with large lattice parameters, an additional washing step was implemented using DMF (99.7% purity, Sigma Aldrich) for 24 h in a glass beaker. Due to the good solubility of TPA in DMF this step facilitated the removal of excess linker material.

#### 4.6.3 Substrates.

Si-wafers were commercially sourced from Silicon Materials (polished, (100)-oriented, P-doped wafers with 2 nm native oxide, a thickness of 525  $\mu\text{m}$  and 100 mm diameter) and cleaved by hand to  $\sim 1 \times 1$  cm pieces for our experiments.  $\text{SiO}_2$  nanoparticles were synthesized following Werner Stöber's approach.<sup>225</sup> In short, using the sol-gel method,  $\text{SiO}_2$  nanoparticles were synthesized. All reagents utilized were of analytical grade, provided by Sigma Aldrich and did not require additional purification. The following substances were employed: tetraethylorthosilicate (TEOS) with a purity of 99.9 %, absolute ethanol (EtOH) with a purity of 99.5%, concentrated ammonia and water. The procedure involved adding 4 mL of saturated ammonium hydroxide solution to 50 mL of absolute EtOH in a flask. Subsequently TEOS (0.28 mol/L) was added to the mixture. Within minutes the mixture appeared as a white suspension and was stirred for 120 minutes. After aging for 24 h, the sol underwent gelation. To obtain nanoparticles, the gel was dried at 100 °C for 2 h to remove water and organic compounds. Subsequently, the dry gel was calcined at 450 °C for 3 h, resulting in a powder that was subsequently ground to obtain nanoparticles.

#### 4.6.4 Characterization.

*Optical microscopy* images were obtained by use of an Axio CSM 700 confocal light microscope manufactured by Carl Zeiss Microscopy LLC. The access to this device was graciously provided by the Institute of Chemical Technologies and Analytics at TU Wien. *Scanning electron microscopy* was performed on a FEI Quanta 250 Field-Emission-Gun-SEM, equipped with an Everhardt-Thornley secondary electron detector. The device was operated at an electron acceleration voltage of 10 kV at a working distance of about 5 mm. EDX-spectra

were measured on an EDAX-AMETEK Octane Elite 55-detector at a voltage of 20 kV and 10 mm working distance. *Raman* spectra were measured using a 488 nm laser source equipped on a WITech alpha 300 RSA+ confocal Raman spectrometer. *XRD* measurements were performed using a X'Pert MPDII diffractometer in Bragg-Brentano geometry (with application of an  $\Omega$ -offset to suppress overwhelmingly intense single-crystal Si-wafer substrate reflections), equipped with a Cu-K $\alpha$  X-Ray source and an X'Celerator semiconductor detector. The samples were mounted on the spinning holder with a rotation speed of four seconds per rotation. *TEM* measurements and *STEM-EDX-mapping* (Figure 11) were performed on a Tecnai F20 FEG-TEM, equipped with a X-FEG, a Gatan Rio16 CCD-camera, Gatan DigiSTEM II with HAADF detector for STEM imaging, and an EDAX-AMETEK Apollo XLTW SDD EDX-detector. The operating voltage was kept at 200 kV for all measurements. *XPS* measurements were carried out on a PHI Versa Probe III-spectrometer equipped with a monochromatic Al K $\alpha$  X-ray source and a hemispherical analyzer (acceptance angle:  $\pm 22^\circ$ ). Pass energies of 112 eV and 55 eV and step widths of 0.4 eV and 0.05 eV were used for survey and detail spectra, respectively. (Excitation energy: 1486.6 eV Beam energy and spot size: 25 W onto 100  $\mu\text{m}$ ; Mean electron take-off angle:  $45^\circ$  to sample surface normal; Base pressure:  $< 7 \times 10^{-10}$  mbar, Pressure during measurements:  $< 1 \times 10^{-8}$  mbar). The sample was mounted on conductive carbon tape. A combination of electronic and ionic charge compensation was used for all measurements (automatized as provided by PHI). The binding energy (BE) scale and intensity were calibrated by using methods described in ISO15472, ISO21270 and ISO24237. The analysis depth is typically around 7-10 nm. Depth profiling was conducted using an Ar-ion gun (2 kV, 2 nA sample current,  $2 \times 2 \text{ mm}^2$ , 8 nm/min on SiO $_2$ , 3 min per sputter step). Data analysis was performed using CASA XPS software, employing transmission corrections, Shirley backgrounds<sup>226</sup> and sensitivity factors provided by PHI.<sup>227</sup> Deconvolution of spectra was carried out by using a Voigtian line shape if not stated otherwise. All content values shown are in units of relative atomic percent (at %), where the detection limit in survey measurements usually lies around 0.1 - 1 at %, depending on the element. Assignment of different components was primarily done using Refs.<sup>228,229</sup> All *ToF-SIMS* measurements in this study were conducted using an IONTOF TOF-SIMS 5 instrument. The depth profiles were obtained within an ultra-high vacuum environment of approximately  $4 \times 10^{-9}$  mbar, employing

a 25 keV Bi<sup>+</sup> primary ion beam. A field of view of 100 x 100 μm (128 x 128 pixels) was analyzed using the HCBU (high current bunched) mode for supreme mass resolution. For depth profiling a beam of O<sub>2</sub><sup>+</sup>-ions was accelerated onto the surface with an applied voltage of 2 keV on a sputter area of 300 x 300 μm. The TOF-SIMS was operated in interlaced mode, the area was rastered in sawtooth mode, all spectroscopic measurements were carried out in positive polarity.

#### **4.7 Acknowledgements:**

The authors acknowledge the use of facilities at the University Service Centre for Transmission Electron Microscopy (USTEM), Analytical Instrumentation Centre (AIC) and X-Ray Centre (XRC), TU Wien, Austria for parts of this work.

#### **4.8 Author Contributions:**

Jakob Rath and Bernhard C. Bayer planned the experiments. Bernhard C. Bayer conceived the idea. Jakob Rath developed the synthesis procedures and performed the majority of the materials characterizations in this work. Tomas Gregan, Nick Parak and Laura Aichinger assisted with synthesis and post-deposition treatment. Bernhard Fickl, Shaghayegh Naghdi, Gerlinde Habler, Markus Sauer, Annette Foelske, Florian Fahrnberger and Herbert Hutter assisted with materials characterization. Bernhard C. Bayer and Dominik Eder supervised the work. Jakob Rath and Bernhard C. Bayer wrote the manuscript with inputs from all authors.

Parts of the contents of this chapter have been established also assisted by BSc students Nick Parak, Tomas Gregan and Laura Aichinger under the assistant supervision from Mr. Jakob Rath. These results that have been jointly obtained by Mr. Parak, Mr. Gregan and Ms. Aichinger with Mr. Rath and they have also been included in Mr. Parak's, Mr. Gregan's and Ms. Aichinger's BSc theses at TU Wien.



# 5 V- and Al-free conformal atomic layer deposited TiO<sub>2</sub> diffusion-barrier-layers on porous 3D-printed TiVAI structures

## 5.1 Abstract:

Atomic-layer-deposition (ALD) is a cutting-edge technique for depositing ultrathin layers of material onto a substrate, typically with a thickness in the order of a few nanometers. We here explore this technique for creating diffusion barriers on complex three-dimensional materials, such as those used in 3D-printed titanium-based (TiVAI) medical implants.

Titanium dioxide (TiO<sub>2</sub>) is a commonly used material for ALD-based diffusion barriers. It effectively prevents the diffusion of atoms and molecules through the surface of implant materials. TiO<sub>2</sub> is a particularly attractive option due to its chemical stability and biocompatibility, making it suitable for use in medical implants.

The effectiveness of using ALD to deposit ultrathin layers of TiO<sub>2</sub> on complex 3D-printed three-dimensional TiVAI implant materials at moderate temperatures as a means of creating diffusion barriers that prevent the diffusion of potentially harmful compounds through the surface of the implant material has been demonstrated. This was achieved through characterization using state-of-the-art surface science methods such as XPS and ToF-SIMS.

## 5.2 Introduction:

In recent decades, there has been a significant increase in research on the manufacturing of lightweight materials with excellent mechanical properties and high resistance to oxidation, even at elevated temperatures.<sup>230–233</sup> During the 20th century, the main interest in developing such materials was found in the aerospace and automotive sectors. Nowadays, a major driving force for further improvement of these alloys is their utilization in the biomedical field, mainly as materials for high-performance and high-durability implants.<sup>234,235</sup>

Ti-6Al-4V (short Ti64), the most common Ti-alloy used today, is a high-strength alloy, consisting of Titanium with 6 mass per cent Aluminum and 4 % Vanadium. It is frequently used in the chemical industry<sup>236</sup>, in marine<sup>237</sup> and aerospace applications, as well as for fabrication of implants and prostheses which are either wrought, cast or produced by additive manufacturing (LPBF – laser powder bed fusion).<sup>123,238–240</sup> Whilst on a short-term base, medical application of Ti64 implants is widely common, their utilization for longer time periods is restricted due to serious concerns. Vanadium in elemental form as well as its oxides are toxic to the human organism.<sup>241</sup> Both, Al and V are associated with serious health issues and neurologic diseases.<sup>242</sup> This creates the need to either develop alternatives to this alloy, or to limit the toxicity of the implants by surface treatment of TiVAI. While the disadvantage of the first method lies mainly in the significantly higher price of alternative materials, the second option proves to be complicated, since a unified coating of a complex three-dimensional structure turns out to be very difficult in many cases. While the high surface area of these structures requires high exposure times with the used reactants<sup>243</sup>, both solvothermal as well as (classical) vapor deposition techniques PVD/CVD show clear limitations when concerning the grade of the obtained coatings. While the quality of the interfaces turn out to be a limiting factor in solvent based growth of material thin films, both PVD and CVD show restrictions in terms of uniformity, as material growth does not only occur on the surface of the substrate but already in the gas phase, hence leading to so-called edge-effects which in turn have an influence on the geometry of the nanostructured object.<sup>244</sup> One method to avoid these undesirable effects is the so called atomic layer deposition (ALD), an extension of CVD-based techniques.<sup>244,245</sup> The self-limiting nature of this technique enables the coating of complex three-dimensional substrates with high-purity, uniform and, in principle, atomically smooth material films. Since the main component of this alloy is titanium, which is biocompatible in both metallic and oxide forms, two main factors make TiO<sub>2</sub> an ideal material for coating of such implants. On the one hand, the ALD films are expected to exhibit ideal bonding to the substrate, as both phases are Ti-based, and on the other hand, its strong ionic bonds make TiO<sub>2</sub> an ideal material for thin film diffusion barriers.<sup>122,246</sup> Since the ideal diffusion barrier is a coating of not more than several nanometers thickness – given by the fact that other properties (electrical, mechanical) of the

bulk material should not be altered by the coating, characterization of the effectiveness of the deposition is not trivial due to the low amount of material as well as the content of Ti in both substrate and thin film. Therefore, application of state-of-the-art methods for surface analysis like XPS (X-Ray Photoelectron Spectroscopy) and ToF-SIMS (Time of Flight Secondary Ion Mass Spectroscopy) is essential to predict the quality of the barrier layer.

Although this topic is of great scientific as well as economic interest, to date however, hardly any work has been done on the ALD-TiO<sub>2</sub> coating of 3D-printed Ti64-implant materials.<sup>247</sup> In this chapter we show the general feasibility of ALD-thin-film coatings of TiO<sub>2</sub> on porous 3D-printed TiVAI-structures and moreover prove their homogeneity as well as the absence of V and Al. Additionally, we show a comparison of these results to the intrinsic formation of Ti/V/Al-oxides on 3D-printed TiVAI-structures by annealing them in air at various temperatures. Figure 5.1 (also shown as figure 1.6 in the introduction section) shows a sketch of the conducted experiments and the estimated results of the different approaches toward formation of an oxide film onto the implant materials.

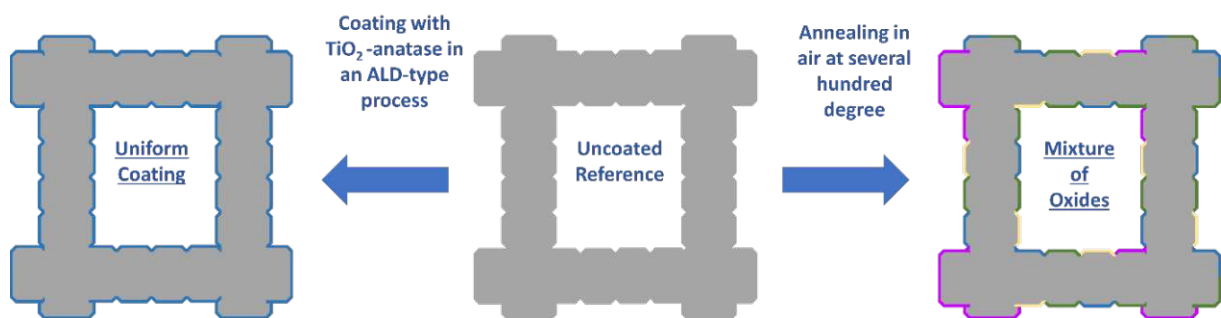


**Figure 5. 1:** Graphic Representation of the two approaches used to form an oxide layer onto the 3D-printed TiVAI-implant materials: coating of the material with TiO<sub>2</sub>-anatase, synthesized by use of ALD leads to formation of a dense, uniform film whereas annealing of the uncoated samples at 300 and 700 ° C leads to the formation of various oxides (Al, V, Ti) on the surface.

## 5.3 Experimental:

### 5.3.1 Synthesis:

#### 5.3.1.1 Laser Powder Bed Fusion.

The complex three-dimensional substrates as well as the much denser reference ingots were synthesized using laser powder bed fusion (LPBF) by JOANNEUM RESEARCH (Niklasdorf, Austria) on an EOS EOSINT M280 machine (EOS, Munich, Germany) equipped with a 400 W Nd:YAG Laser (spot size 100  $\mu\text{m}$ ) in an Argon 5.0 protective atmosphere. In order to achieve lattice struts of 200  $\mu\text{m}$  diameter, the process parameters were adapted for 20  $\mu\text{m}$  layer thickness at a low power input of 50 W. The powder used for L-PBF was commercially available gas-atomized Ti6Al4V Grade 5. The samples offered exhibit two distinct configurations: flat disks and porous monoliths, each with a 1 cm diameter. Figure 5.2 illustrates the porous monolith as supplied by Joanneum Research. To augment the total sample count, certain samples underwent cutting before undergoing ALD treatment.

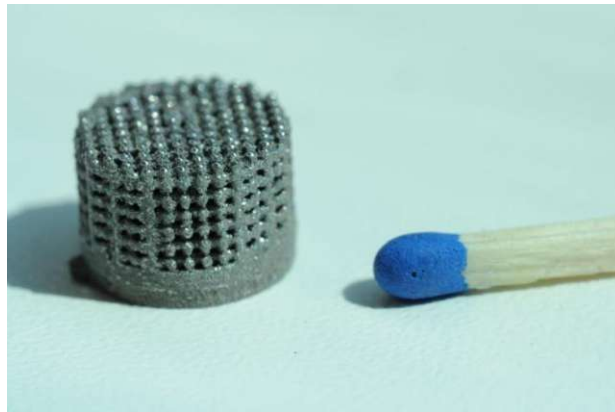


*Figure 5. 2: porous Ti6Al-monolith as printed by use of LPBF*

#### 5.3.1.2 ALD-thin-film deposition.

ALD coatings were performed using a Picosun R200 Advanced ALD-reactor, which can accommodate up to 12 precursor sources (solid, liquid, or gaseous). The reactor is optimized for coating flat samples as well as powders. The synthesis procedure for  $\text{TiO}_2$  involved consecutive pulse-purge-cycles of two precursors,  $\text{TiCl}_4$  (99.7% purity) and water (99.7% purity). The procedure was initially investigated within the temperature range of 100  $^\circ\text{C}$  to 300  $^\circ\text{C}$  on both Ti6Al-printed structures and Si-wafer-substrates (1). A high-aspect coating was

obtained by applying a typical pulse-purge sequence of 0.1 s  $\text{TiCl}_4$  – 4 s purge– 0.1 s  $\text{H}_2\text{O}$  - 4 s purge, with a saturation range well above literature data, even when applying the process onto complex shaped substrates.<sup>46</sup> Nitrogen 5.0 was used as both transport and purging gas. The pressure in the reaction chamber was approximately 1 mbar during the deposition. The applied process's linear growth was determined using Ellipsometry and XRF.

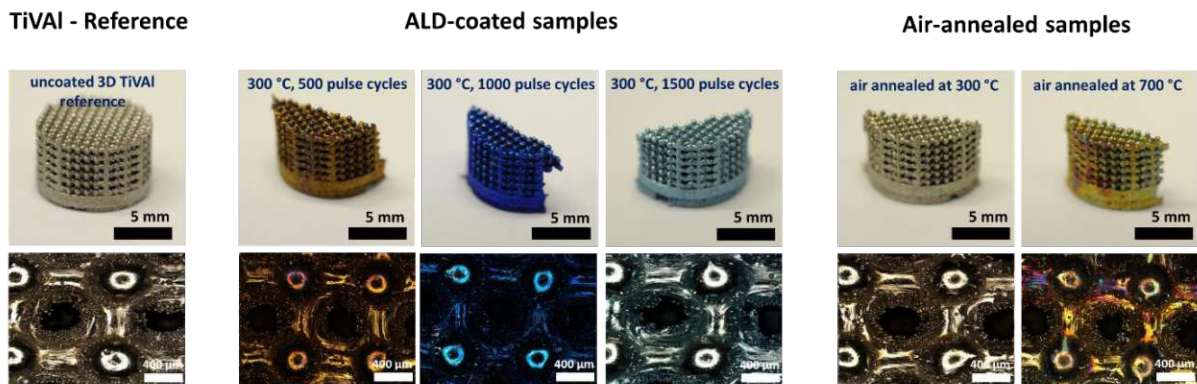
### 5.3.2 Characterization:

*Ellipsometry.* Ellipsometric film thickness measurements were carried out on a Plasmos SD 2300 ellipsometer with a rotating analyzer and a He-Ne laser ( $\lambda = 632.8$  nm) at  $68^\circ$  incidence as the light source. The ellipsometric angles (relative phase shift  $\Delta$  and amplitude ratio  $\Psi$ ) were converted into film thicknesses using the commercial instrument software which is based on the McCrackin algorithm.<sup>248</sup> An isotropic three-phase model (Si/SiO<sub>2</sub>/air) was used for the substrate and a four-phase model (Si/SiO<sub>2</sub>/anatase/air) for the sample. A measurement of the clean reference Si/SiO<sub>2</sub> yielded the thickness of the native oxide layer using values, approved for the existing setup - for the optical constants of Si ( $n = 3.865$ ,  $k = 0.020$ ) and SiO<sub>2</sub> ( $n = 1.465$ ,  $k = 0$ ). Subsequent measurement of the film- covered substrate and substitution of the substrate parameters together with assumed values for the anatase-ALD-film ( $n = 2.38$  and  $k = 0$ )<sup>249</sup> into the four-phase model allowed the calculation of the resulting layer thickness.<sup>250</sup> *XRF.* X-ray Fluorescence analysis was performed using a wavelength dispersive spectrometer manufactured by PANalytical, equipped with a Rh-source for elemental analysis of solid as well as liquid samples. Due to the design of the spectrometer the measurements are performed either in vacuum or He (in case of liquids) giving access to observation of characteristic X-rays down to B (with some restrictions mentioned later). *P-XRD.* The powder-XRD measurements shown in this work were performed using a X'Pert MPDII diffractometer in Bragg-Brentano geometry (with or without application of an  $\Omega$  -Offset), equipped with a Cu-K $\alpha$  X-Ray source and an X'Celerator semiconductor detector. The samples were mounted on the spinning holder with a rotation speed of four seconds per rotation. *Raman.* For analysis of the structure, we conducted Raman measurements, using a 488 nm laser source equipped on a WITech alpha 300 RSA+

confocal Raman spectrometer. The system utilized consists of a fibre-coupled confocal Raman microscope with four laser lines (488, 532, 633, and 785 nm) and two spectrometers optimized for the visible and near infrared range. *Optical Microscopy*. All microscope images presented in this work were obtained on Axio CSM 700, manufactured by Zeiss. The microscope is equipped with a MRc5 camera and is optimized for characterization of 3-dimensional materials with a maximum depth resolution of 20 nm. The device is capable of taking up to 100 images per second for generation of high-resolution z-stacks of complex shaped specimen. *SEM*. The scanning electron microscopy images pictured in this work were recorded on a FEI Quanta 250 (Schottky-)FEG-SEM, equipped with an ETD Secondary electron detector and an EDAX-AMETEK Octane Elite 55 detector for elemental characterization by energy-dispersive X-ray-spectroscopy. The device was operated at a voltage of 10 kV at a working distance of about 5 mm, providing a maximum resolution of roughly 2 nm. Chemical X-ray microanalysis was performed at 20 kV and 10 mm working distance. *XPS-analysis*. Determination of the chemical states of the ALD-synthesized material was accomplished by a custom designed XPS, provided by SPECS, using monochromatic AL-K $\alpha$  (1486,6 eV) radiation on a hemispheric SCIENTA RS4000 photoelectron energy analyzer. All measurements were performed in high vacuum ( $\sim 3 \cdot 10^{-9}$  mbar). *ToF-SIMS*. A TOF-SIMS 5 instrument (IONTOF GmbH, Münster, Germany) was used for the measurements presented in this work. Depth profiles were acquired in a high vacuum ( $\sim 4 \times 10^{-9}$  mbar) using a 25 keV Bi $^{+}$  primary ion beam. The burst alignment (BA) mode was used to analyze the narrow part.<sup>251-253</sup> Five bursts were fired consecutively to achieve high mass resolution and lateral resolution. To compensate for the signal loss, the non-interlaced mode was used, where ten frames with a resolution of 256 x 256 pixels were acquired at a field-of-view of 32 x 32  $\mu\text{m}^2$ . A 500 eV Oxygen beam was used as the sputter gun, and the sputter crater was set to 300 x 300  $\mu\text{m}$ . Low energy electron flooding of 21 V was used to reduce surface charging. After 1 s of sputtering, a pause of 0.1 s was placed, followed by another acquisition cycle. The measurements were stopped after 180 s.

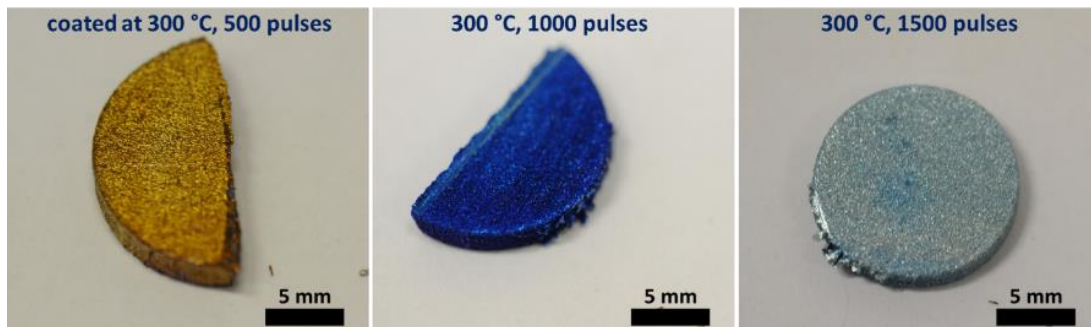
#### 5.4 Results and Discussion:

As shown by images obtained through the use of a camera and optical microscopy (Fig. 5.3 - center), coating the 3D-printed alloys with TiO<sub>2</sub> thin-films results in a clear color change that correlates closely with the corresponding layer thickness and number of pulse cycles. ALD processing shows a uniformly changed color, indicating a uniform process. The observation of uniform coating by ALD is consistent with the literature.<sup>247</sup> Cutting the samples confirmed a uniform change of color throughout the entire structure, not just on the surface. SEM-EDX spectra obtained from the surface of the coated structures showed an increase in oxygen content similar to that obtained from the surface of the inner structures of a sample cut after the ALD-coating (see Figure 5.6). When comparing these results to images of the air-oxidized reference samples, we observed either the formation of regions with various colors, corresponding to a highly heterogeneous surface, or no optical changes at all, depending on the temperature applied during the annealing step (Fig. 5.3 - right). Figure 5.4 displays the corresponding 3D-printed ingots that were coated with titania in the same run as their corresponding monolith structures from figure 5.3.



**Figure 5. 3:** From left to right, the image shows an uncoated 3D-printed TiAlV structure synthesized by LPBF, followed by three 3D-printed TiAlV structures coated with varying thicknesses of ALD-Anatase. The coatings were applied using 500, 1000, and 1500 pulse cycles, resulting in thicknesses of approximately 20 nm, 40 nm, and 60 nm, respectively. All coating processes were executed at 300 °C. From left to right, the images show the synthesized TiAlV-alloy annealed at 300 °C in air and the synthesized TiAlV-alloy annealed at 700 °C in air. The

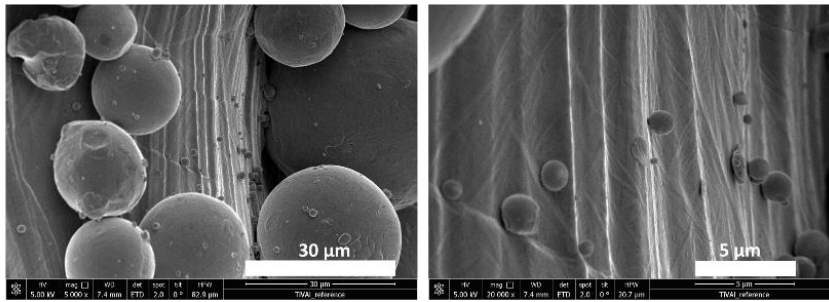
lower images display z-stacks obtained on the corresponding samples using optical microscopy, indicating the superior quality of the Titania films synthesized by ALD.



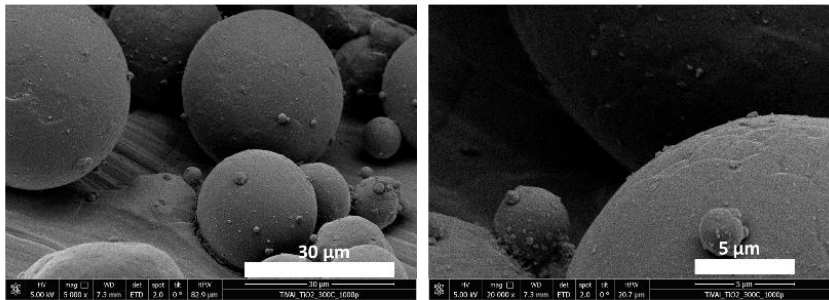
**Figure 5. 4:** camera images of 3D-printed TiVAI-ingots which in some cases were used instead of the more complex structures due to reasons of reproducibility (XRF) or sample handling (ToF-SIMS, XPS); very similarly to the 3D-structures shown in the corresponding publication the change in color is uniform and highly correlates with the thickness of the deposited anatase film

Figure 5.5 shows that SEM confirmed a uniform coating on the nanometer scale, as SEM images do not exhibit any differences between the substrate and the material coated with approximately 40 nm of Titania. We note that the spherical particles in Figure 5.5 are a direct well-known result of the 3D printing process. In Figure 5.6, SEM-EDX demonstrates a small deviation between the elemental composition on a coated area when correlating to an uncoated surface area, with relatively higher content of Al and lower content of O in the bulk material. However, the observed deviation is not enough to provide a complete explanation of the underlying process.

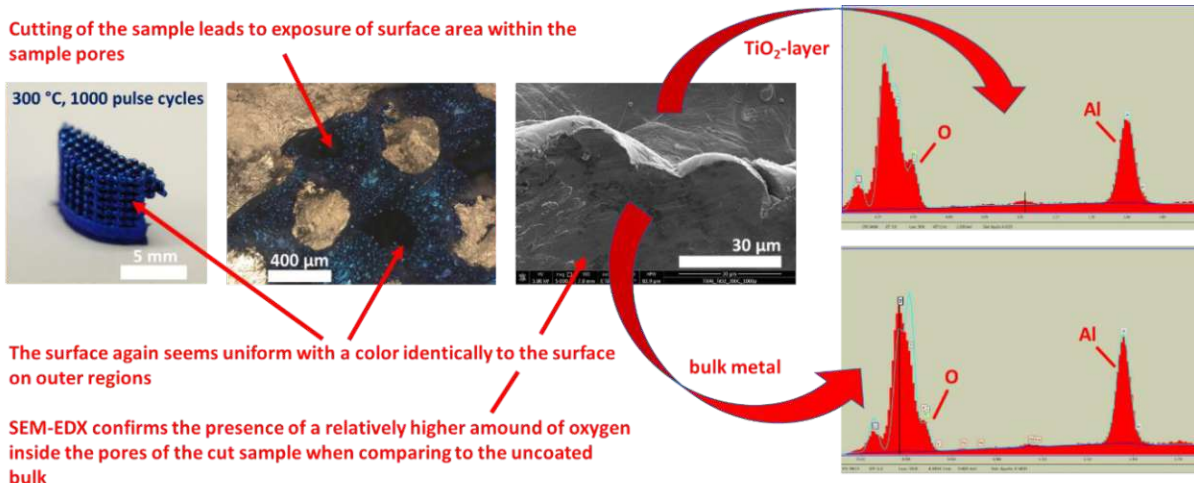
**a - TiVAI-reference**



**b - ALD-anatase, 300 ° C, 1000 pulse cycles**



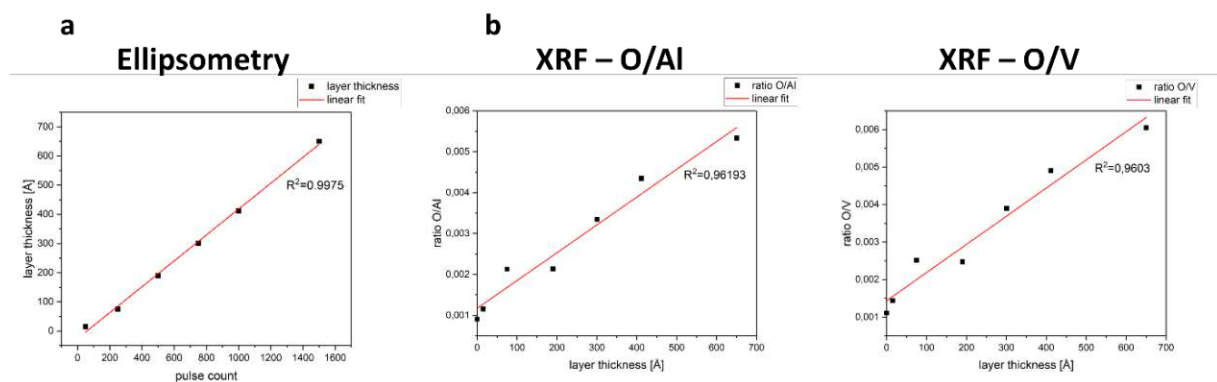
*Figure 5. 5: SEM images of the – a: uncoated TiVAI-structure and – b: a structure coated with approximately 40 nm of ALD-anatase at 300 ° C, using secondary electrons for imaging does not show any differences in morphology between the two materials. The magnifications are 5k and 20 k, respectively.*



*Figure 5. 6: The uniformity of the coating within the pores of the 3D-printed structures was characterized using simple optical measures. Additionally, SEM-EDX-point-spectra were*

performed on surfaces that were exposed by cutting a sample coated with approximately 40 nm of anatase at 300 °C. EDX on these inner surfaces confirmed an amount of oxygen relatively higher than within the bulk substrate and very similar to the oxygen content of surfaces lying on the outside of the structure.

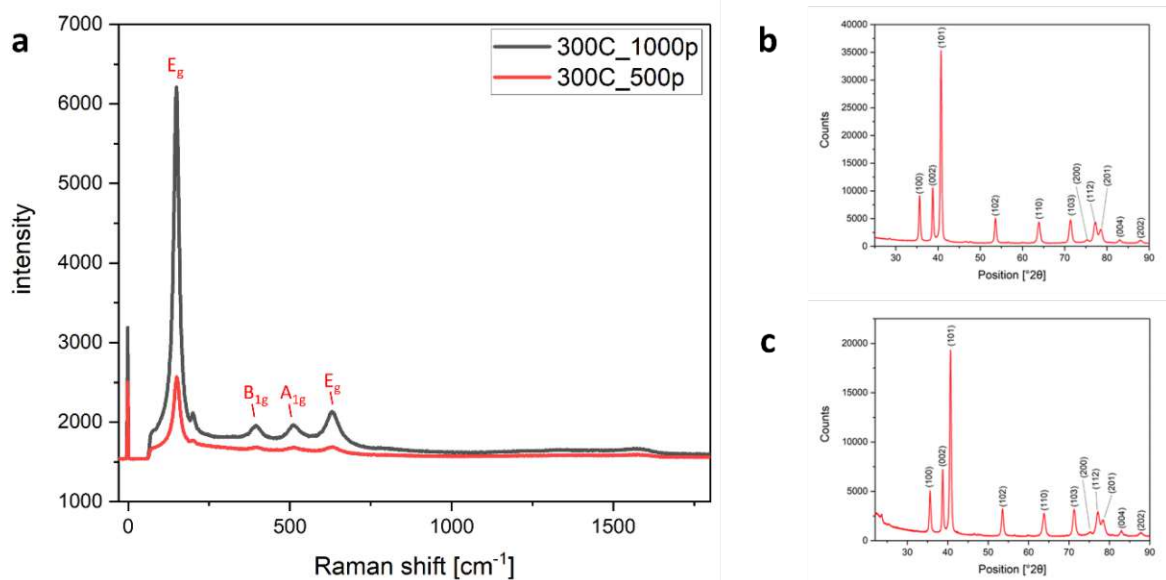
Ellipsometry was used on silicon wafers coated within the same process as the printed alloys to determine the thicknesses of the deposited Titania films (Fig. 5.7a). Due to the high roughness of the metal samples, thickness measurements using ellipsometry and XRR were not possible. Therefore, we utilized XRF to determine the material growth by analyzing the linear increase of the ratios O/Al and O/V (since titanium was present in both materials). These values were combined with the thickness values obtained by ellipsometry and XRF on the corresponding Si-wafers to estimate the layer thickness on the alloys (Fig. 5.7 b). Despite the generally lower relative response to light elements in XRF, this method still exhibits a linear fit above 96 percent.



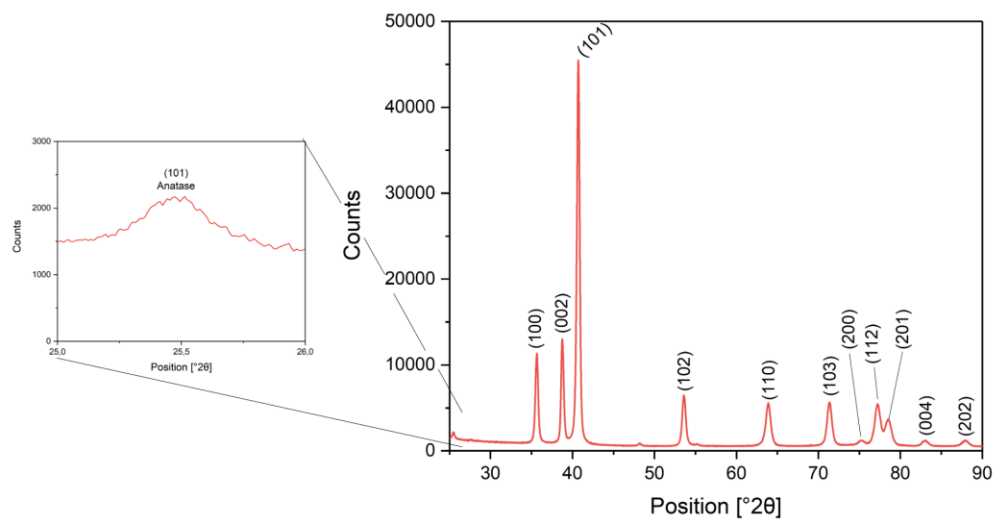
**Figure 5. 7 – a:** The layer thickness of the anatase films was determined using ellipsometry on Si-wafers coated within the same deposition run as the TiVAI-samples. The growth per cycle (GPC) value was determined to be approximately 0.4 Å/cycle, with linearity above 99.7 %. – **b:** The growth rate of the anatase films was determined using high-vacuum-wavelength-dispersive XRF (HV-WLD-XRF) on bare TiVAI, 3D-printed TiVAI ingots coated in the same deposition run as the porous TiVAI structures shown above, and Si-wafers used for ellipsometry. The fits' linear increase indicates that the applied process on the metal substrates is in the saturation regime for ALD. After method calibration, this process offers a

simple way to estimate the resulting film thickness on samples with high surface roughness that would hinder ellipsometry measurements.

To determine the structures of the Titania layer, powder XRD measurements were first applied, as shown in Figure 5.8 b-c and 5.9. The measurements indicate the presence of anatase (Figure 5.8 a and 5.9) and confirm that the structure of the TiVAI substrate material remained unchanged during the ALD-process (Fig. 5.8 b-c). This is of great importance for the mechanical properties of the resulting implant. Furthermore, Raman measurements of the samples confirmed the crystalline nature of the TiO<sub>2</sub>-film (Fig. 5.8 a). The spectrum shows characteristic bands at 150 (E<sub>g</sub>), 200 (E<sub>g</sub>), 395 (B<sub>1g</sub>), 515 (A<sub>1g</sub>) and 633 (E<sub>g</sub>) cm<sup>-1</sup>, which correspond to the characteristic modes of anatase.<sup>254</sup>

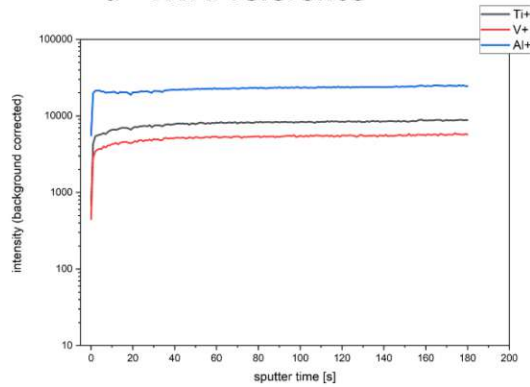
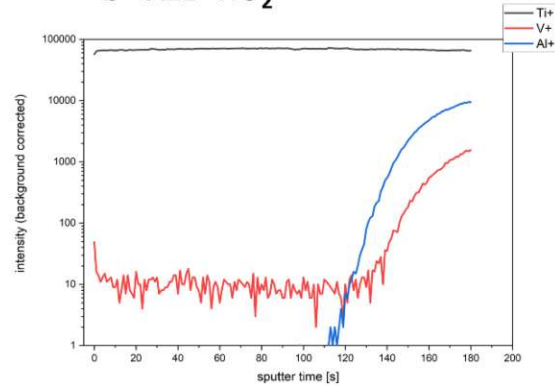
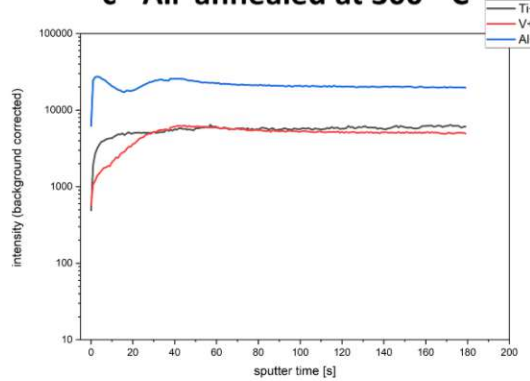
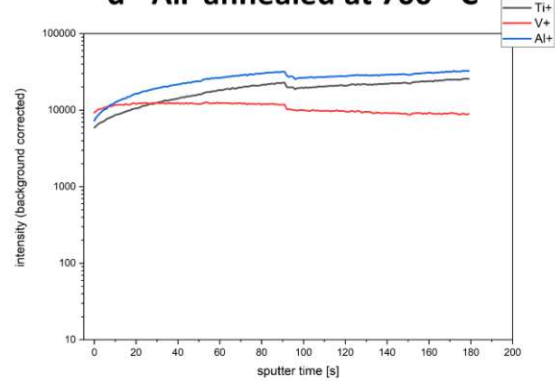


**Figure 5.8** – a: The Raman spectra of TiVAI-structures that were 3D-printed and coated with 500 (red line) and 1000 (black line) pulse cycles of ALD-anatase at 300 °C were analyzed. The thicker film exhibited all the characteristic bands that are expected for crystalline anatase. b-c – The PXRD diffraction pattern was obtained for an uncoated TiVAI-reference sample (b, upper) and the corresponding ALD-coated sample (c, lower). The patterns indicate that no phase transition occurred within the bulk material during the coating process. In the case of the coated sample, a weak anatase signal was also observed (Figure 5.9).



**Figure 5. 9:** The PXRD measurement was conducted on a 3D-printed TiVAI-structure that was coated with 1000 pulse cycles of ALD-anatase at 300 °C. The highlighted and magnified image on the left displays the (101)-reflex of the ultra-thin anatase layer.

XPS and ToF-SIMS measurements were performed to confirm the absence of Al and V within the top surface layers of the implant materials. This is crucial as a thin, enclosed, and uniform coating of the complex three-dimensional substrate is the critical point behind the concept of applying a diffusion barrier to prevent penetration. The ToF-SIMS data in Figure 5.10 a-d indicates that the top surface layers are free from contamination with the mentioned elements, while the titanium concentration remains stable throughout the measurement period. All untreated and air-annealed samples contain Al and V in the entire measurement region. Likewise, as shown in Figure 5.11 a-b, the XPS spectra do not show any signals of Al and V for the ALD coated samples, in contrast to the untreated and air-annealed samples. In both cases, measurements were taken at multiple positions on the material surface, yielding consistent results. The absence of Al and V, as determined by these techniques, indicates the high uniformity and integrity of the synthesized diffusion barrier. This suggests that there are no cracks in the film that could cause signal leakage from the bulk material. Merely observing the titanium edges would not provide a comprehensive understanding of the surface treatment quality, as shown in Figure 5.12.

**a - TiVAI-reference****b - ALD-TiO<sub>2</sub>****c - Air-annealed at 300 ° C****d - Air-annealed at 700 ° C**

**Figure 5. 10:** ToF-SIMS data of depth profile measurements performed on 3D-printed TiVAI-structures. In all graphs, the concentration of the different ions are presented in the following colors: Ti is black, V is red and Al is blue. – a: TiVAI-reference as synthesized by LPBF, all elements (Ti, V, Al) are present in close to constant amount throughout the whole depth profile – b: a TiVAI-sample coated with approximately 40 nm of TiO<sub>2</sub> by use of ALD (300 ° C, 1000 pulse cycles), neither Al nor V could be detected in the surface of the material in decisive amounts, note that the signal for V is lower by a factor of 10<sup>4</sup> compared to Ti which might be a contamination of the ALD-process, since V is a common constituent of Ti-rich ores – c: TiVAI-sample annealed in air at 300 ° C in a tube furnace, ToF-SIMS data shows high concentrations of all bulk elements on the very surface of the sample – d: TiVAI-sample annealed in air at 700 ° C in a tube furnace, ToF-SIMS data shows high concentrations of all bulk elements on the very surface of the sample

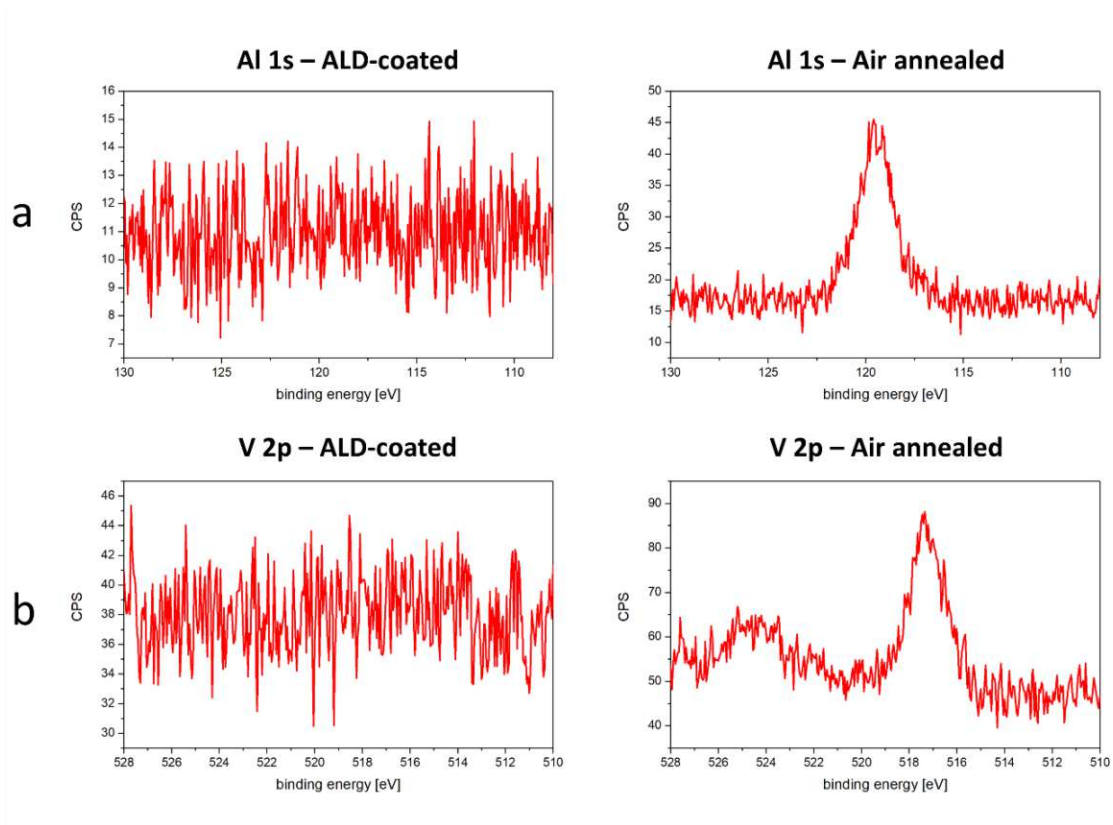


**Figure 5. 11:** XPS data performed on 3D-printed TiVAI-structures – a: detail spectra of the Al 1s transition in an energy range from 105-130 eV; while the coated sample does not show any relevant features in the observed region one can clearly see a peak correlating to aluminum in the spectrum of the sample annealed in air at 300 ° C. – b: detail spectra of the V 2p transition in an energy range from 510-528 eV; while the coated sample does not show any relevant features in the observed region one can clearly see two peaks correlating to vanadium in the spectrum of the sample annealed in air at 300 ° C.

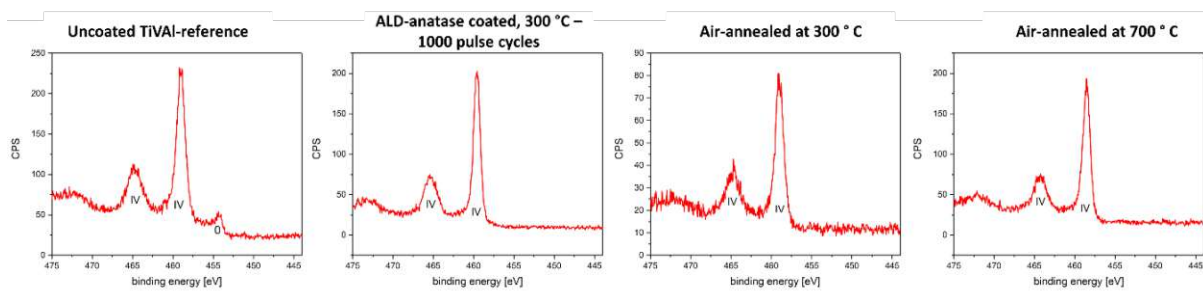


**Figure 5. 12:** The XPS-detail spectra show the Ti 2p transition for four samples: an uncoated 3D-printed TiVAI-reference alloy, a TiVAI-alloy coated with 1000 pulse cycles of ALD-TiO<sub>2</sub> at 300 ° C, an uncoated sample annealed at 300 ° C in air, and an uncoated sample annealed at

700 °C in air. The reference sample is the only one that exhibits a clear peak of a  $Ti^0$ -phase, while all the other samples only contain  $Ti^{4+}$  on their surfaces.

Clear differences are already indicated by the survey spectra of the different samples, as the Auger peaks of V and Al are much stronger in all samples except the ALD-coated ones (see Figure 5.13).

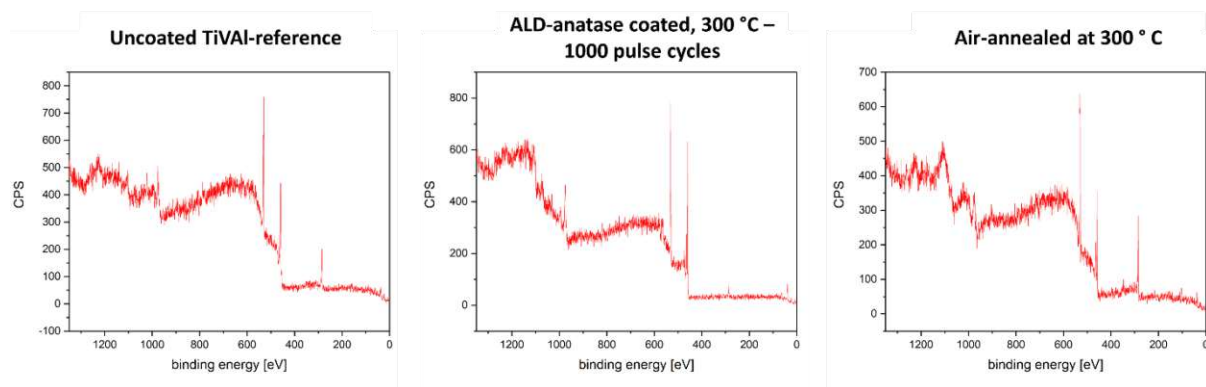


**Figure 5.13:** The survey spectra show three samples from left to right: an uncoated 3D-printed TiVAI-reference alloy, a TiVAI-alloy coated with 1000 pulse cycles of ALD- $TiO_2$  at 300 °C, and an uncoated sample annealed at 300 °C in air.

## 5.5 Conclusion:

The use of characterization techniques developed for state-of-the-art surface science demonstrated that ALD can coat complex 3D-printed TiVAI structures with a uniform film of anatase at relatively low temperatures of 300 °C. This process allows for the deposition of a dense and uniform layer of material onto the surface of such alloys. This layer acts as a diffusion barrier for potentially harmful contaminants without degrading the implant piece's mechanical performance. We emphasize that these ALD coatings from 300 °C greatly surpass coatings from direct oxidation via air annealing for both 300 °C and up to 700 °C. In particular the direct oxidation process is demonstrated to inevitably lead to Al and V in the oxide coatings, while the ALD  $TiO_2$  coatings do not have this critical disadvantage. The process has the potential to improve the performance and durability of medical implants. However,

before fully implementing this technique in biotechnology, it is necessary to conduct additional research, particularly regarding the biocompatibility of these materials and their diffusive properties in simulated situations such as artificial body fluids.

## **5.6 Acknowledgments:**

The authors acknowledge the use of facilities at the University Service Centre for Transmission Electron Microscopy (USTEM), the Analytic Instrumentation Center (AIC) and the X-Ray Center (XRC), all located at the TU Wien. Also, we would like to thank our cooperation partners at Laser Center Leoben, especially Dr. Reinhard Kaindl and DI Benjamin Meier for LPBF synthesis of the implant materials.

## **5.7 Author Contributions:**

Jakob Rath, Bernhard C. Bayer and Rainhard Kaindl planned the experiments. Bernhard C. Bayer conceived the idea. Jakob Rath developed the synthesis procedures and performed the majority of the materials characterizations in this work. Rainhard Kaindl and Benjamin Maier performed LPBF-synthesis of the alloys. Johannes Jeryczynski assisted with ALD-synthesis and characterization. Bernhard Fickl, Fabian Bohrn and Herbert Hutter assisted with materials characterization. Bernhard C. Bayer and Dominik Eder supervised the work. Jakob Rath and Bernhard C. Bayer wrote the manuscript with inputs from all authors.

Parts of the contents of this chapter have been established also assisted by BSc student Johannes Jeryczynski under the assistant supervision from Mr. Jakob Rath. These results that have been jointly obtained by Mr. Jeryczynski and Mr. Rath have also been included in Mr. Jeryczynski's BSc thesis at TU Wien.

## 6 Summary and Outlook

This summary starts with a description of the challenges overcome in this thesis:

After the successful commissioning and activation of the Picosun R200 ALD system at the TU Wien, first material calibrations were performed using trimethylaluminum (TMA) and water as precursors for the synthesis of  $\text{Al}_2\text{O}_3$  and  $\text{TiCl}_4$  and water for the formation of ultrathin Titania films. Some of the characterization methods highlighted in the main part of this work were evaluated for their potential use in understanding these thin film materials. The growth observed was in close correlation with the current literature on ALD oxides, which allowed the main focus of the research to be set on more complex materials and depositions on more complicated geometries.

Experiments in the following years encountered many difficulties, most of which were solved.

The first challenge was to determine the thickness of the resulting MOF-like layers using ellipsometry. As neither the physical density nor the refractive index of the new materials was known, thickness measurements using a laser ellipsometer could not be performed due to the lack of known parameters. The layers were too thin to measure their thickness using a Dektak Stylus XT profilometer, and the mechanical properties of the substrate and the thin films were too different to freeze-break (liquid nitrogen) them in a way that would allow the thickness to be measured on the resulting cross section using SEM. All these problems could be overcome by using XRR to determine the thickness of the thin films, as it also gave us access to the densities of the materials. The counter movement, the method setup, the measurements themselves and the data evaluation proved to be very time consuming. To improve the speed of the thickness determination, we used the data obtained in XRR to calibrate a UHV wavelength dispersive XRF setup with elemental ratios (e.g. Ti/Si; to adjust for different sample sizes) in order to obtain a result within a few minutes instead of days. In principle, this method is very simple and can be used to determine the thickness of materials containing all elements up to B.

One challenge that was part of our discussions from the very beginning was the expected low crystallinity of MOFs produced by an ALD process, which had been previously reported by

Lausund et al. It seemed that under the process conditions of ALD, the building blocks of the MOF films did not have enough energy to self-assemble as they do under the usual solvothermal synthesis conditions. Instead, various types of bonding between the central metal nodes and the linkers, as well as high levels of unreacted excess linker molecules, limit the structural order within the material. However, in-situ modulation of the process using smaller monofunctional ligands (e.g. AcOH) can dramatically increase crystallinity. Post-deposition treatments using autoclaves may be another way to increase structural uniformity. In our research we have tested both options and have seen changes in crystallinity depending on the type of material. While modulation with acetic acid dramatically improved the Raman signals, no improvement in XRD crystallinity was observed. XRD reflections only appeared after treatment of the MOF films with benzoic acid in a Teflon-lined steel autoclave. During this treatment, the unity and uniformity of the films completely disappeared. We however note that for our ALD MOF films we measure specific surface areas (Chapter 3) close to the solvothermal benchmarks, which clearly delineates our films as MOFs, which distinguishing features are often seen as crystallinity and porosity.

In order to gain a detailed understanding of the new materials, a wide range of different characterization methods have been applied, each of which has contributed a piece of the jigsaw to our picture of ALD-MOFs. The data presented in this thesis include some very dedicated and sophisticated results that demonstrate the high quality, unity and uniformity of these materials on an unprecedented scale, and provide clear indications that ALD can be used to synthesize state-of-the-art heterogeneous catalysts on almost any substrate, and even to design highly complex multilayer systems that can be used in the semiconductor industry or in aerospace engineering.

# 7 Bibliography

- (1) *Publications Output: U.S. Trends and International Comparisons | NSF - National Science Foundation*. <https://ncses.nsf.gov/pubs/nsb20206/publication-output-by-field-of-science> (accessed 2023-12-12).
- (2) Hamilton, E. *Top 10 Most Popular Sciences among Students in 2019*. Science Times. <https://www.sciencetimes.com/articles/23904/20190925/top-10-most-popular-sciences-among-students-in-2019.htm> (accessed 2023-12-12).
- (3) Geim, A. K.; Novoselov, K. S. The Rise of Graphene. *Nat. Mater.* **2007**, *6* (3), 183–191. <https://doi.org/10.1038/nmat1849>.
- (4) Gupta, T.; Elibol, K.; Hummel, S.; Stöger-Pollach, M.; Mangler, C.; Habler, G.; Meyer, J. C.; Eder, D.; Bayer, B. C. Resolving Few-Layer Antimonene/Graphene Heterostructures. *Npj 2D Mater. Appl.* **2021**, *5* (1), 1–11. <https://doi.org/10.1038/s41699-021-00230-3>.
- (5) Greene, J. E. Review Article: Tracing the Recorded History of Thin-Film Sputter Deposition: From the 1800s to 2017. *J. Vac. Sci. Technol. Vac. Surf. Films* **2017**, *35* (5), 05C204. <https://doi.org/10.1116/1.4998940>.
- (6) *Synthesis of Graphene-layer Nanosheet Coatings by PECVD - ScienceDirect*. <https://www.sciencedirect.com/science/article/pii/S2214785315007944> (accessed 2024-01-05).
- (7) Güniat, L.; Caroff, P.; Fontcuberta i Morral, A. Vapor Phase Growth of Semiconductor Nanowires: Key Developments and Open Questions. *Chem. Rev.* **2019**, *119* (15), 8958–8971. <https://doi.org/10.1021/acs.chemrev.8b00649>.
- (8) Kuech, T. F. Metal-Organic Vapor Phase Epitaxy of Compound Semiconductors. *Mater. Sci. Rep.* **1987**, *2* (1), 1–49. [https://doi.org/10.1016/0920-2307\(87\)90002-8](https://doi.org/10.1016/0920-2307(87)90002-8).
- (9) Jiang, J.; Li, N.; Zou, J.; Zhou, X.; Eda, G.; Zhang, Q.; Zhang, H.; Li, L.-J.; Zhai, T.; S. Wee, A. T. Synergistic Additive-Mediated CVD Growth and Chemical Modification of 2D Materials. *Chem. Soc. Rev.* **2019**, *48* (17), 4639–4654. <https://doi.org/10.1039/C9CS00348G>.
- (10) Stüber, M.; Leiste, H.; Ulrich, S.; Skokan, A. Development of Tailored Coating Concepts for CVD and PVD Deposition of Multifunctional Coatings - A Review. *Int. J. Mater. Res.* **1999**, *90* (10), 774–779. <https://doi.org/10.1515/ijmr-1999-901004>.
- (11) Habig, K. -H. Chemical Vapor Deposition and Physical Vapor Deposition Coatings: Properties, Tribological Behavior, and Applications. *J. Vac. Sci. Technol. A* **1986**, *4* (6), 2832–2843. <https://doi.org/10.1116/1.573687>.
- (12) Schalk, N.; Tkadletz, M.; Mitterer, C. Hard Coatings for Cutting Applications: Physical vs. Chemical Vapor Deposition and Future Challenges for the Coatings Community. *Surf. Coat. Technol.* **2022**, *429*, 127949. <https://doi.org/10.1016/j.surfcoat.2021.127949>.
- (13) Moshfegh, A. Z. Pvd Growth Method: Physics and Technology. In *Physics and Technology of Thin Films*; WORLD SCIENTIFIC, 2004; pp 28–53. [https://doi.org/10.1142/9789812702876\\_0002](https://doi.org/10.1142/9789812702876_0002).

- (14) Yanguas-Gil, A. *Growth and Transport in Nanostructured Materials: Reactive Transport in PVD, CVD, and ALD*; Springer, 2016.
- (15) Kodas, T. T.; Hampden-Smith, M. J. *The Chemistry of Metal CVD*; John Wiley & Sons, 2008.
- (16) Mattox, D. M. *Handbook of Physical Vapor Deposition (PVD) Processing*; William Andrew, 2010.
- (17) Azad Malik, M.; O'brien, P. Basic Chemistry of CVD and ALD Precursors. **2008**.  
<https://doi.org/10.1039/9781847558794-00207>.
- (18) Choy, K. L. Chemical Vapour Deposition of Coatings. *Prog. Mater. Sci.* **2003**, *48* (2), 57–170.  
[https://doi.org/10.1016/S0079-6425\(01\)00009-3](https://doi.org/10.1016/S0079-6425(01)00009-3).
- (19) Lackner, J. M.; Waldhauser, W.; Hartmann, P.; Bruckert, F.; Weidenhaupt, M.; Major, R.; Sanak, M.; Wiesinger, M.; Heim, D. Hemocompatibility of Inorganic Physical Vapor Deposition (PVD) Coatings on Thermoplastic Polyurethane Polymers. *J. Funct. Biomater.* **2012**, *3* (2), 283–297.  
<https://doi.org/10.3390/jfb3020283>.
- (20) Singh, A.; Moun, M.; Singh, R. Effect of Different Precursors on CVD Growth of Molybdenum Disulfide. *J. Alloys Compd.* **2019**, *782*, 772–779. <https://doi.org/10.1016/j.jallcom.2018.12.230>.
- (21) Devi, A. 'Old Chemistries' for New Applications: Perspectives for Development of Precursors for MOCVD and ALD Applications. *Coord. Chem. Rev.* **2013**, *257* (23), 3332–3384.  
<https://doi.org/10.1016/j.ccr.2013.07.025>.
- (22) Zhao, S.; Zhou, F.; Li, Z.; Liu, H. Effect of Precursor Purity and Flow Rate on the CVD Growth of Hexagonal Boron Nitride. *J. Alloys Compd.* **2016**, *688*, 1006–1012.  
<https://doi.org/10.1016/j.jallcom.2016.07.117>.
- (23) Wang, B.; Fu, X.; Song, S.; Chu, H. O.; Gibson, D.; Li, C.; Shi, Y.; Wu, Z. Simulation and Optimization of Film Thickness Uniformity in Physical Vapor Deposition. *Coatings* **2018**, *8* (9), 325.  
<https://doi.org/10.3390/coatings8090325>.
- (24) Crowell, J. E. Chemical Methods of Thin Film Deposition: Chemical Vapor Deposition, Atomic Layer Deposition, and Related Technologies. *J. Vac. Sci. Technol. A* **2003**, *21* (5), S88–S95.  
<https://doi.org/10.1116/1.1600451>.
- (25) Cale, T. S.; Raupp, G. B. A Unified Line-of-sight Model of Deposition in Rectangular Trenches. *J. Vac. Sci. Technol. B Microelectron. Process. Phenom.* **1990**, *8* (6), 1242–1248.  
<https://doi.org/10.1116/1.584901>.
- (26) Mayer, T. M.; Elam, J. W.; George, S. M.; Kotula, P. G.; Goeke, R. S. Atomic-Layer Deposition of Wear-Resistant Coatings for Microelectromechanical Devices. *Appl. Phys. Lett.* **2003**, *82* (17), 2883–2885. <https://doi.org/10.1063/1.1570926>.
- (27) *ASM Microchemistry Ltd | HYCOAT*. <http://www.hycoat.eu/?q=AboutASM> (accessed 2023-12-12).
- (28) *Atomic Layer Deposition of Two-Dimensional Metal Dichalcogenides*.  
<https://www.atomiclayerdeposition.com/science/theses/ald-of-two-dimensional-metal-dichalcogenides> (accessed 2024-06-27).

- (29) Ren, J.; Jen, T.-C. Atomic Layer Deposition (ALD) Assisting the Visibility of Metal-Organic Frameworks (MOFs) Technologies. *Coord. Chem. Rev.* **2021**, *430*, 213734. <https://doi.org/10.1016/j.ccr.2020.213734>.
- (30) Ylivaara, O. M. E.; Liu, X.; Kilpi, L.; Lyytinen, J.; Schneider, D.; Laitinen, M.; Julin, J.; Ali, S.; Sintonen, S.; Berdova, M.; Haimi, E.; Sajavaara, T.; Ronkainen, H.; Lipsanen, H.; Koskinen, J.; Hannula, S.-P.; Puurunen, R. L. Aluminum Oxide from Trimethylaluminum and Water by Atomic Layer Deposition: The Temperature Dependence of Residual Stress, Elastic Modulus, Hardness and Adhesion. *Thin Solid Films* **2014**, *552*, 124–135. <https://doi.org/10.1016/j.tsf.2013.11.112>.
- (31) Kim, S.; Lee, S.-H.; Jo, I. H.; Seo, J.; Yoo, Y.-E.; Kim, J. H. Influence of Growth Temperature on Dielectric Strength of Al<sub>2</sub>O<sub>3</sub> Thin Films Prepared via Atomic Layer Deposition at Low Temperature. *Sci. Rep.* **2022**, *12* (1), 5124. <https://doi.org/10.1038/s41598-022-09054-7>.
- (32) Malygin, A. A.; Drozd, V. E.; Malkov, A. A.; Smirnov, V. M. From V. B. Aleskovskii's "Framework" Hypothesis to the Method of Molecular Layering/Atomic Layer Deposition. *Chem. Vap. Depos.* **2015**, *21* (10-11-12), 216–240. <https://doi.org/10.1002/cvde.201502013>.
- (33) Puurunen, R. L. A Short History of Atomic Layer Deposition: Tuomo Suntola's Atomic Layer Epitaxy. *Chem. Vap. Depos.* **2014**, *20* (10-11-12), 332–344. <https://doi.org/10.1002/cvde.201402012>.
- (34) Suntola, T.; Antson, J. Method for Producing Compound Thin Films. US4058430A, November 15, 1977. <https://patents.google.com/patent/US4058430/en> (accessed 2023-12-12).
- (35) Nilsen, O.; Klepper, K.; Nielsen, H.; Fjellvåg, H. Deposition of Organic- Inorganic Hybrid Materials by Atomic Layer Deposition. *ECS Trans.* **2008**, *16* (4), 3. <https://doi.org/10.1149/1.2979975>.
- (36) Barnholt Klepper, K.; Nilsen, O.; Fjellvåg, H. Deposition of Thin Films of Organic–Inorganic Hybrid Materials Based on Aromatic Carboxylic Acids by Atomic Layer Deposition. *Dalton Trans.* **2010**, *39* (48), 11628–11635. <https://doi.org/10.1039/C0DT00817F>.
- (37) Peng, Q.; Gong, B.; VanGundy, R. M.; Parsons, G. N. "Zincone" Zinc Oxide–Organic Hybrid Polymer Thin Films Formed by Molecular Layer Deposition. *Chem. Mater.* **2009**, *21* (5), 820–830. <https://doi.org/10.1021/cm8020403>.
- (38) Hakim, L. F.; Blackson, J.; George, S. M.; Weimer, A. W. Nanocoating Individual Silica Nanoparticles by Atomic Layer Deposition in a Fluidized Bed Reactor. *Chem. Vap. Depos.* **2005**, *11* (10), 420–425. <https://doi.org/10.1002/cvde.200506392>.
- (39) Niu, W.; Li, X.; Karuturi, S. K.; Fam, D. W.; Fan, H.; Shrestha, S.; Wong, L. H.; Tok, A. I. Y. Applications of Atomic Layer Deposition in Solar Cells. *Nanotechnology* **2015**, *26* (6), 064001. <https://doi.org/10.1088/0957-4484/26/6/064001>.
- (40) Kim, H. Characteristics and Applications of Plasma Enhanced-Atomic Layer Deposition. *Thin Solid Films* **2011**, *519* (20), 6639–6644. <https://doi.org/10.1016/j.tsf.2011.01.404>.
- (41) Wang, B.; Huang, W.; Chi, L.; Al-Hashimi, M.; Marks, T. J.; Facchetti, A. High-k Gate Dielectrics for Emerging Flexible and Stretchable Electronics. *Chem. Rev.* **2018**, *118* (11), 5690–5754. <https://doi.org/10.1021/acs.chemrev.8b00045>.

- (42) Wang, J.; Huang, Q.; Gao, Y.; Shi, N.; Ge, Q.; Meng, H.; Zhang, M.; Wang, X. Molecular and Atomic Layer Deposition of Hybrid Polyimide–Al<sub>2</sub>O<sub>3</sub> Gate Dielectrics for Flexible Electronic Devices. *Chem. Mater.* **2022**, *34* (20), 9119–9133. <https://doi.org/10.1021/acs.chemmater.2c01997>.
- (43) Nam, T.; Seo, S.; Kim, H. Atomic Layer Deposition of a Uniform Thin Film on Two-Dimensional Transition Metal Dichalcogenides. *J. Vac. Sci. Technol. A* **2020**, *38* (3), 030803. <https://doi.org/10.1116/6.0000068>.
- (44) Kim, H. G.; Lee, H.-B.-R. Atomic Layer Deposition on 2D Materials. *Chem. Mater.* **2017**, *29* (9), 3809–3826. <https://doi.org/10.1021/acs.chemmater.6b05103>.
- (45) Salmi, L. D.; Heikkilä, M. J.; Puukilainen, E.; Sajavaara, T.; Grosso, D.; Ritala, M. Studies on Atomic Layer Deposition of MOF-5 Thin Films. *Microporous Mesoporous Mater.* **2013**, *182*, 147–154. <https://doi.org/10.1016/j.micromeso.2013.08.024>.
- (46) Lausund, K. B.; Nilsen, O. All-Gas-Phase Synthesis of UiO-66 through Modulated Atomic Layer Deposition. *Nat. Commun.* **2016**, *7* (1), 13578. <https://doi.org/10.1038/ncomms13578>.
- (47) Li, H.; Wang, K.; Sun, Y.; Lollar, C. T.; Li, J.; Zhou, H.-C. Recent Advances in Gas Storage and Separation Using Metal–Organic Frameworks. *Mater. Today* **2018**, *21* (2), 108–121. <https://doi.org/10.1016/j.mattod.2017.07.006>.
- (48) Li, H.; Li, L.; Lin, R.-B.; Zhou, W.; Zhang, Z.; Xiang, S.; Chen, B. Porous Metal–Organic Frameworks for Gas Storage and Separation: Status and Challenges. *EnergyChem* **2019**, *1* (1), 100006. <https://doi.org/10.1016/j.enchem.2019.100006>.
- (49) Naghdi, S.; Cherevan, A.; Giesriegl, A.; Guillet-Nicolas, R.; Biswas, S.; Gupta, T.; Wang, J.; Haunold, T.; Bayer, B. C.; Rupprechter, G.; Toroker, M. C.; Kleitz, F.; Eder, D. Selective Ligand Removal to Improve Accessibility of Active Sites in Hierarchical MOFs for Heterogeneous Photocatalysis. *Nat. Commun.* **2022**, *13* (1), 282. <https://doi.org/10.1038/s41467-021-27775-7>.
- (50) Wang, J.; Cherevan, A. S.; Hannecart, C.; Naghdi, S.; Nandan, S. P.; Gupta, T.; Eder, D. Ti-Based MOFs: New Insights on the Impact of Ligand Composition and Hole Scavengers on Stability, Charge Separation and Photocatalytic Hydrogen Evolution. *Appl. Catal. B Environ.* **2021**, *283*, 119626. <https://doi.org/10.1016/j.apcatb.2020.119626>.
- (51) A. Dolgoplova, E.; M. Rice, A.; R. Martin, C.; B. Shustova, N. Photochemistry and Photophysics of MOFs: Steps towards MOF-Based Sensing Enhancements. *Chem. Soc. Rev.* **2018**, *47* (13), 4710–4728. <https://doi.org/10.1039/C7CS00861A>.
- (52) Wang, Y.; Zhang, Y.; Hou, C.; Liu, M. Magnetic Fe<sub>3</sub>O<sub>4</sub>@MOFs Decorated Graphene Nanocomposites as Novel Electrochemical Sensor for Ultrasensitive Detection of Dopamine. *RSC Adv.* **2015**, *5* (119), 98260–98268. <https://doi.org/10.1039/C5RA20996J>.
- (53) Shiozawa, H.; Bayer, B. C.; Peterlik, H.; Meyer, J. C.; Lang, W.; Pichler, T. Doping of Metal–Organic Frameworks towards Resistive Sensing. *Sci. Rep.* **2017**, *7* (1), 1–8.
- (54) Abánades Lázaro, I.; Forgan, R. S. Application of Zirconium MOFs in Drug Delivery and Biomedicine. *Coord. Chem. Rev.* **2019**, *380*, 230–259. <https://doi.org/10.1016/j.ccr.2018.09.009>.

- (55) Lawson, H. D.; Walton, S. P.; Chan, C. Metal–Organic Frameworks for Drug Delivery: A Design Perspective. *ACS Appl. Mater. Interfaces* **2021**, *13* (6), 7004–7020. <https://doi.org/10.1021/acscami.1c01089>.
- (56) Jiao, L.; Seow, J. Y. R.; Skinner, W. S.; Wang, Z. U.; Jiang, H.-L. Metal–Organic Frameworks: Structures and Functional Applications. *Mater. Today* **2019**, *27*, 43–68. <https://doi.org/10.1016/j.mattod.2018.10.038>.
- (57) Masters, A. F.; Maschmeyer, T. Zeolites – From Curiosity to Cornerstone. *Microporous Mesoporous Mater.* **2011**, *142* (2), 423–438. <https://doi.org/10.1016/j.micromeso.2010.12.026>.
- (58) Muslim, M.; Ahmad, M.; Muslim, M.; Ahmad, M. Historical Developments in Synthesis Approaches and Photocatalytic Perspectives of Metal–Organic Frameworks. In *Photocatalysts - New Perspectives*; IntechOpen, 2022. <https://doi.org/10.5772/intechopen.107119>.
- (59) Li, H.; Eddaoudi, M.; O’Keeffe, M.; Yaghi, O. M. Design and Synthesis of an Exceptionally Stable and Highly Porous Metal–Organic Framework. *Nature* **1999**, *402* (6759), 276–279. <https://doi.org/10.1038/46248>.
- (60) Eddaoudi, M.; Li, H.; Yaghi, O. M. Highly Porous and Stable Metal–Organic Frameworks: Structure Design and Sorption Properties. *J. Am. Chem. Soc.* **2000**, *122* (7), 1391–1397. <https://doi.org/10.1021/ja9933386>.
- (61) Furukawa, H.; Cordova, K. E.; O’Keeffe, M.; Yaghi, O. M. The Chemistry and Applications of Metal–Organic Frameworks. *Science* **2013**, *341* (6149), 1230444. <https://doi.org/10.1126/science.1230444>.
- (62) Wu, C.-D.; Hu, A.; Zhang, L.; Lin, W. A Homochiral Porous Metal–Organic Framework for Highly Enantioselective Heterogeneous Asymmetric Catalysis. *J. Am. Chem. Soc.* **2005**, *127* (25), 8940–8941. <https://doi.org/10.1021/ja052431t>.
- (63) Ibrahim, M.; Sabouni, R.; A. Hussein, G. Anti-Cancer Drug Delivery Using Metal Organic Frameworks (MOFs). *Curr. Med. Chem.* **2017**, *24* (2), 193–214.
- (64) Qian, Q.; Asinger, P. A.; Lee, M. J.; Han, G.; Mizrahi Rodriguez, K.; Lin, S.; Benedetti, F. M.; Wu, A. X.; Chi, W. S.; Smith, Z. P. MOF-Based Membranes for Gas Separations. *Chem. Rev.* **2020**, *120* (16), 8161–8266. <https://doi.org/10.1021/acs.chemrev.0c00119>.
- (65) Kumar, P.; Deep, A.; Kim, K.-H. Metal Organic Frameworks for Sensing Applications. *TrAC Trends Anal. Chem.* **2015**, *73*, 39–53. <https://doi.org/10.1016/j.trac.2015.04.009>.
- (66) Grünker, R.; Bon, V.; Müller, P.; Stoeck, U.; Krause, S.; Mueller, U.; Senkovska, I.; Kaskel, S. A New Metal–Organic Framework with Ultra-High Surface Area. *Chem. Commun.* **2014**, *50* (26), 3450–3452. <https://doi.org/10.1039/C4CC00113C>.
- (67) He, T.; Kong, X.-J.; Li, J.-R. Chemically Stable Metal–Organic Frameworks: Rational Construction and Application Expansion. *Acc. Chem. Res.* **2021**, *54* (15), 3083–3094. <https://doi.org/10.1021/acs.accounts.1c00280>.
- (68) Mandal, S.; Natarajan, S.; Mani, P.; Pankajakshan, A. Post-Synthetic Modification of Metal–Organic Frameworks Toward Applications. *Adv. Funct. Mater.* **2021**, *31* (4), 2006291. <https://doi.org/10.1002/adfm.202006291>.

- (69) Yin, Z.; Wan, S.; Yang, J.; Kurmoo, M.; Zeng, M.-H. Recent Advances in Post-Synthetic Modification of Metal–Organic Frameworks: New Types and Tandem Reactions. *Coord. Chem. Rev.* **2019**, *378*, 500–512. <https://doi.org/10.1016/j.ccr.2017.11.015>.
- (70) Nelson, A. P.; Parrish, D. A.; Cambrea, L. R.; Baldwin, L. C.; Trivedi, N. J.; Mulfort, K. L.; Farha, O. K.; Hupp, J. T. Crystal to Crystal Guest Exchange in a Mixed Ligand Metal–Organic Framework. *Cryst. Growth Des.* **2009**, *9* (11), 4588–4591. <https://doi.org/10.1021/cg900735n>.
- (71) Abednatanzi, S.; Derakhshandeh, P. G.; Depauw, H.; Coudert, F.-X.; Vrielinck, H.; Voort, P. V. D.; Leus, K. Mixed-Metal Metal–Organic Frameworks. *Chem. Soc. Rev.* **2019**, *48* (9), 2535–2565. <https://doi.org/10.1039/C8CS00337H>.
- (72) Masoomi, M. Y.; Morsali, A.; Dhakshinamoorthy, A.; Garcia, H. Mixed-Metal MOFs: Unique Opportunities in Metal–Organic Framework (MOF) Functionality and Design. *Angew. Chem.* **2019**, *131* (43), 15330–15347. <https://doi.org/10.1002/ange.201902229>.
- (73) Liang, Z.; Qu, C.; Guo, W.; Zou, R.; Xu, Q. Pristine Metal–Organic Frameworks and Their Composites for Energy Storage and Conversion. *Adv. Mater.* **2018**, *30* (37), 1702891. <https://doi.org/10.1002/adma.201702891>.
- (74) Zhang, X.; Chen, A.; Zhong, M.; Zhang, Z.; Zhang, X.; Zhou, Z.; Bu, X.-H. Metal–Organic Frameworks (MOFs) and MOF-Derived Materials for Energy Storage and Conversion. *Electrochem. Energy Rev.* **2019**, *2* (1), 29–104. <https://doi.org/10.1007/s41918-018-0024-x>.
- (75) Wu, H. B.; Lou, X. W. (David). Metal–Organic Frameworks and Their Derived Materials for Electrochemical Energy Storage and Conversion: Promises and Challenges. *Sci. Adv.* **2017**, *3* (12), eaap9252. <https://doi.org/10.1126/sciadv.aap9252>.
- (76) Naghdi, S.; Shahrestani, M. M.; Zendeabad, M.; Djahaniani, H.; Kazemian, H.; Eder, D. Recent Advances in Application of Metal–Organic Frameworks (MOFs) as Adsorbent and Catalyst in Removal of Persistent Organic Pollutants (POPs). *J. Hazard. Mater.* **2023**, *442*, 130127. <https://doi.org/10.1016/j.jhazmat.2022.130127>.
- (77) *Recent advances in MOF-based photocatalysis: environmental remediation under visible light - Inorganic Chemistry Frontiers (RSC Publishing) DOI:10.1039/C9QI01120J.* <https://pubs.rsc.org/en/content/articlehtml/2020/qi/c9qi01120j> (accessed 2023-12-21).
- (78) Liu, X.; Wang, A.; Wang, C.; Li, J.; Zhang, Z.; Al-Enizi, A. M.; Nafady, A.; Shui, F.; You, Z.; Li, B.; Wen, Y.; Ma, S. A General Large-Scale Synthesis Approach for Crystalline Porous Materials. *Nat. Commun.* **2023**, *14* (1), 7022. <https://doi.org/10.1038/s41467-023-42833-y>.
- (79) Li, N.; Xu, J.; Feng, R.; Hu, T.-L.; Bu, X.-H. Governing Metal–Organic Frameworks towards High Stability. *Chem. Commun.* **2016**, *52* (55), 8501–8513. <https://doi.org/10.1039/C6CC02931K>.
- (80) Li, Y.; Karimi, M.; Gong, Y.-N.; Dai, N.; Safarifard, V.; Jiang, H.-L. Integration of Metal–Organic Frameworks and Covalent Organic Frameworks: Design, Synthesis, and Applications. *Matter* **2021**, *4* (7), 2230–2265. <https://doi.org/10.1016/j.matt.2021.03.022>.
- (81) Stassen, I.; Burtch, N.; Talin, A.; Falcaro, P.; Allendorf, M.; Ameloot, R. An Updated Roadmap for the Integration of Metal–Organic Frameworks with Electronic Devices and Chemical Sensors. *Chem. Soc. Rev.* **2017**, *46* (11), 3185–3241. <https://doi.org/10.1039/C7CS00122C>.

- (82) Liu, B.; Ma, M.; Zacher, D.; Bétard, A.; Yussenko, K.; Metzler-Nolte, N.; Wöll, C.; Fischer, R. A. Chemistry of SURMOFs: Layer-Selective Installation of Functional Groups and Post-Synthetic Covalent Modification Probed by Fluorescence Microscopy. *J. Am. Chem. Soc.* **2011**, *133* (6), 1734–1737. <https://doi.org/10.1021/ja1109826>.
- (83) McGuire, C. V.; Forgan, R. S. The Surface Chemistry of Metal–Organic Frameworks. *Chem. Commun.* **2015**, *51* (25), 5199–5217. <https://doi.org/10.1039/C4CC04458D>.
- (84) Wu, T.; Liu, X.; Liu, Y.; Cheng, M.; Liu, Z.; Zeng, G.; Shao, B.; Liang, Q.; Zhang, W.; He, Q.; Zhang, W. Application of QD-MOF Composites for Photocatalysis: Energy Production and Environmental Remediation. *Coord. Chem. Rev.* **2020**, *403*, 213097. <https://doi.org/10.1016/j.ccr.2019.213097>.
- (85) Keskin, S.; Alsoy Altinkaya, S. A Review on Computational Modeling Tools for MOF-Based Mixed Matrix Membranes. *Computation* **2019**, *7* (3), 36. <https://doi.org/10.3390/computation7030036>.
- (86) Meng, J.; Liu, X.; Niu, C.; Pang, Q.; Li 李坚涛, J.; Liu, F.; Liu, Z.; Mai, L. Advances in Metal-Organic Framework Coatings: Versatile Synthesis and Broad Applications. *Chem. Soc. Rev.* **2020**, *49*. <https://doi.org/10.1039/C9CS00806C>.
- (87) Yang, S.; Karve, V. V.; Justin, A.; Kochetygov, I.; Espín, J.; Asgari, M.; Trukhina, O.; Sun, D. T.; Peng, L.; Queen, W. L. Enhancing MOF Performance through the Introduction of Polymer Guests. *Coord. Chem. Rev.* **2021**, *427*, 213525. <https://doi.org/10.1016/j.ccr.2020.213525>.
- (88) Yu, K.; Lee, Y.-R.; Seo, J. Y.; Baek, K.-Y.; Chung, Y.-M.; Ahn, W.-S. Sonochemical Synthesis of Zr-Based Porphyrinic MOF-525 and MOF-545: Enhancement in Catalytic and Adsorption Properties. *Microporous Mesoporous Mater.* **2021**, *316*, 110985. <https://doi.org/10.1016/j.micromeso.2021.110985>.
- (89) Rubio-Martinez, M.; Avci-Camur, C.; W. Thornton, A.; Imaz, I.; Maspocho, D.; R. Hill, M. New Synthetic Routes towards MOF Production at Scale. *Chem. Soc. Rev.* **2017**, *46* (11), 3453–3480. <https://doi.org/10.1039/C7CS00109F>.
- (90) Julien, P. A.; Užarević, K.; Katsenis, A. D.; Kimber, S. A. J.; Wang, T.; Farha, O. K.; Zhang, Y.; Casaban, J.; Germann, L. S.; Etter, M.; Dinnebier, R. E.; James, S. L.; Halasz, I.; Friščić, T. In Situ Monitoring and Mechanism of the Mechanochemical Formation of a Microporous MOF-74 Framework. *J. Am. Chem. Soc.* **2016**, *138* (9), 2929–2932. <https://doi.org/10.1021/jacs.5b13038>.
- (91) Zahn, G.; Zerner, P.; Lippke, J.; L. Kempf, F.; Lilienthal, S.; A. Schröder, C.; M. Schneider, A.; Behrens, P. Insight into the Mechanism of Modulated Syntheses: In Situ Synchrotron Diffraction Studies on the Formation of Zr-Fumarate MOF. *CrystEngComm* **2014**, *16* (39), 9198–9207. <https://doi.org/10.1039/C4CE01095G>.
- (92) Wu, D.; Navrotsky, A. Thermodynamics of Metal-Organic Frameworks. *J. Solid State Chem.* **2015**, *223*, 53–58. <https://doi.org/10.1016/j.jssc.2014.06.015>.
- (93) Crivello, C.; Sevim, S.; Graniel, O.; Franco, C.; Pané, S.; Puigmartí-Luis, J.; Muñoz-Rojas, D. Advanced Technologies for the Fabrication of MOF Thin Films. *Mater. Horiz.* **2021**, *8* (1), 168–178. <https://doi.org/10.1039/D0MH00898B>.

- (94) John Cruz, A.; Arnauts, G.; Obst, M.; E. Kravchenko, D.; M. Vereecken, P.; Feyter, S. D.; Stassen, I.; Hauffman, T.; Ameloot, R. Effect of Different Oxide and Hybrid Precursors on MOF-CVD of ZIF-8 Films. *Dalton Trans.* **2021**, 50 (20), 6784–6788. <https://doi.org/10.1039/D1DT00927C>.
- (95) *Metal–organic frameworks (MOFs) beyond crystallinity: amorphous MOFs, MOF liquids and MOF glasses - Journal of Materials Chemistry A (RSC Publishing)* DOI:10.1039/D1TA01043C. <https://pubs.rsc.org/en/content/articlehtml/2001/mk/d1ta01043c> (accessed 2023-11-17).
- (96) Bennett, T. D.; Cheetham, A. K. Amorphous Metal–Organic Frameworks. *Acc. Chem. Res.* **2014**, 47 (5), 1555–1562. <https://doi.org/10.1021/ar5000314>.
- (97) Wu, X.; Yue, H.; Zhang, Y.; Gao, X.; Li, X.; Wang, L.; Cao, Y.; Hou, M.; An, H.; Zhang, L.; Li, S.; Ma, J.; Lin, H.; Fu, Y.; Gu, H.; Lou, W.; Wei, W.; Zare, R. N.; Ge, J. Packaging and Delivering Enzymes by Amorphous Metal–Organic Frameworks. *Nat. Commun.* **2019**, 10 (1), 5165. <https://doi.org/10.1038/s41467-019-13153-x>.
- (98) Fonseca, J.; Choi, S. Synthesis of a Novel Amorphous Metal Organic Framework with Hierarchical Porosity for Adsorptive Gas Separation. *Microporous Mesoporous Mater.* **2021**, 310, 110600. <https://doi.org/10.1016/j.micromeso.2020.110600>.
- (99) Ye, L.; Wang, J.; Zhang, Y.; Zhang, M.; Jing, X.; Gong, Y. A Self-Supporting Electrode with in-Situ Partial Transformation of Fe-MOF into Amorphous NiFe-LDH for Efficient Oxygen Evolution Reaction. *Appl. Surf. Sci.* **2021**, 556, 149781. <https://doi.org/10.1016/j.apsusc.2021.149781>.
- (100) Nasim, M.; Li, Y.; Wen, M.; Wen, C. A Review of High-Strength Nanolaminates and Evaluation of Their Properties. *J. Mater. Sci. Technol.* **2020**, 50, 215–244. <https://doi.org/10.1016/j.jmst.2020.03.011>.
- (101) Barbee, T. W. Nano-Laminates: A New Class of Materials for Aerospace Applications. In *2003 IEEE Aerospace Conference Proceedings (Cat. No.03TH8652)*; IEEE: Big Sky, Montana, USA, 2003; Vol. 4, p 4\_1745-4\_1754. <https://doi.org/10.1109/AERO.2003.1235105>.
- (102) Tseng, M.-H.; Su, D.-Y.; Chen, G.-L.; Tsai, F.-Y. Nano-Laminated Metal Oxides/Polyamide Stretchable Moisture- and Gas-Barrier Films by Integrated Atomic/Molecular Layer Deposition. *ACS Appl. Mater. Interfaces* **2021**, 13 (23), 27392–27399. <https://doi.org/10.1021/acsami.1c03895>.
- (103) Fu, L.; Xia, W. MAX Phases as Nanolaminate Materials: Chemical Composition, Microstructure, Synthesis, Properties, and Applications. *Adv. Eng. Mater.* **2021**, 23 (4), 2001191. <https://doi.org/10.1002/adem.202001191>.
- (104) Park, J. W.; Kwon, S.; Kwon, J. H.; Kim, C. Y.; Choi, K. C. Low-Leakage Fiber-Based Field-Effect Transistors with an Al<sub>2</sub>O<sub>3</sub>–MgO Nanolaminate as Gate Insulator. *ACS Appl. Electron. Mater.* **2019**, 1 (8), 1400–1407. <https://doi.org/10.1021/acsaelm.9b00189>.
- (105) *A review on hybrid nanolaminate materials synthesized by deposition techniques for energy storage applications - Journal of Materials Chemistry A (RSC Publishing)* DOI:10.1039/C3TA14034B. <https://pubs.rsc.org/en/content/articlehtml/2014/ta/c3ta14034b> (accessed 2023-12-28).
- (106) Nie, M.; Zhao, Y.; Nam, W.; Song, J.; Zhu, W.; Lezec, H. J.; Agrawal, A.; Zhou, W. Broadband Nanoscale Surface-Enhanced Raman Spectroscopy by Multiresonant Nanolaminate Plasmonic

Nanocavities on Vertical Nanopillars. *Adv. Funct. Mater.* **2022**, *32* (32), 2202231.  
<https://doi.org/10.1002/adfm.202202231>.

- (107) Kravchenko, Y. O.; Coy, E.; Załęski, K.; Iatsunskiy, I.; Pogorielov, M.; Korniienko, V.; Pshyk, A. V.; Pogrebnjak, A. D.; Beresnev, V. M. Biocompatibility and Electron Microscopy Studies of Epitaxial Nanolaminate (Al<sub>0.5</sub>Ti<sub>0.5</sub>)N/ZrN Coatings Deposited by Arc-PVD Technique. *Ceram. Int.* **2021**, *47* (24), 34648–34656. <https://doi.org/10.1016/j.ceramint.2021.09.003>.
- (108) Huang, J.; Mu, J.; Cho, Y.; Winter, C.; Wang, V.; Zhang, Z.; Wang, K.; Kim, C.; Yadav, A.; Wong, K.; Nemani, S.; Yieh, E.; Kummel, A. Low-k SiO<sub>x</sub>/AlO<sub>x</sub> Nanolaminate Dielectric on Dielectric Achieved by Hybrid Pulsed Chemical Vapor Deposition. *ACS Appl. Mater. Interfaces* **2023**, *15* (48), 56556–56566. <https://doi.org/10.1021/acsami.3c13973>.
- (109) Teixeira, V.; Monteiro, A.; Duarte, J.; Portinha, A. Deposition of Composite and Nanolaminate Ceramic Coatings by Sputtering. *Vacuum* **2002**, *67* (3), 477–483. [https://doi.org/10.1016/S0042-207X\(02\)00235-X](https://doi.org/10.1016/S0042-207X(02)00235-X).
- (110) Xing, L.-L.; Yuan, B.; Hu, S.-X.; Zhang, Y.-D.; Lu, Y.; Mai, Z.-H.; Li, M. Electrochemical Synthesis of Highly Oriented Layered Zinc Hydroxide with Intercalated P-Aminobenzoic Acid. *J. Phys. Chem. C* **2008**, *112* (10), 3800–3804. <https://doi.org/10.1021/jp709978v>.
- (111) Losego, M. D.; Blitz, I. P.; Vaia, R. A.; Cahill, D. G.; Braun, P. V. Ultralow Thermal Conductivity in Organoclay Nanolaminates Synthesized via Simple Self-Assembly. *Nano Lett.* **2013**, *13* (5), 2215–2219. <https://doi.org/10.1021/nl4007326>.
- (112) Xie, T.; Fu, L.; Qin, W.; Zhu, J.; Yang, W.; Li, D.; Zhou, L. Self-Assembled Metal Nano-Multilayered Film Prepared by Co-Sputtering Method. *Appl. Surf. Sci.* **2018**, *435*, 16–22. <https://doi.org/10.1016/j.apsusc.2017.11.049>.
- (113) Flores-López, M. L.; Cerqueira, M. A.; de Rodríguez, D. J.; Vicente, A. A. Perspectives on Utilization of Edible Coatings and Nano-Laminate Coatings for Extension of Postharvest Storage of Fruits and Vegetables. *Food Eng. Rev.* **2016**, *8* (3), 292–305. <https://doi.org/10.1007/s12393-015-9135-x>.
- (114) Choi, J.-H.; Kim, Y.-M.; Park, Y.-W.; Park, T.-H.; Jeong, J.-W.; Choi, H.-J.; Song, E.-H.; Lee, J.-W.; Kim, C.-H.; Ju, B.-K. Highly Conformal SiO<sub>2</sub>/Al<sub>2</sub>O<sub>3</sub> Nanolaminate Gas-Diffusion Barriers for Large-Area Flexible Electronics Applications. *Nanotechnology* **2010**, *21* (47), 475203. <https://doi.org/10.1088/0957-4484/21/47/475203>.
- (115) Veiga, C.; Davim, J. P.; Loureiro, A. J. R. PROPERTIES AND APPLICATIONS OF TITANIUM ALLOYS: A BRIEF REVIEW.
- (116) Liu, S.; Shin, Y. C. Additive Manufacturing of Ti6Al4V Alloy: A Review. *Mater. Des.* **2019**, *164*, 107552. <https://doi.org/10.1016/j.matdes.2018.107552>.
- (117) Kim, K. T.; Eo, M. Y.; Nguyen, T. T. H.; Kim, S. M. General Review of Titanium Toxicity. *Int. J. Implant Dent.* **2019**, *5* (1), 10. <https://doi.org/10.1186/s40729-019-0162-x>.
- (118) Monteiro, E. dos S.; Moura de Souza Soares, F.; Nunes, L. F.; Carvalho Santana, A. I.; Sérgio de Biasi, R.; Elias, C. N. Comparison of the Wettability and Corrosion Resistance of Two Biomedical Ti

Alloys Free of Toxic Elements with Those of the Commercial ASTM F136 (Ti–6Al–4V) Alloy. *J. Mater. Res. Technol.* **2020**, *9* (6), 16329–16338. <https://doi.org/10.1016/j.jmrt.2020.11.068>.

(119) Satoh, K.; Ohtsu, N.; Sato, S.; Wagatsuma, K. Surface Modification of Ti–6Al–4V Alloy Using an Oxygen Glow-Discharge Plasma to Suppress the Elution of Toxic Elements into Physiological Environment. *Surf. Coat. Technol.* **2013**, *232*, 298–302. <https://doi.org/10.1016/j.surfcoat.2013.05.018>.

(120) Pyka, G.; Burakowski, A.; Kerckhofs, G.; Moesen, M.; Van Bael, S.; Schrooten, J.; Wevers, M. Surface Modification of Ti6Al4V Open Porous Structures Produced by Additive Manufacturing. *Adv. Eng. Mater.* **2012**, *14* (6), 363–370. <https://doi.org/10.1002/adem.201100344>.

(121) Zhang, L.-C.; Chen, L.-Y.; Wang, L. Surface Modification of Titanium and Titanium Alloys: Technologies, Developments, and Future Interests. *Adv. Eng. Mater.* **2020**, *22* (5), 1901258. <https://doi.org/10.1002/adem.201901258>.

(122) Alén, P.; Vehkamäki, M.; Ritala, M.; Leskelä, M. Diffusion Barrier Properties of Atomic Layer Deposited Ultrathin Ta[Sub 2]O[Sub 5] and TiO[Sub 2] Films. *J. Electrochem. Soc.* **2006**, *153* (4), G304. <https://doi.org/10.1149/1.2168389>.

(123) Kaindl, R.; Homola, T.; Rastelli, A.; Schwarz, A.; Tarre, A.; Kopp, D.; Coclite, A. M.; Görtler, M.; Meier, B.; Pretenthaler, B.; Belegriatis, M.; Lackner, J. M.; Waldhauser, W. Atomic Layer Deposition of Oxide Coatings on Porous Metal and Polymer Structures Fabricated by Additive Manufacturing Methods (Laser-Based Powder Bed Fusion, Material Extrusion, Material Jetting). *Surf. Interfaces* **2022**, *34*, 102361. <https://doi.org/10.1016/j.surfin.2022.102361>.

(124) Li, F.; Lan, X.; Wang, L.; Kong, X.; Xu, P.; Tai, Y.; Liu, G.; Shi, J. An Efficient Photocatalyst Coating Strategy for Intimately Coupled Photocatalysis and Biodegradation (ICPB): Powder Spraying Method. *Chem. Eng. J.* **2020**, *383*, 123092. <https://doi.org/10.1016/j.cej.2019.123092>.

(125) *Coatings | Free Full-Text | Review on the Photocatalyst Coatings of TiO<sub>2</sub>: Fabrication by Mechanical Coating Technique and Its Application.* <https://www.mdpi.com/2079-6412/5/3/425> (accessed 2023-12-29).

(126) Adhikari, S.; Selvaraj, S.; Kim, D.-H. Progress in Powder Coating Technology Using Atomic Layer Deposition. *Adv. Mater. Interfaces* **2018**, *5* (16), 1800581. <https://doi.org/10.1002/admi.201800581>.

(127) Thouless, M. D. Cracking and Delamination of Coatings. *J. Vac. Sci. Technol. Vac. Surf. Films* **1991**, *9* (4), 2510–2515. <https://doi.org/10.1116/1.577265>.

(128) Guttoff, E. B.; Cohen, E. D. 14 - Water- and Solvent-Based Coating Technology. In *Multilayer Flexible Packaging (Second Edition)*; Wagner, J. R., Ed.; Plastics Design Library; William Andrew Publishing, 2016; pp 205–234. <https://doi.org/10.1016/B978-0-323-37100-1.00014-4>.

(129) Furukawa, H.; Cordova, K. E.; O’Keeffe, M.; Yaghi, O. M. The Chemistry and Applications of Metal-Organic Frameworks. *Science* **2013**, *341* (6149), 1230444.

(130) Shi, Y.; Yang, A.-F.; Cao, C.-S.; Zhao, B. Applications of MOFs: Recent Advances in Photocatalytic Hydrogen Production from Water. *Coord. Chem. Rev.* **2019**, *390*, 50–75.

- (131) Wang, J.; Cherevan, A. S.; Hannecart, C.; Naghdi, S.; Nandan, S. P.; Gupta, T.; Eder, D. Ti-Based MOFs: New Insights on the Impact of Ligand Composition and Hole Scavengers on Stability, Charge Separation and Photocatalytic Hydrogen Evolution. *Appl. Catal. B Environ.* **2021**, *283*, 119626. <https://doi.org/10.1016/j.apcatb.2020.119626>.
- (132) Abid, H. R.; Tian, H.; Ang, H.-M.; Tade, M. O.; Buckley, C. E.; Wang, S. Nanosize Zr-Metal Organic Framework (UiO-66) for Hydrogen and Carbon Dioxide Storage. *Chem. Eng. J.* **2012**, *187*, 415–420. <https://doi.org/10.1016/j.cej.2012.01.104>.
- (133) Liu, X.; Demir, N. K.; Wu, Z.; Li, K. Highly Water-Stable Zirconium Metal–Organic Framework UiO-66 Membranes Supported on Alumina Hollow Fibers for Desalination. *J. Am. Chem. Soc.* **2015**, *137* (22), 6999–7002. <https://doi.org/10.1021/jacs.5b02276>.
- (134) Zhang, D.-L.; Feng, Q.-K.; Zhong, S.-L.; Liu, D.-F.; Zhao, Y.; Dang, Z.-M. Tunable Dielectric Performance of Porphyrin Based Metal–organic Frameworks with Polar Molecule Confinement. *Compos. Commun.* **2021**, *25*, 100734. <https://doi.org/10.1016/j.coco.2021.100734>.
- (135) Krishtab, M.; Stassen, I.; Stassin, T.; Cruz, A. J.; Okudur, O. O.; Armini, S.; Wilson, C.; De Gendt, S.; Ameloot, R. Vapor-Deposited Zeolitic Imidazolate Frameworks as Gap-Filling Ultra-Low-k Dielectrics. *Nat. Commun.* **2019**, *10* (1), 1–9.
- (136) Fonseca, J.; Gong, T.; Jiao, L.; Jiang, H.-L. Metal–Organic Frameworks (MOFs) beyond Crystallinity: Amorphous MOFs, MOF Liquids and MOF Glasses. *J. Mater. Chem. A* **2021**, *9* (17), 10562–10611.
- (137) Ma, N.; Horike, S. Metal–Organic Network-Forming Glasses. *Chem. Rev.* **2022**, *122* (3), 4163–4203.
- (138) Liu, C.; Wang, J.; Wan, J.; Cheng, Y.; Huang, R.; Zhang, C.; Hu, W.; Wei, G.; Yu, C. Amorphous Metal–Organic Framework-Dominated Nanocomposites with Both Compositional and Structural Heterogeneity for Oxygen Evolution. *Angew. Chem.* **2020**, *132* (9), 3659–3666.
- (139) Li, L.; Li, G.; Zhang, Y.; Ouyang, W.; Zhang, H.; Dong, F.; Gao, X.; Lin, Z. Fabricating Nano-IrO<sub>2</sub>@ Amorphous Ir-MOF Composites for Efficient Overall Water Splitting: A One-Pot Solvothermal Approach. *J. Mater. Chem. A* **2020**, *8* (48), 25687–25695.
- (140) Laulainen, J. E. M.; Johnstone, D. N.; Bogachev, I.; Longley, L.; Calahoo, C.; Wondraczek, L.; Keen, D. A.; Bennett, T. D.; Collins, S. M.; Midgley, P. A. Mapping Short-Range Order at the Nanoscale in Metal–Organic Framework and Inorganic Glass Composites. *Nanoscale* **2022**, *14* (44), 16524–16535. <https://doi.org/10.1039/D2NR03791B>.
- (141) Shan, Y.; Chen, L.; Pang, H.; Xu, Q. Metal–Organic Framework-based Hybrid Frameworks. *Small Struct.* **2021**, *2* (2), 2000078.
- (142) Moniz, S. J.; Shevlin, S. A.; Martin, D. J.; Guo, Z.-X.; Tang, J. Visible-Light Driven Heterojunction Photocatalysts for Water Splitting—a Critical Review. *Energy Environ. Sci.* **2015**, *8* (3), 731–759.
- (143) Liu, J.; Wöll, C. Surface-Supported Metal–Organic Framework Thin Films: Fabrication Methods, Applications, and Challenges. *Chem. Soc. Rev.* **2017**, *46* (19), 5730–5770.

- (144) Stassen, I.; De Vos, D.; Ameloot, R. Vapor-Phase Deposition and Modification of Metal–Organic Frameworks: State-of-the-Art and Future Directions. *Chem. Eur. J.* **2016**, *22* (41), 14452–14460.
- (145) Stassen, I.; Styles, M.; Greci, G.; Van Gorp, H.; Vanderlinden, W.; De Feyter, S.; Falcaro, P.; De Vos, D.; Vereecken, P.; Ameloot, R. Chemical Vapour Deposition of Zeolitic Imidazolate Framework Thin Films. *Nat. Mater.* **2016**, *15* (3), 304–310.
- (146) Kräuter, M.; Cruz, A. J.; Stassin, T.; Rodríguez-Hermida, S.; Ameloot, R.; Resel, R.; Coclite, A. M. Influence of Precursor Density and Conversion Time on the Orientation of Vapor-Deposited ZIF-8. *Crystals* **2022**, *12* (2), 217.
- (147) Salmi, L. D.; Heikkilä, M. J.; Puukilainen, E.; Sajavaara, T.; Grosso, D.; Ritala, M. Studies on Atomic Layer Deposition of MOF-5 Thin Films. *Microporous Mesoporous Mater.* **2013**, *182*, 147–154.
- (148) Salmi, L. D.; Heikkilä, M. J.; Vehkamäki, M.; Puukilainen, E.; Ritala, M.; Sajavaara, T. Studies on Atomic Layer Deposition of IRMOF-8 Thin Films. *J. Vac. Sci. Technol. Vac. Surf. Films* **2015**, *33* (1), 01A121.
- (149) Lausund, K. B.; Petrovic, V.; Nilsen, O. All-Gas-Phase Synthesis of Amino-Functionalized UiO-66 Thin Films. *Dalton Trans.* **2017**, *46* (48), 16983–16992.
- (150) Lausund, K. B.; Olsen, M. S.; Hansen, P.-A.; Valen, H.; Nilsen, O. MOF Thin Films with Bi-Aromatic Linkers Grown by Molecular Layer Deposition. *J. Mater. Chem. A* **2020**, *8* (5), 2539–2548.
- (151) Ahvenniemi, E.; Karppinen, M. Atomic/Molecular Layer Deposition: A Direct Gas-Phase Route to Crystalline Metal–Organic Framework Thin Films. *Chem. Commun.* **2016**, *52* (6), 1139–1142.
- (152) Ahvenniemi, E.; Karppinen, M. ALD/MLD Processes for Mn and Co Based Hybrid Thin Films. *Dalton Trans.* **2016**, *45* (26), 10730–10735.
- (153) Tanskanen, A.; Karppinen, M. Iron-Terephthalate Coordination Network Thin Films through in-Situ Atomic/Molecular Layer Deposition. *Sci. Rep.* **2018**, *8* (1), 1–8.
- (154) Khayyami, A.; Philip, A.; Karppinen, M. Atomic/Molecular Layer Deposited Iron–Azobenzene Framework Thin Films for Stimuli-Induced Gas Molecule Capture/Release. *Angew. Chem. Int. Ed.* **2019**, *58* (38), 13400–13404.
- (155) Ghazy, A.; Safdar, M.; Lastusaari, M.; Karppinen, M. Amorphous-to-Crystalline Transition and Photoluminescence Switching in Guest-Absorbing Metal–Organic Network Thin Films. *Chem. Commun.* **2020**, *56* (2), 241–244.
- (156) Robertson, J. Properties of Diamond-like Carbon. *Surf. Coat. Technol.* **1992**, *50* (3), 185–203.
- (157) Li, F. M.; Bayer, B. C.; Hofmann, S.; Dutson, J. D.; Wakeham, S. J.; Thwaites, M. J.; Milne, W. I.; Flewitt, A. J. High-k (K= 30) Amorphous Hafnium Oxide Films from High Rate Room Temperature Deposition. *Appl. Phys. Lett.* **2011**, *98*, 252903.
- (158) Dan-Hardi, M.; Serre, C.; Frot, T.; Rozes, L.; Maurin, G.; Sanchez, C.; Férey, G. A New Photoactive Crystalline Highly Porous Titanium(IV) Dicarboxylate. *J. Am. Chem. Soc.* **2009**, *131* (31), 10857–10859. <https://doi.org/10.1021/ja903726m>.

- (159) Momma, K.; Izumi, F. VESTA 3 for Three-Dimensional Visualization of Crystal, Volumetric and Morphology Data. *J. Appl. Crystallogr.* **2011**, *44* (6), 1272–1276. <https://doi.org/10.1107/S0021889811038970>.
- (160) PubChem. *Hazardous Substances Data Bank (HSDB) : 870*. <https://pubchem.ncbi.nlm.nih.gov/source/hsdb/870> (accessed 2023-06-06).
- (161) Rahtu, A.; Ritala, M. Reaction Mechanism Studies on the Zirconium Chloride–Water Atomic Layer Deposition Process. *J. Mater. Chem.* **2002**, *12* (5), 1484–1489. <https://doi.org/10.1039/b109846b>.
- (162) Shevyakov, A. M.; Kuznetsova, G. N.; Aleskovskii, V. B. Interaction of Titanium and Germanium Tetrachlorides with Hydrated Silica. In *Chemistry of High-Temperature Materials*; Toropov, N. A., Ed.; Springer US: Boston, MA, 1969; pp 162–168. [https://doi.org/10.1007/978-1-4899-4824-3\\_31](https://doi.org/10.1007/978-1-4899-4824-3_31).
- (163) Adhikari, S.; Selvaraj, S.; Kim, D. Progress in Powder Coating Technology Using Atomic Layer Deposition. *Adv. Mater. Interfaces* **2018**, *5* (16), 1800581.
- (164) Bhembe, Y. A.; Dlamini, L. N. Photoreduction of Chromium (VI) by a Composite of Niobium (V) Oxide Impregnated with a Ti-Based MOF. *J. Environ. Sci. Health Part A* **2020**, *55* (8), 1003–1020. <https://doi.org/10.1080/10934529.2020.1763706>.
- (165) Li, Z.; Che, G.; Jiang, W.; Liu, L.; Wang, H. Visible-Light-Driven CQDs@MIL-125(Ti) Nanocomposite Photocatalyst with Enhanced Photocatalytic Activity for the Degradation of Tetracycline. *RSC Adv.* **2019**, *9* (57), 33238–33245. <https://doi.org/10.1039/C9RA05600A>.
- (166) Zhu, L.; Lu, Q.; Lv, L.; Wang, Y.; Hu, Y.; Deng, Z.; Lou, Z.; Hou, Y.; Teng, F. Ligand-Free Rutile and Anatase TiO<sub>2</sub> Nanocrystals as Electron Extraction Layers for High Performance Inverted Polymer Solar Cells. *RSC Adv.* **2017**, *7* (33), 20084–20092. <https://doi.org/10.1039/C7RA00134G>.
- (167) Yuan, X.; Wang, H.; Wu, Y.; Zeng, G.; Chen, X.; Leng, L.; Wu, Z.; Li, H. One-Pot Self-Assembly and Photoreduction Synthesis of Silver Nanoparticle-Decorated Reduced Graphene Oxide/MIL-125(Ti) Photocatalyst with Improved Visible Light Photocatalytic Activity: Synthesis of Ag/rGO/MIL-125(Ti) Photocatalyst for Photocatalysis. *Appl. Organomet. Chem.* **2016**, *30* (5), 289–296. <https://doi.org/10.1002/aoc.3430>.
- (168) Challagulla, S.; Tarafder, K.; Ganesan, R.; Roy, S. Structure Sensitive Photocatalytic Reduction of Nitroarenes over TiO<sub>2</sub>. *Sci. Rep.* **2017**, *7* (1), 8783. <https://doi.org/10.1038/s41598-017-08599-2>.
- (169) Pritchina, E. A.; Kolesov, B. A. Raman Spectra of Terephthalic Acid Crystals in the Temperature Range 5 K–300 K. *Spectrochim. Acta. A. Mol. Biomol. Spectrosc.* **2018**, *202*, 319–323. <https://doi.org/10.1016/j.saa.2018.05.065>.
- (170) Hlophe, P. V.; Mahlalela, L. C.; Dlamini, L. N. A Composite of Platelet-like Orientated BiVO<sub>4</sub> Fused with MIL-125(Ti): Synthesis and Characterization. *Sci. Rep.* **2019**, *9* (1), 10044. <https://doi.org/10.1038/s41598-019-46498-w>.
- (171) Qiao, X.; Liu, Y.; Yang, Y.; Wang, H.; Ma, J.; Wang, D.; Gao, N.; Li, L.; Liu, W.; Wang, H. Synthesis Optimization of Metal-Organic Frameworks MIL-125 and Its Adsorption Separation on C8

Aromatics Measured by Pulse Test and Simulation Calculation. *J. Solid State Chem.* **2021**, *296*, 121956. <https://doi.org/10.1016/j.jssc.2021.121956>.

(172) Bayer, B. C.; Bosworth, D. A.; Michaelis, F. B.; Blume, R.; Habler, G.; Abart, R.; Weatherup, R. S.; Kidambi, P. R.; Baumberg, J. J.; Knop-Gericke, A.; Schloegl, R.; Baetz, C.; Barber, Z. H.; Meyer, J. C.; Hofmann, S. In Situ Observations of Phase Transitions in Metastable Nickel (Carbide)/Carbon Nanocomposites. *J. Phys. Chem. C* **2016**, *120* (39), 22571–22584. <https://doi.org/10.1021/acs.jpcc.6b01555>.

(173) Decker, G. E.; Bloch, E. D. Using Helium Pycnometry to Study the Apparent Densities of Metal–Organic Frameworks. *ACS Appl. Mater. Interfaces* **2021**, *13* (44), 51925–51932. <https://doi.org/10.1021/acsami.1c07304>.

(174) Krivanek, O. L.; Chisholm, M. F.; Nicolosi, V.; Pennycook, T. J.; Corbin, G. J.; Dellby, N.; Murfitt, M. F.; Own, C. S.; Szilagy, Z. S.; Oxley, M. P.; Pantelides, S. T.; Pennycook, S. J. Atom-by-Atom Structural and Chemical Analysis by Annular Dark-Field Electron Microscopy. *Nature* **2010**, *464* (7288), 571–574.

(175) Multia, J.; Kravchenko, D. E.; Rubio-Giménez, V.; Philip, A.; Ameloot, R.; Karppinen, M. Nanoporous Metal–Organic Framework Thin Films Prepared Directly from Gaseous Precursors by Atomic and Molecular Layer Deposition: Implications for Microelectronics. *ACS Appl. Nano Mater.* **2023**.

(176) Aarik, J.; Aidla, A.; Mändar, H.; Uustare, T. Atomic Layer Deposition of Titanium Dioxide from TiCl<sub>4</sub> and H<sub>2</sub>O: Investigation of Growth Mechanism. *Appl. Surf. Sci.* **2001**, *172* (1–2), 148–158. [https://doi.org/10.1016/S0169-4332\(00\)00842-4](https://doi.org/10.1016/S0169-4332(00)00842-4).

(177) Haselmann, G. M.; Eder, D. Early-Stage Deactivation of Platinum-Loaded TiO<sub>2</sub> Using in Situ Photodeposition during Photocatalytic Hydrogen Evolution. *ACS Catal.* **2017**, *7* (7), 4668–4675.

(178) Stöber, W.; Fink, A.; Bohn, E. Controlled Growth of Monodisperse Silica Spheres in the Micron Size Range. *J. Colloid Interface Sci.* **1968**, *26* (1), 62–69. [https://doi.org/10.1016/0021-9797\(68\)90272-5](https://doi.org/10.1016/0021-9797(68)90272-5).

(179) Dubey, R. S.; Rajesh, Y. B. R. D.; More, M. A. Synthesis and Characterization of SiO<sub>2</sub> Nanoparticles via Sol-Gel Method for Industrial Applications. *Mater. Today Proc.* **2015**, *2* (4–5), 3575–3579. <https://doi.org/10.1016/j.matpr.2015.07.098>.

(180) Nelson, A. R. J.; Prescott, S. W. *Refnx* : Neutron and X-Ray Reflectometry Analysis in Python. *J. Appl. Crystallogr.* **2019**, *52* (1), 193–200. <https://doi.org/10.1107/S1600576718017296>.

(181) Gupta, T.; Rosza, N.; Sauer, M.; Goetz, A.; Winzely, M.; Rath, J.; Naghdi, S.; Lechner, A.; Apaydin, D. H.; Cherevan, A.; Friedbacher, G.; Foelske, A.; Skoff, S. M.; Bayer, B. C.; Eder, D. Sonochemical Synthesis of Large Two-Dimensional Bi<sub>2</sub>O<sub>2</sub>CO<sub>3</sub> Nanosheets for Hydrogen Evolution in Photocatalytic Water Splitting. *Adv. Sustain. Syst.* **2022**, *6* (11), 2100326. <https://doi.org/10.1002/advs.202100326>.

(182) Ayala, P.; Naghdi, S.; Nandan, S. P.; Myakala, S. N.; Rath, J.; Saito, H.; Guggenberger, P.; Lakhani, L.; Kleitz, F.; Toroker, M. C.; Cherevan, A.; Eder, D. The Emergence of 2D Building Units in Metal-Organic Frameworks for Photocatalytic Hydrogen Evolution: A Case Study with COK-47. *Adv. Energy Mater.* **2023**, *13* (31), 2300961. <https://doi.org/10.1002/aenm.202300961>.

- (183) Hong-Cai “Joe” Zhou; Kitagawa, S. Metal–Organic Frameworks (MOFs). *Chem. Soc. Rev.* **2014**, *43* (16), 5415–5418. <https://doi.org/10.1039/C4CS90059F>.
- (184) James, S. L. Metal–Organic Frameworks. *Chem. Soc. Rev.* **2003**, *32* (5), 276–288. <https://doi.org/10.1039/B200393G>.
- (185) Della Rocca, J.; Liu, D.; Lin, W. Nanoscale Metal–Organic Frameworks for Biomedical Imaging and Drug Delivery. *Acc. Chem. Res.* **2011**, *44* (10), 957–968. <https://doi.org/10.1021/ar200028a>.
- (186) Keskin, S.; Kizilel, S. Biomedical Applications of Metal Organic Frameworks. *Ind. Eng. Chem. Res.* **2011**, *50* (4), 1799–1812. <https://doi.org/10.1021/ie101312k>.
- (187) Zhu, L.; Liu, X.-Q.; Jiang, H.-L.; Sun, L.-B. Metal–Organic Frameworks for Heterogeneous Basic Catalysis. *Chem. Rev.* **2017**, *117* (12), 8129–8176. <https://doi.org/10.1021/acs.chemrev.7b00091>.
- (188) Dhakshinamoorthy, A.; Li, Z.; Garcia, H. Catalysis and Photocatalysis by Metal Organic Frameworks. *Chem. Soc. Rev.* **2018**, *47* (22), 8134–8172. <https://doi.org/10.1039/C8CS00256H>.
- (189) Zagorodniy, K.; Seifert, G.; Hermann, H. Metal–Organic Frameworks as Promising Candidates for Future Ultralow-k Dielectrics. *Appl. Phys. Lett.* **2010**, *97* (25), 251905. <https://doi.org/10.1063/1.3529461>.
- (190) Krishtab, M.; Stassen, I.; Stassin, T.; Cruz, A. J.; Okudur, O. O.; Armini, S.; Wilson, C.; De Gendt, S.; Ameloot, R. Vapor-Deposited Zeolitic Imidazolate Frameworks as Gap-Filling Ultra-Low-k Dielectrics. *Nat. Commun.* **2019**, *10* (1), 3729. <https://doi.org/10.1038/s41467-019-11703-x>.
- (191) Mendiratta, S.; Usman, M.; Lu, K.-L. Expanding the Dimensions of Metal–Organic Framework Research towards Dielectrics. *Coord. Chem. Rev.* **2018**, *360*, 77–91. <https://doi.org/10.1016/j.ccr.2018.01.005>.
- (192) Usman, M.; Mendiratta, S.; Lu, K.-L. Metal–Organic Frameworks: New Interlayer Dielectric Materials. *ChemElectroChem* **2015**, *2* (6), 786–788. <https://doi.org/10.1002/celec.201402456>.
- (193) Yang, Z.; Ao, D.; Guo, X.; Nie, L.; Qiao, Z.; Zhong, C. Preparation and Characterization of Small-Size Amorphous MOF Mixed Matrix Membrane. *Sep. Purif. Technol.* **2021**, *272*, 118860. <https://doi.org/10.1016/j.seppur.2021.118860>.
- (194) Niu, W.; Yang, Y. Amorphous MOF Introduced N-Doped Graphene: An Efficient and Versatile Electrocatalyst for Zinc–Air Battery and Water Splitting. *ACS Appl. Energy Mater.* **2018**, *1* (6), 2440–2445. <https://doi.org/10.1021/acsaem.8b00594>.
- (195) Shaiful Bahari, A. M.; Othman, S. Z.; Mohamad Fadli, M. F.; Zulkifli, M. Z. A.; Biyamin, S. A.; Islam, M. A.; Aspanut, Z.; Amin, N.; Misran, H. Facile Synthesis of Zr-Based Metal–Organic Gel (Zr-MOG) Using “Green” Sol-Gel Approach. *Surf. Interfaces* **2021**, *27*, 101469. <https://doi.org/10.1016/j.surfin.2021.101469>.
- (196) Hou, J.; F. Sapnik, A.; D. Bennett, T. Metal–Organic Framework Gels and Monoliths. *Chem. Sci.* **2020**, *11* (2), 310–323. <https://doi.org/10.1039/C9SC04961D>.
- (197) Prabhu, S. M.; Kancharla, S.; Min Park, C.; Sasaki, K. Synthesis of Modulator-Driven Highly Stable Zirconium-Fumarate Frameworks and Mechanistic Investigations of Their Arsenite and

Arsenate Adsorption from Aqueous Solutions. *CrystEngComm* **2019**, *21* (14), 2320–2332.  
<https://doi.org/10.1039/C8CE01424H>.

(198) Bennett, T. D.; Yue, Y.; Li, P.; Qiao, A.; Tao, H.; Greaves, N. G.; Richards, T.; Lampronti, G. I.; Redfern, S. A. T.; Blanc, F.; Farha, O. K.; Hupp, J. T.; Cheetham, A. K.; Keen, D. A. Melt-Quenched Glasses of Metal–Organic Frameworks. *J. Am. Chem. Soc.* **2016**, *138* (10), 3484–3492.  
<https://doi.org/10.1021/jacs.5b13220>.

(199) Bennett, T. D.; Horike, S. Liquid, Glass and Amorphous Solid States of Coordination Polymers and Metal–Organic Frameworks. *Nat. Rev. Mater.* **2018**, *3* (11), 431–440.  
<https://doi.org/10.1038/s41578-018-0054-3>.

(200) Ghazy, A.; Safdar, M.; Lastusaari, M.; Karppinen, M. Amorphous-to-Crystalline Transition and Photoluminescence Switching in Guest-Absorbing Metal–Organic Network Thin Films. *Chem. Commun.* **2020**, *56* (2), 241–244. <https://doi.org/10.1039/C9CC08904G>.

(201) Ashworth, C. Characterizing Amorphous MOFs. *Nat. Rev. Chem.* **2021**, *5* (5), 298–298.  
<https://doi.org/10.1038/s41570-021-00282-5>.

(202) Fillery, S. P.; Koerner, H.; Drummy, L.; Dunkerley, E.; Durstock, M. F.; Schmidt, D. F.; Vaia, R. A. Nanolaminates: Increasing Dielectric Breakdown Strength of Composites. *ACS Appl. Mater. Interfaces* **2012**, *4* (3), 1388–1396. <https://doi.org/10.1021/am201650g>.

(203) Kukli, K.; Ihanus, J.; Ritala, M.; Leskela, M. Tailoring the Dielectric Properties of HfO<sub>2</sub>–Ta<sub>2</sub>O<sub>5</sub> Nanolaminates. *Appl. Phys. Lett.* **1996**, *68* (26), 3737–3739. <https://doi.org/10.1063/1.115990>.

(204) Barsoum, M. W. The MN+1AXN Phases: A New Class of Solids: Thermodynamically Stable Nanolaminates. *Prog. Solid State Chem.* **2000**, *28* (1), 201–281. [https://doi.org/10.1016/S0079-6786\(00\)00006-6](https://doi.org/10.1016/S0079-6786(00)00006-6).

(205) Sagade, A. A.; Aria, A. I.; Edge, S.; Melgari, P.; Gieseking, B.; Bayer, B. C.; Meyer, J. C.; Bird, D.; Brewer, P.; Hofmann, S. Graphene-Based Nanolaminates as Ultra-High Permeation Barriers. *Npj 2D Mater. Appl.* **2017**, *1* (1), 1–8. <https://doi.org/10.1038/s41699-017-0037-z>.

(206) Kahouli, A.; Lebedev, O.; Ben Elbahri, M.; Mercey, B.; Prellier, W.; Riedel, S.; Czernohorsky, M.; Lallemand, F.; Bunel, C.; Lüders, U. Structural and Dielectric Properties of Subnanometric Laminates of Binary Oxides. *ACS Appl. Mater. Interfaces* **2015**, *7* (46), 25679–25684.  
<https://doi.org/10.1021/acsami.5b06485>.

(207) Rodríguez-Ortiz, A.; Muriel-Plaza, I.; Alía-García, C.; Pinilla-Cea, P.; Suárez-Bermejo, J. C. Hybrid Composite Material Reinforced with Carbon Nanolaminates for Gradient Stiffness: Preparation and Characterization. *Polymers* **2021**, *13* (22), 4043.  
<https://doi.org/10.3390/polym13224043>.

(208) Guo, W.; Pei, Z.; Sang, X.; Poplawsky, J. D.; Bruschi, S.; Qu, J.; Raabe, D.; Bei, H. Shape-Preserving Machining Produces Gradient Nanolaminate Medium Entropy Alloys with High Strain Hardening Capability. *Acta Mater.* **2019**, *170*, 176–186.  
<https://doi.org/10.1016/j.actamat.2019.03.024>.

- (209) Rahmani, A.; Emrooz, H. B. M.; Abedi, S.; Morsali, A. Synthesis and Characterization of CdS/MIL-125 (Ti) as a Photocatalyst for Water Splitting. *Mater. Sci. Semicond. Process.* **2018**, *80*, 44–51. <https://doi.org/10.1016/j.mssp.2018.02.013>.
- (210) Shamiryani, D.; Abell, T.; Iacopi, F.; Maex, K. Low-k Dielectric Materials. *Mater. Today* **2004**, *7* (1), 34–39. [https://doi.org/10.1016/S1369-7021\(04\)00053-7](https://doi.org/10.1016/S1369-7021(04)00053-7).
- (211) Guo, H.; Wang, M.; Liu, J.; Zhu, S.; Liu, C. Facile Synthesis of Nanoscale High Porosity IR-MOFs for Low-k Dielectrics Thin Films. *Microporous Mesoporous Mater.* **2016**, *221*, 40–47. <https://doi.org/10.1016/j.micromeso.2015.09.026>.
- (212) Grill, A.; Gates, S. M.; Ryan, T. E.; Nguyen, S. V.; Priyadarshini, D. Progress in the Development and Understanding of Advanced Low k and Ultralow k Dielectrics for Very Large-Scale Integrated Interconnects—State of the Art. *Appl. Phys. Rev.* **2014**, *1* (1), 011306. <https://doi.org/10.1063/1.4861876>.
- (213) Palumbo, F.; Wen, C.; Lombardo, S.; Pazos, S.; Aguirre, F.; Eizenberg, M.; Hui, F.; Lanza, M. A Review on Dielectric Breakdown in Thin Dielectrics: Silicon Dioxide, High-k, and Layered Dielectrics. *Adv. Funct. Mater.* **2020**, *30* (18), 1900657. <https://doi.org/10.1002/adfm.201900657>.
- (214) Evans, A. M.; Giri, A.; Sangwan, V. K.; Xun, S.; Bartnof, M.; Torres-Castanedo, C. G.; Balch, H. B.; Rahn, M. S.; Bradshaw, N. P.; Vitaku, E.; Burke, D. W.; Li, H.; Bedzyk, M. J.; Wang, F.; Brédas, J.-L.; Malen, J. A.; McGaughey, A. J. H.; Hersam, M. C.; Dichtel, W. R.; Hopkins, P. E. Thermally Conductive Ultra-Low-k Dielectric Layers Based on Two-Dimensional Covalent Organic Frameworks. *Nat. Mater.* **2021**, *20* (8), 1142–1148. <https://doi.org/10.1038/s41563-021-00934-3>.
- (215) Peng, J.; Pu, W.; Lu, S.; Yang, X.; Wu, C.; Wu, N.; Sun, Z.; Wang, H.-T. Inorganic Low k Cage-Molecular Crystals. *Nano Lett.* **2021**, *21* (1), 203–208. <https://doi.org/10.1021/acs.nanolett.0c03528>.
- (216) Cho, S.-J.; Bae, I.-S.; Park, Y. S.; Hong, B.; Park, W.; Park, S. C.; Boo, J.-H. The Characteristics of Organic–Inorganic Hybrid Low-k Thin Films by PECVD. *Surf. Coat. Technol.* **2008**, *202* (22), 5654–5658. <https://doi.org/10.1016/j.surfcoat.2008.06.105>.
- (217) Devaraju, S.; R. Vengatesan, M.; Selvi, M.; Ashok Kumar, A.; Hamerton, I.; S. Go, J.; Alagar, M. Low Surface Free Energy Cyanate Ester – Silica Hybrid (CE–SiO<sub>2</sub>) Nanomaterials for Low k Dielectric Applications. *RSC Adv.* **2013**, *3* (31), 12915–12921. <https://doi.org/10.1039/C3RA41144C>.
- (218) Xie, M.; Li, M.; Sun, Q.; Fan, W.; Xia, S.; Fu, W. Research Progress on Porous Low Dielectric Constant Materials. *Mater. Sci. Semicond. Process.* **2022**, *139*, 106320. <https://doi.org/10.1016/j.mssp.2021.106320>.
- (219) Øien, S.; Wragg, D.; Reinsch, H.; Svelle, S.; Bordiga, S.; Lamberti, C.; Lillerud, K. P. Detailed Structure Analysis of Atomic Positions and Defects in Zirconium Metal–Organic Frameworks. *Cryst. Growth Des.* **2014**, *14* (11), 5370–5372. <https://doi.org/10.1021/cg501386j>.
- (220) Luchinskii, G. P. Physico-Chemical Study of Titanium Halides. 1. Parameters of Phase Transitions of Titanium Tetrachloride. *Zh. Fiz. Khim.* **1966**, *40*, 593–598.
- (221) Matuszek, K.; Pankalla, E.; Grymel, A.; Latos, P.; Chrobok, A. Studies on the Solubility of Terephthalic Acid in Ionic Liquids. *Molecules* **2019**, *25* (1), 80. <https://doi.org/10.3390/molecules25010080>.

- (222) Sun, L.; Zhao, Y.; Shang, Y.; Sun, C.; Zhou, M. The Phase Stability of Terephthalic Acid under High Pressure. *Chem. Phys. Lett.* **2017**, *689*, 56–61. <https://doi.org/10.1016/j.cplett.2017.10.004>.
- (223) Maschio, L.; Kirtman, B.; Rérat, M.; Orlando, R.; Dovesi, R. Ab Initio Analytical Raman Intensities for Periodic Systems through a Coupled Perturbed Hartree-Fock/Kohn-Sham Method in an Atomic Orbital Basis. II. Validation and Comparison with Experiments. *J. Chem. Phys.* **2013**, *139*, 164102. <https://doi.org/10.1063/1.4824443>.
- (224) Robertson, J. Diamond-like Carbon. *Pure Appl. Chem.* **1994**, *66* (9), 1789–1796. <https://doi.org/10.1351/pac199466091789>.
- (225) Stöber, W.; Fink, A.; Bohn, E. Controlled Growth of Monodisperse Silica Spheres in the Micron Size Range. *J. Colloid Interface Sci.* **1968**, *26* (1), 62–69. [https://doi.org/10.1016/0021-9797\(68\)90272-5](https://doi.org/10.1016/0021-9797(68)90272-5).
- (226) Tougaard, S. Universality Classes of Inelastic Electron Scattering Cross-Sections. *Surf. Interface Anal.* **1997**, *25* (3), 137–154. [https://doi.org/10.1002/\(SICI\)1096-9918\(199703\)25:3<137::AID-SIA230>3.0.CO;2-L](https://doi.org/10.1002/(SICI)1096-9918(199703)25:3<137::AID-SIA230>3.0.CO;2-L).
- (227) Scofield, J. H. Hartree-Slater Subshell Photoionization Cross-Sections at 1254 and 1487 eV. *J. Electron Spectrosc. Relat. Phenom.* **1976**, *8* (2), 129–137. [https://doi.org/10.1016/0368-2048\(76\)80015-1](https://doi.org/10.1016/0368-2048(76)80015-1).
- (228) Powell, C. X-Ray Photoelectron Spectroscopy Database XPS, Version 4.1, NIST Standard Reference Database 20, 1989. <https://doi.org/10.18434/T4T88K>.
- (229) High Resolution XPS of Organic Polymers: The Scienta ESCA300 Database (Beamson, G.; Briggs, D.). *J. Chem. Educ.* **1993**, *70* (1), A25. <https://doi.org/10.1021/ed070pA25.5>.
- (230) Batool, S. A.; Ahmad, A.; Wadood, A.; Mateen, A.; Hussain, S. W. Development of Lightweight Aluminum-Titanium Alloys for Aerospace Applications. *Key Eng. Mater.* **2018**, *778*, 22–27. <https://doi.org/10.4028/www.scientific.net/KEM.778.22>.
- (231) Dada, M.; Popoola, P.; Adeosun, S.; Mathe, N. High Entropy Alloys for Aerospace Applications. In *Aerodynamics*; IntechOpen, 2019.
- (232) Cole, G. S.; Sherman, A. M. Light Weight Materials for Automotive Applications. *Mater. Charact.* **1995**, *35* (1), 3–9. [https://doi.org/10.1016/1044-5803\(95\)00063-1](https://doi.org/10.1016/1044-5803(95)00063-1).
- (233) Peters, M.; Kumpfert, J.; Ward, C. H.; Leyens, C. Titanium Alloys for Aerospace Applications. *Adv. Eng. Mater.* **2003**, *5* (6), 419–427. <https://doi.org/10.1002/adem.200310095>.
- (234) Hanawa, T. Metals and Medicine. *Mater. Trans.* **2021**, *62* (2), 139–148. <https://doi.org/10.2320/matertrans.MT-M2020268>.
- (235) Kiradzhyska, D. D.; Mantcheva, R. D. Overview of Biocompatible Materials and Their Use in Medicine. *Folia Med. (Plovdiv)* **2019**, *61* (1), 34–40. <https://doi.org/10.2478/folmed-2018-0038>.
- (236) Arrazola, P.-J.; Garay, A.; Iriarte, L.-M.; Armendia, M.; Marya, S.; Le Maître, F. Machinability of Titanium Alloys (Ti6Al4V and Ti555.3). *J. Mater. Process. Technol.* **2009**, *209* (5), 2223–2230. <https://doi.org/10.1016/j.jmatprotec.2008.06.020>.

- (237) Elanchezhian, C.; Vijaya Ramnath, B.; Ramakrishnan, G.; Sripada Raghavendra, K. N.; Muralidharan, M.; Kishore, V. Review on Metal Matrix Composites for Marine Applications. *Mater. Today Proc.* **2018**, *5* (1), 1211–1218. <https://doi.org/10.1016/j.matpr.2017.11.203>.
- (238) Timercan, A.; Brailovski, V.; Petit, Y.; Lussier, B.; Séguin, B. Personalized 3D-Printed Endoprostheses for Limb Sparing in Dogs: Modeling and in Vitro Testing. *Med. Eng. Phys.* **2019**, *71*, 17–29. <https://doi.org/10.1016/j.medengphy.2019.07.005>.
- (239) Elsayed, M.; Ghazy, M.; Youssef, Y.; Essa, K. Optimization of SLM Process Parameters for Ti6Al4V Medical Implants. *Rapid Prototyp. J.* **2019**, *25* (3), 433–447. <https://doi.org/10.1108/RPJ-05-2018-0112>.
- (240) Zhu, Y.; Zhang, K.; Meng, Z.; Zhang, K.; Hodgson, P.; Birbilis, N.; Weyland, M.; Fraser, H. L.; Lim, S. C. V.; Peng, H.; Yang, R.; Wang, H.; Huang, A. Ultrastrong Nanotwinned Titanium Alloys through Additive Manufacturing. *Nat. Mater.* **2022**, *21* (11), 1258–1262. <https://doi.org/10.1038/s41563-022-01359-2>.
- (241) Geetha, M.; Singh, A. K.; Asokamani, R.; Gogia, A. K. Ti Based Biomaterials, the Ultimate Choice for Orthopaedic Implants – A Review. *Prog. Mater. Sci.* **2009**, *54* (3), 397–425. <https://doi.org/10.1016/j.pmatsci.2008.06.004>.
- (242) Rao, S.; Ushida, T.; Tateishi, T.; Okazaki, Y.; Asao, S. Effect of Ti, Al, and V Ions on the Relative Growth Rate of Fibroblasts (L929) and Osteoblasts (MC3T3-E1) Cells. *Biomed. Mater. Eng.* **1996**, *6* (2), 79–86. <https://doi.org/10.3233/BME-1996-6202>.
- (243) Ferguson, J. D.; Buechler, K. J.; Weimer, A. W.; George, S. M. SnO<sub>2</sub> Atomic Layer Deposition on ZrO<sub>2</sub> and Al Nanoparticles: Pathway to Enhanced Thermite Materials. *Powder Technol.* **2005**, *156* (2–3), 154–163. <https://doi.org/10.1016/j.powtec.2005.04.009>.
- (244) Johnson, R. W.; Hultqvist, A.; Bent, S. F. A Brief Review of Atomic Layer Deposition: From Fundamentals to Applications. *Mater. Today* **2014**, *17* (5), 236–246. <https://doi.org/10.1016/j.mattod.2014.04.026>.
- (245) Hussin, R.; Choy, K. L.; Hou, X. H. Growth of TiO<sub>2</sub> Thin Films by Atomic Layer Deposition (ALD). *Adv. Mater. Res.* **2016**, *1133*, 352–356. <https://doi.org/10.4028/www.scientific.net/AMR.1133.352>.
- (246) Libardi, J.; Grigorov, K. G.; Massi, M.; da Silva Sobrinho, A. S.; Pessoa, R. S.; Sismanoglu, B. Diffusion of Silicon in Titanium Dioxide Thin Films with Different Degree of Crystallinity: Efficiency of TiO<sub>2</sub> and TiN Barrier Layers. *Vacuum* **2016**, *128*, 178–185. <https://doi.org/10.1016/j.vacuum.2016.03.031>.
- (247) Dobrzańska-Danikiewicz, A. D.; Dobrzański, L. A.; Szindler, M.; Dobrzański, L. B.; Achtełik-Franczak, A.; Hajduczek, E. Microporous Titanium-Based Materials Coated by Biocompatible Thin Films. In *Biomaterials in Regenerative Medicine*; Dobrzański, L. A., Ed.; InTech, 2018. <https://doi.org/10.5772/intechopen.70491>.
- (248) Krisdhasima, V.; McGuire, J.; Sproull, R. A One-Film-Model Ellipsometry Program for the Simultaneous Calculation of Protein Film Thickness and Refractive Index. *Surf. Interface Anal.* **1992**, *18* (6), 453–456. <https://doi.org/10.1002/sia.740180614>.

- (249) Aarik, J.; Aidla, A.; Kiisler, A.-A.; Uustare, T.; Sammelselg, V. Effect of Crystal Structure on Optical Properties of TiO<sub>2</sub> Films Grown by Atomic Layer Deposition. *Thin Solid Films* **1997**, *305* (1–2), 270–273. [https://doi.org/10.1016/S0040-6090\(97\)00135-1](https://doi.org/10.1016/S0040-6090(97)00135-1).
- (250) Vallant, T.; Brunner, H.; Mayer, U.; Hoffmann, H.; Leitner, T.; Resch, R.; Friedbacher, G. Formation of Self-Assembled Octadecylsiloxane Monolayers on Mica and Silicon Surfaces Studied by Atomic Force Microscopy and Infrared Spectroscopy. *J. Phys. Chem. B* **1998**, *102* (37), 7190–7197. <https://doi.org/10.1021/jp981282g>.
- (251) Kubicek, M.; Holzlechner, G.; Opitz, A. K.; Larisegger, S.; Hutter, H.; Fleig, J. A Novel ToF-SIMS Operation Mode for Sub 100nm Lateral Resolution: Application and Performance. *Appl. Surf. Sci.* **2014**, *289*, 407–416. <https://doi.org/10.1016/j.apsusc.2013.10.177>.
- (252) Sodhi, R. N. S. Time-of-Flight Secondary Ion Mass Spectrometry (TOF-SIMS):—Versatility in Chemical and Imaging Surface Analysis. *The Analyst* **2004**, *129* (6), 483–487. <https://doi.org/10.1039/B402607C>.
- (253) Bohrn, F.; Leitzenberger, M.; Schwab, S.; Kuegler, P.; Brunnbauer, L.; Jordan, S.; Hutter, H. Study on the Ion Migration of Silver Ions from Aqueous Solution in Epoxy-Based Molding Compounds by TOF-SIMS Measurements. *ECS J. Solid State Sci. Technol.* **2022**, *11* (2), 024006. <https://doi.org/10.1149/2162-8777/ac546b>.
- (254) Ohsaka, T.; Izumi, F.; Fujiki, Y. Raman Spectrum of Anatase, TiO<sub>2</sub>. *J. Raman Spectrosc.* **1978**, *7* (6), 321–324. <https://doi.org/10.1002/jrs.1250070606>.